1D modeling of blood flow in networks:
numerical computing and applications

THÈSE DE DOCTORAT

Présentée par

Xiaofei WANG

pour obtenir le grade de

DOCTEUR DE

L'UNIVERSITÉ PIERRE ET MARIE CURIE - Paris VI
Spécialité : Mécaniques
École Doctorale 391: Sciences mécaniques, acoustique, électronique & robotique de Paris

Soutenue publiquement le 17 Octobre 2014 devant le jury composé de:

Stéphane ZALESKI	Président
Pierre-Yves LAGRÉE	Directeur de thèse
Jose-Maria FULLANA	Codirecteur de thèse
Patrick SEGERS	Rapporteur
Franck NICOUD	Rapporteur
Sylvie LORTHOIS	Examinateur
Irène VIGNON-CLEMENTEL	Examinateur
Eleuterio F. TORO	Examinateur

Résumé

Notre étude vise à modéliser l'écoulement pulsé sanguin dans le réseau vasculaire humain. Celui ci est constitué d'un très grand nombre de vaisseaux disposés dans un vaste réseau ayant différentes propriétés mécaniques. Le modèle simplifié unidimensionnel (1D) permet une étude numérique dans le réseau sanguin et plusieurs applications seront proposées.

Le modèle 1D est établi grâce aux hypothèses de grande longueur d'onde de l'onde de pouls comparée aux rayons des vaisseaux et de profil de vitesse de révolution, en moyennant transversalement les équations de Navier-Stokes et de conservation de la masse. Un modèle viscoélastique de Kelvin-Voigt est adopté pour l'équation constitutive du tube. Cela conduit à un système hyperbolique-parabolique non linéaire, qui est ensuite résolu avec quatre schémas numériques, à savoir: MacCormack, Taylor-Galerkin, schéma monotone décentré pour les équations de conservation Law (MUSCL) et Galerkin discontinu local. Les schémas sont mis en oeuvre dans un premier temps dans MATLAB et les solutions numériques sont vérifiées favorablement à des solutions semi-analytiques et des observations cliniques. Des comparaisons entre les schémas sont faites pour quatre aspects importants: la précision, la capacité de capturer des phénomènes de type choc, la vitesse de calcul et la complexité de la mise en oeuvre, enfin les conditions appropriées pour l'application de chaque système sont discutées. Après cela, un code objet général en C++ est développé et testé sur plusieurs réseaux: un cercle d'artères, un réseau systémique humain de 55 artères et un rein de souris avec plus d'un millier les segments. La répartition en fonction du temps de la pression dans les réseaux est visualisée et les modes de propagation des ondes sont bien capturés. Une bonne accélération est atteinte par parallélisation du code.

Le code développé est ensuite appliqué dans trois études. En premier lieu, les coefficients de frottement du fluide et la viscosité de la paroi sont déterminés avec des dispositifs expérimentaux bien définis constitués de tuyaux élastiques *in vitro*. Ces deux facteurs amortissant les ondes de pouls, ils sont difficiles à évaluer séparément. Nous les estimons par ajustement du modèle viscoélastique 1D avec les ondes de pression mesurées expérimentalement. Les valeurs ajustées des paramètres viscoélastiques sont conformes aux valeurs estimées avec d'autres méthodes. Les deux effets visqueux sont du même ordre de grandeur. *In vivo*, des séries chronologiques de la pression du diamètre en différents points d'un réseau artériel de mouton, sont analysées et les paramètres de viscoélasticité sont estimés. Le réseau du mouton est ensuite simulé, on montre que la visco-élasticité amortit de manière significative les hautes fréquences. En troisième lieu, la variation de la circulation induite par des anastomoses axillo et fémoro-fémorales avec une sténose iliaque sévère! est simulée. L'influence de la voie de contournement est étudié.

Abstracts

The vascular network consists of a very large number of segments with various properties and thus the pulsatile blood flow inside is very complicated. With the time-domain-based nonlinear 1D model, this thesis studies the blood flow in networks, focusing on the numerical computing and several applications.

With assumptions of long wave and axisymmetric velocity profile, the 1D governing equations of mass and momentum are derived by integrating the continuity and Navier-Stokes equations along the radius. A Kelvin-Voigt viscoelastic model is adopted for the constitutive equation of the tube. This leads to a nonlinear hyperbolic-parabolic system, which is then solved with four numerical schemes, namely: MacCormack, Taylor-Galerkin, Monotonic Upwind Scheme for Conservation Law (MUSCL) and local discontinuous Galerkin. The schemes are implemented in MATLAB and the numerical solutions are checked favorably against analytical, semi-analytical solutions and clinical observations. Among the numerical schemes, comparisons are made in four important aspects: accuracy, ability to capture shock-like phenomena, computational speed and implementation complexity. The suitable conditions for the application of each scheme are discussed. After this, a general purpose C++ code is developed and tested on several networks: a circle of arteries, a human systemic network with 55 arteries and a mouse kidney with more than one thousand segments. The time dependent distribution of pressure in the networks is visualized and the propagation patterns of the waves are well captured. Good speedup is achieved by parallelizations of the code.

The developed code is applied in three studies. First, the coefficients of fluid friction and wall viscosity are determined with aides of a well defined experimental setup. Because both the two factors damp the pulse waves, they are difficult to evaluate separately. We estimate them in pairs by fitting the 1D viscoelastic model against pressure waves measured on the experimental setup. The fitted values of viscoelastic parameters are consistent with values estimated with other methods. The effect of wall viscosity on the pulse wave has been shown in the same order of that of fluid viscosity. Second, with time series of pressure and diameter measured in several locations of the sheep arterial network, the viscoelasticity parameters are estimated. With those values, the pulse waves in the sheep network are simulated and the effect of viscoelasticity is investigated. Numerical solutions show that the viscoelasticity damps significantly the high frequency components of the pulse waves. Third, we simulate the change of blood flow induced by the axillofemoral and femoral-femoral anastomoses with a severe iliac stenosis. The influence of the bypassing path is studied.

Acknowledgements

The working environment influences a scientist like the growing environment to a fruit tree. Without the help of many people, I cannot yield with three years of research the fruit—this manuscript of thesis.

First of all, I would like to thank my supervisor Pierre-Yves LAGRÉE. Besides being an active researcher in multiple directions of fluid mechanics, he is also an excellent advisor, who really cares the full development of PhD students. He believes that curiosity is a very important driving factor of scientific discoveries and thus respects my research interests. My co-supervisor, Jose-Maria FULLANA, also gives me advices in a lot of aspects, from doing research to making presentations. I benefit from both my supervisors not only in scientific knowledge, but also in the good working conditions they create for me. They cover generously my national and international travel expenses for conferences and collaborations. I feel very honored and lucky to do my PhD thesis under their supervision.

The collaborators of our team of course deserve my gratitudes because this thesis directly benefits from their works or ideas. I give a big thank you to Prof. Mami MASTUKAWA and Mr. Shohei NISHI (Doshisha Univerisity, Japan) for the collaborations on the experimental measurements; to Dr. Jean-Frédéric GERBEAU (Director of research, INRIA Paris-Rocquencourt, France) for his guiding me to this research topic; to Prof. Ricardo L. ARMENTANO (Favaloro University, Argentina) for his group's measurement data on sheep; to M.D. Salam ABOU TAAM (Hospital Foch, France) for his medical knowledge in anastomosis surgeries; to Dr. Sylvie LORTHOIS (Director of research, CNRS, Institut de Mécanique des Fluides de Toulouse, France) and Dr. Cecile DUPLAA (Director of research, INSERM, U1034 Adaptation cardiovasculaire à l'ischemie) for the geometrical data of a mouse kidney vascular; to Dr. Olivier DELESTRE (Université de Nice Sophia-Antipolis, France) for the discussions on the numerical methods; and to Dr. Hélène COULLON (University of Orléans, France) for her useful advices on code development.

It has been a great pleasure to work in the same office with Julien PHILIPPI, Gounséti PARÉ, Luca MARGHERI and Cansu OZHAN. During my PhD research, I have discussed a lot with colleagues in the Institute of d'Alembert and ICS (Institut du Calcul et de la Simulation, UPMC). I am very sorry that I cannot list their names here one by one because the list would be very long. I really enjoy the discussions with them and my research life is much more colorful because of them.

I want to acknowledge the scholarship of China Scholarship Council (2010-1013) and the French state funds managed by CALSIMLAB and the ANR within the investissements d'Avenir programme under reference ANR-11-IDEX-0004-02 (2013-2014).

I give special thanks to the two referees of my thesis: Prof. Patrick SEGERS (Ghent

University, Belgium) and Prof. Franck NICOUD (Université Montpellier 2, France). I also acknowledge the great gentleness of the other four examiners of the jury committee besides my two supervisors: Prof. Stéphane ZALESKI (Institut d'Alembert, UPMC, France), Dr. Irène VIGNON-CLEMENTEL (INRIA Paris-Rocquencourt, France), Dr. Sylvie LORTHOIS (CNRS, Institut de Mécanique des Fluides de Toulouse, France), and Prof. Eleuterio F. TORO (University of Trento, Italy).

Last but not least, my deepest gratitude shall go to my family. Without their support, I could not go as far as today in pursuing a dream in academia.

Contents

1. Introduction

1.1. Background

The most easily noticed feature of blood flow in arteries is perhaps the pulsation phenomenon. It has been studied and used in medical practices for thousands of years. For example, in traditional Chinese medicine, the practitioners palpate on six locations of the two wrists. Those positions are mapped to various organs as shown in Fig. 1.1. The pluses are classified by several characteristic elements, such as depth, rate, regularity, width, smoothness etc. The practitioners determine the health status of individual organs and of the whole body by examining those characteristics. Several traditional classic medical books (e.g. Nei Jing, 475–221 B.C.) have summarized the empirical knowledge accumulated by generations of practitioners. But we did not find anatomical evidence for the mapping between the palpating positions and the organs. Moreover those methods are described in qualitative manners, thus there are no precise standards for the practitioners to follow. Although the traditional medicine is controversial in many aspects, it is still an important part of the healthcare system in several asian countries. Scrutinizing those methods with modern techniques and medical knowledge is now an active research field [17, 82, 90]. If strong statistical correlations between diseases and some characteristics of pulses are established, palpating pulses is obviously a very advantageous prognosis method. In contrast with this empirical approach, which dose not investigate the wave propagation mechanism, the deterministic approach relies on deep understanding of the pulse wave behaviours in the cardiovascular system.

The modern concept of blood circulation was established by Harvey in 17^{th} century. Since then many talented mathematicians and physicists have been attracted to study the blood flow in the vascular system. In 1775, L. Euler derived the partial differential equations describing the conservation of mass and momentum for an inviscid fluid. But he could not solve the equations and thus did not recognize the wave characteristics of the system. T. Young gave the first scientific description of waves of blood flow in 1808. G. Hagen (in 1839) and Jean L. M. Poiseuille (in 1838) derived independently the resistance formula of the laminar flow in a long tube. In 1878, A. I. Moens and D. Korteweg established the formula of the speed of waves in a distensible vessel. B. Riemann introduced the method of characteristics and it was applied to the study of arterial blood flow since the decade of 1950. John R. Womersley's approach is to neglect the nonlinear convection term, and make analysis on frequency domain [72].

The aforementioned studies were done before the advent of powerful digital computers. In recent decades, the box of research tools has been enriched a lot due to the progress of computer science, image analysis and computational fluid dynamics (CFD). The majority of current simulations are done on computers by solving three-dimensional,

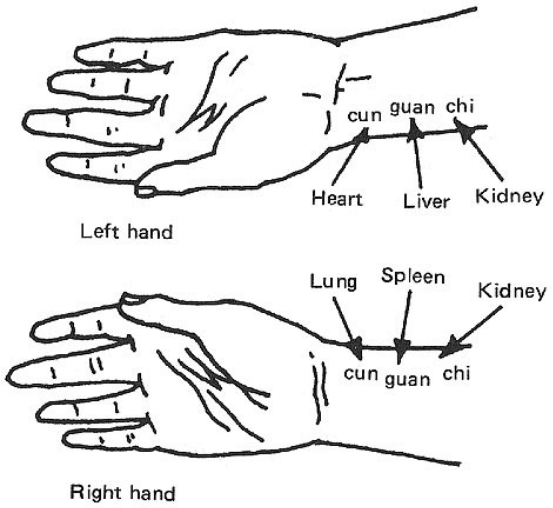

Figure 1.1.: Positions to palpate pulses in traditional Chinese medicine (from Ref. [21]).

nonlinear one-dimensional, zero-dimensional or multi-scale models.

At the same time, cardiovascular related diseases have become the leading killers globally, due to many unhealthy living styles and various environment pollutions. According to a report by World Health Organization, cardiovascular diseases are responsible to 48% of the total deaths in 2008 caused by noncommunicable diseases, while cancers come second with a ratio of 21% [1]. This necessitates a lot of researches on cardiovascular system in multidisciplinary fields, among which studying the hemodynamics of blood flow is a very important part. Well understanding of the pulsatile flow in vascular vessels can benefit in at least the following aspects:

1. To help investigate the pathology of diseases. Surely, cardiovascular diseases are related with many factors. But a lot of studies show that arterial wall remodels in response to the mechanical stimuli imposed by the blood. Quantities of the flow field, e.g. wall shear stress (WSS), turbulence etc. are directly related with the initiation and progression of atherosclerosis, stenosis and aneurysms [52]. Many previous CFD studies always assume a steady flow or/and rigid walls. In many scenarios, the unsteadiness and wall movement may have significant influence on the predictions of CFD simulation. It is necessary to model the pulsatile flow within distensible vessels to predict more reliably or to justify the aforementioned simplified assumptions on walls and inflow & outflow boundary conditions.

2. To develop non-invasive diagnosis tools. The most well known quantities of blood flow used as diagnosis purpose must be the heart rate and the systolic/diastolic pressure. Those biomarkers can be measured easily and are reliable for some diseases. Recently, more tools based on analysis of pulse waves have been proposed for early detections of vascular disorders, such as pulse wave velocity (PWV), cardioankle vascular index, pulse wave separation method et al. [66]. Development of

techniques to estimate parameters from flow rate and pressure makes the applications on this direction promising [40, 44].

3. To optimize the design of intravascular prostheses and surgery planning. We have seen some simulations of bypass graft surgery in both coronary [68] and peripheral [33, 34, 48, 95] vascular systems. The insertion of a stent changes the local compliance of the vessel. The pressure reflection and WSS alterations incurred by the stent can be predicted by computing of an unsteady blood flow field with moving boundaries [53].

1.2. Blood flow in vascular networks from a mechanical view

Briefly speaking, the circuit of blood circulation consists of one pump and two networks of vessels. The role of pump is played by the heart which contracts and relaxes periodically. One network starts from aorta and branches progressively into a lot of smaller and smaller vessels. Millions of vessels with the smallest diameter and thinnest wall in this network form the capillary bed, where exchange of materials (e.g. gas, nutrients, hormones) with the surrounding tissues happens. After the capillary bed, the smallest vessels converge to venules which merge again to form larger veins. The network of veins converges progressively to cenae cavae which connect to the right atrium of the heart. The pulmonary network is very similar in topology to the systemic network but has a smaller size and the pressure inside is lower, because it is only for material exchange with the lung.

In this study, we discuss the systemic network, the main arteries of which are illustrated in Fig 1.2. In the contraction phase of the heart, blood is pushed into the aorta from the left ventricle. The journey of blood in the systemic network starts here and goes through a series of vessels with various properties. We discuss them in the following:

- *Large-sized arteries.* Those arteries are also called elastic arteries because the wall has a large number of collagen and elastin filaments. When the heart ejects blood, the elastic arteries dilate to accommodate the blood. This mechanism avoids a too high diastolic pressure at the root of the aorta, and thus reduces the afterload of the heart. When the heart relaxes and the aortic valve closes, the arteries recoil to keep the diastolic pressure at a high level and the blood is still pushed forward. By this buffering effect, the violent pulsations generated by the left ventricle are significantly smoothed. The deteriorating of the buffering effect due to the stiffening of arterial wall is the main cause for hypertension. The pulse wave velocity, which increases in hardened vessels, has been recognized as early indicators of the health status of the cardiovascular system. Another feature of blood flow in large arteries worthy to note is that the pulse wave's front is steepened due to the convection effect as it propagates down the system.

- *Medium-sized arteries.* Those arteries form the main frames of the networks supplying blood to some specific organs and there are layers of smooth muscle cells in the wall. Thus they are also called distributing arteries or muscular arteries.

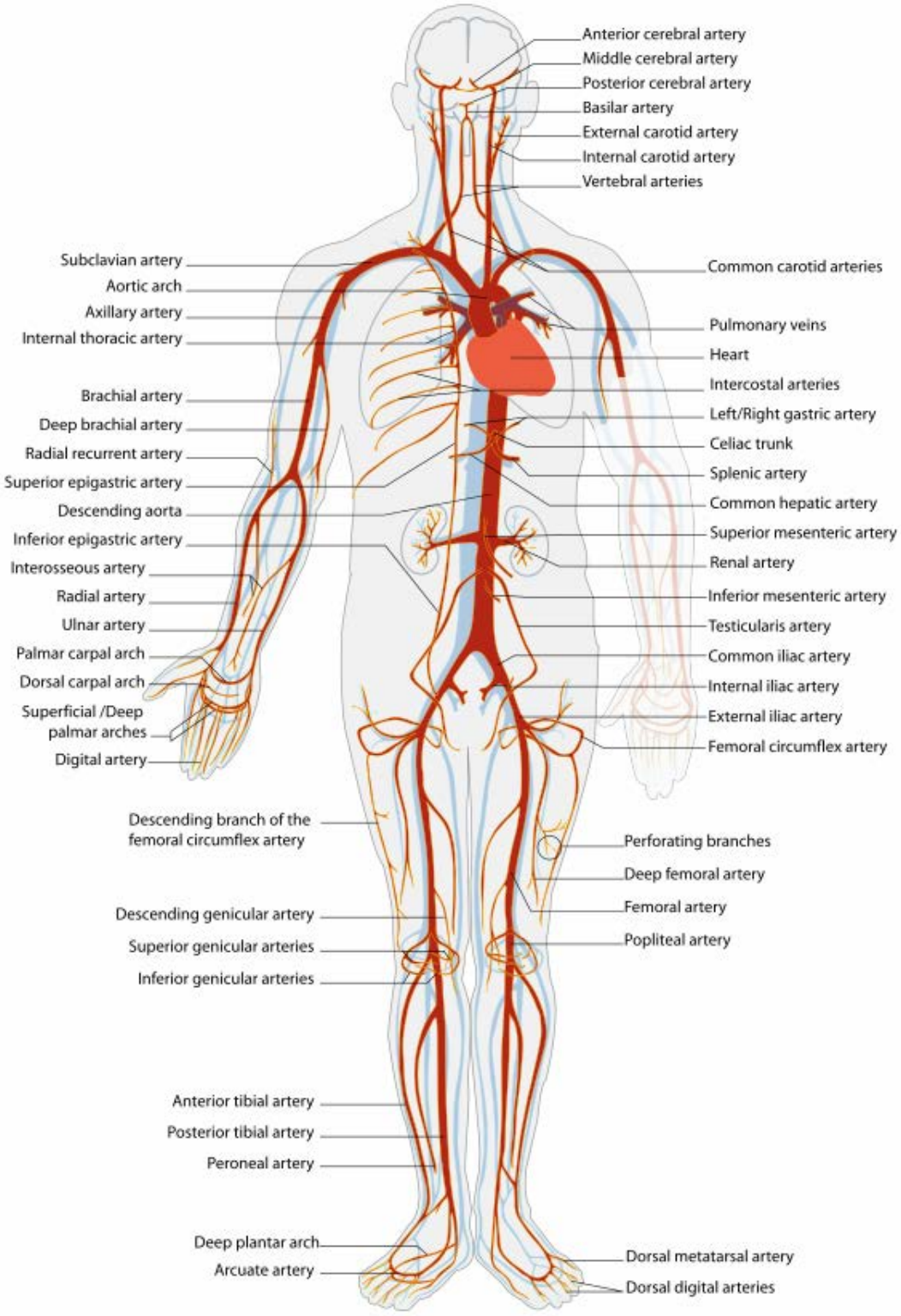

Figure 1.2.: Arterial system. From Gray's anatomy 36$^{\text{th}}$ edition by Williams & Warwick.

The stiffness and viscosity of the wall are bigger than those of large arteries. Partially due to the weakened buffering effect (reflection at peripheral sites may be another reason), the pulse pressure (difference between systolic and diastolic pressure) increases, while the mean pressure drops slightly (see Fig. 1.3). As shown in Table 1.1, due to many branches in this level, the total cross section increases. The mean flow in those arteries is smaller than in the large arteries, thus the nonlinear convection effect becomes smaller as well. Because of this, the profile of the waveform becomes less front-steepened than in the large arteries.

- *Arteriole.* This kind of arteries are characterized by layers of muscle cells which are regulated by autonomic nervous system and hormones. According to Poiseuille's theory, the resistance of the a tube to the flow is CL/R^4, where L is the length of the tube, R is the radius and C is a constant coefficient. From Table 1.1, we see that the characteristic diameters of large arteries and arterioles are 2cm and 0.05cm respectively. Even though we assume the arterioles are 1/10 in length and 10 times in total cross-sectional area of the large arteries, the resistance of the former is 25600 times of the latter. The main resistance of the network mainly resides in this level of vessels and the capillary bed. As shown in Fig. 1.3, the pressure starts to drop sharply at this level. The muscle cells can contract or relax to change the resistance significantly. The blood supply is thus regulated according to the metabolic needs of the organs.

- *Capillaries.* The wall of capillaries is formed by only one layer of endothelial linings. To maximize the total area of the capillary bed, the diameter of capillaries is so small that the red blood cells have to deform to pass through them. This structure facilitates material exchange. Due to the buffering effect of the arterial network, the pressure pulsation becomes very weak here, and the blood moves steadily.

- *Venules.* Vessels at this level collect blood from the capillary bed and forward them further to larger veins.

- *Veins.* The pressure at this level drops to almost zero (in lying down position). Compared with arteries, veins have some different features. First, there are valves in some veins to keep the flow uni-directional. Even though there is no big resistance in the venous network for the blood to go back to the heart, there lacks pressure gradient to balance the gravity in the lower limbs. Muscular contractions around deep veins help to propel the blood upward. Second, the wall may collapse because there are cases when the internal pressure is smaller than external pressure. Third, the wall of veins is thin and the Young's modulus is much smaller. The veins are easy to dilate to accommodate blood. According to the wave theory, the wave speed is also smaller than that in arteries. In same cases, the skeleton muscle contraction causes very large acceleration of the blood flow, such that shock-like phenomenon may form in the veins. We will discuss the possibilities in this thesis (Chapter 3).

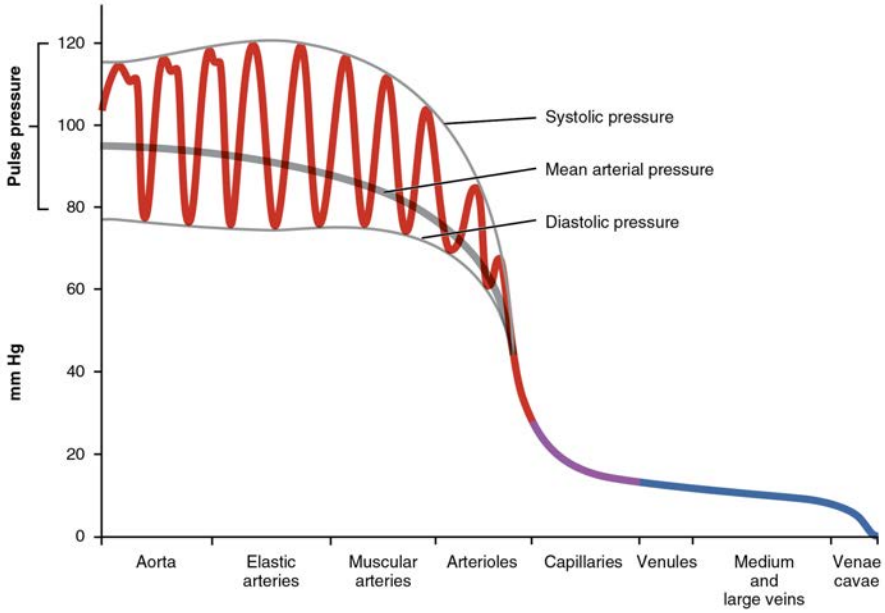

Figure 1.3.: Systemic blood pressure. From Anatomy & Physiology, OpenStax College.

If we truncate at the level of very small arteries where the pulsation is not significant, the arterial system can be considered as a very large network of distensible tubes whose impedance mainly resides in the outlets of the network. As shown in Table 1.1, for a 20kg-dog, the number of vessels in this truncated network can be the order of magnitude of 10^5. The main features of blood flow in this network can be summarized as: pulsation in time, wave transmission in space and large number of vessel segments.

1.3. Models for blood flow in distensible tubes

Models with various complexities have been developed for the pulsatile flow. They can be briefly summarized as follows:

1. *Three-dimensional models.* In those models, the mass conservation equations, time dependent Navier-Stokes equations and equations of elasticity of vessel wall are solved with proper boundary conditions [30]. Based on medical imaging, a patient-specific simulation of the largest arteries of a whole body has been proven possible very recently [97]. While this simulation provides many details of the flow field, it is very expensive to compute. Moreover, there are a lot of parameters to set in this model, which makes it difficult for clinical applications. At the current stage, such simulations are only suitable for the purpose of research when supercomputers are available. The most feasible approach is to model only one or several segments of interest with the 3D model, while the rest of the network is described by proper boundary conditions. 0D models can be integrated with 3D models to provide

System level	Section	Mean Diameter(cm)	Number of vessels	Total cross section
1	Aorta	(19-4.5)	1	(2.8-0.2)
2	Arteries	4.000	40	5.0
3	Arteries	1.300	500	6.6
4	Arteries	0.450	6×10^3	9.5
5	Arteries	0.150	1.1×10^5	19.4
6	Arterioles	0.050	2.8×10^6	55.0
7	Capillaries	0.008	2.7×10^9	1357.0
8	Venules	0.100	1.0×10^7	785.4
9	Veins	0.280	6.6×10^5	406.4
10	Veins	0.700	4×10^3	154.0
11	Veins	1.800	2100	53.4
12	Veins	4.500	110	17.5
13	Venae Cavae	(5-14)	2	(0.2-1.5)

Table 1.1.: Vascular dimensions in a 20-kg dog (reproduced from Milnor 1989)

quite realistic boundary conditions with a limited computational cost [8, 88].

2. *Two-dimensional models.* For a tube flow, if turbulence is not considered, the velocity at the circumferential direction can be neglected, and only velocities in the axial and radial directions are computed. Usually, the nonlinear convective term is neglected and solutions are found in frequency domain.

3. *One-dimensional models.* In addition to the assumption of axial symmetry, the long-wave assumption is always satisfied for the blood flow waves. With those two main assumptions, the pressure at the local cross sections is considered constant and thus radial velocity is neglected. In this model, the velocity is described by $v_x(t, r, x)$, where t is time, r is radius and x is axial distance. This model is sometimes called 1.5 dimensional model [14, 38, 43]. If a proper axial velocity profile $\Phi(r)$ is prescribed such that $v_x(t, r, x) = \bar{v}_x(t, x)\Phi(r)$, we can integrate the governing equations over r. Thus the conservation of mass and balance of momentum can be expressed as partial differential equations in time and axial distance. This system is closed by a constitutive law of the mechanical properties of the wall. While those models can not simulate details of the blood flow, e.g. vortex, flow separation, both *in-vitro* [2, 67, 92] and *in-vivo* [20, 56, 63, 64, 78, 95] observations have shown that they can capture all of the features of the waveforms. Compared with 3D simulations, the reduction of computation cost is at least 1000 [96]. According to a recent report [2], a simulation of a network with about 100 segments for one cardiac cycle can be done in the order of magnitude of minute.

   The 1D models are well balanced between complexity and computation cost, thus they are very suitable for many applications. In clinical applications, real time computations are usually required. In parameter setting or data assimilation frame-

works, the problem needs to be computed millions of times [39]. With the 1D model, it is possible in the near future to have fast, accurate, patient-specific and clinically applicable solutions for the simulation of full bodies.

4. *Zero-dimensional models.* Zero dimensional models are described by ordinary differential equations dependent only on time. Because those models do not depend on spatial variable (thus the name 0D or lumped models), the wave propagation in space can not be captured. Those models are very cheap and they can describe the impedance of a vascular network (thus also named as Windkessel models). They are usually integrated with 3D [88] or 1D [87] models to provide the inflow and outflow boundary conditions. The 0D models can also be used to make concise investigations of the dynamics of the whole cardiovascular system [73].

1.4. Problems for one-dimensional models

There are some factors that may influence the validity of the 1D models. We study them in order of magnitude or discuss with experimental observations in the following.

- *Blood rheology.* The blood is considered as *Homogenous*, *Newtonian* and *Incompressible* fluid. About 45% of blood in volume are taken by blood cells, of which the majority are red blood cells (hemocyte). The disc-like red blood cells have a diameter $D_r \approx 0.007$ mm. There are some white blood cells with a bit larger size. But the number of white blood cells is very small compared to the red blood cells. In [76], vessels with diameters $D_v \geq 0.1$ mm were simulated by the 1D model. If we assume the minimum vessel for the 1D model is 0.1 mm in diameter, then the ratio between the two diameters D_v/D_r is larger than 14.3. In fact, the blood is a well known non-Newtonian fluid with a shear-thinning property. But only in vessels with an internal diameter of less than 1mm, the apparent viscosity is dependent significantly on the shear rate [52]. However, in vessels smaller than this value, we can tune the friction coefficient to account the changed viscosity. Within each particular vessel segment, we consider the viscosity is constant, i.e. the blood is a Newtonian fluid. The bulk Young's modulus of water is about 2.2×10^9 Pa and that of a vessel volume to internal pressure is about 2.2×10^4. The ratio between the two moduli is 10^5, thus the incompressibility of blood is obvious.

- *Lateral leakage and tapering.* The aorta is tapering from the proximal to the distal end. The tapering wall will increase the pulse pressure by continuous reflection. It is also observed that there are tiny side branches at the aorta. Some studies show that the effect of tapering wall is compensated by the blood loss to the side branches. In net effect, it is more like a flow in a straight tube with no lateral leakage [52]. However, both the branches and tapering can be modeled by the 1D models. The net effect needs further research. In our model, we just assume that there is no distributive blood loss, because the arterial wall is considered as impermeable.

- *Wave length is much longer than vessel radius.* In the aorta, the wave speed is about 5 m/s and the radius is about 10 mm [52]. If we assume the period of one pulse is 1 second, the ratio between the wave length and the radius is 500. In smaller arteries, the wave speed increases and the radius decreases, the ratio becomes even bigger. Thus the long wave assumption is fully justified.

- *Profile of axial velocity.* One crucial step in deriving the 1D model is to prescribe a proper axial velocity profile. The fluid friction coefficient and the correction factor of the convection term in the momentum balance equation are dependent on this profile. The ratio between the transient inertia force and the viscous force can be estimated by the Womersley number $R\sqrt{\omega/\nu}$, where R is the internal radius, ω the angular frequency and ν the kinematic viscosity of blood. Table 1.3 shows the Womersley number at various arteries calculated using a cardiac frequency of 2 Hz, a kinematic viscosity of blood 3.3×10^{-6} m^2/s. From the table, we see that the inertia force are bigger than viscous force in larger vessels. In this case, the profile is essentially flat in the central part and there is a thin viscous boundary layer to match the no-slip boundary condition near the wall. When the Womersley number is very small in the small vessels, the profile is more close to a parabolic or Poiseuille flow. We will discuss this in more details in chapter 2 and 5. We usually assume that the profile is the same within one segment, while it may vary through the network.

- *Turbulence.* Since the mean Reynolds number (computed from the mean flux between systolic and diastolic ones) in aorta is over 4000 (see Table 1.3 and [79]), the flow should be described as turbulent if it is in a straight pipe with the given steady flux. In unsteady case, we consider, the flow is at least transitional to turbulence if it is not turbulent. In small arteries, the Reynolds number drops a lot because both the velocity and the diameter of the vessels become smaller. Given that the Womersley number is also much smaller in small arteries, laminar flow is very likely to appear in small arteries. That gives justification to Poiseuille's theory in estimating the peripheral resistance. In medium-sized arteries, there may be complex transition conditions between turbulent and laminar flow. The 1D models neglect the velocity components in the circumferential direction and thus a laminar flow is an implicit assumption. However, the dissipating effect of turbulence on energy can be lumped into the skin friction term.

- *Constitutive equation of vessel wall.* The constitutive equation of the wall is derived from thin shell theory. The characteristic thickness of wall is 0.2 mm and the radius of vessel is 2 mm. Then the ratio between the two is 0.1. The wall shows nonlinear elasticity properties in high pressure and the inertia of the wall may affect the pulse wave as well. But in most cases, a linear one is enough for a first approximation. Some recent studies show that viscoelastic property has a considerable effect on the pulse waves. We will investigate further on the viscoelasticity in this study.

- *Gravity of blood.* Given that the density of mercury is 13.56 times of that of water,

Diameter	Total resistance	Total cross area	Fluid speed	Wave speed	Womersley number
↓	↑	↑	↓	↑	↓

Table 1.2.: Changes of characteristics of the arterial tree from aorta to arterioles

the hydrostatic pressure at the foot is about 125 mmHg (1 mmHg $\approx$ 133 Pa) for a normal adult man with a hight of 170 cm in standing posture. This is indeed a big number compared with the pressure in arteries (80-120 mmHg). In clinical applications, the blood pressure is measured when the subject is in supine or siting posture. In those cases, the pressure difference through the whole body caused by gravity is much smaller than the pressure at the arterial system. In this study, we will not consider the gravity. But we note that it can be added as a source term if necessary.

- *Curvature and bifurcation.* Both the curvature and bifurcation will dissipate energy of the blood flow. Experimental study shows that the energy loss at bifurcations is very small [50]. Our experiments on medium-sized tubes show that the energy dissipation caused by curvature is also negligible.

- *Boundary conditions.* Because the network of vessels is very large, we usually have to truncate it at some levels. The truncated subnetworks have to be described properly. Reflection coefficient, structured tree [56], 0D models [23] and some other kind of generalized methods for specific numerical schemes [87] have been investigated as the boundary conditions of the 1D models.

- *Extension to veins.* With some modifications, the 1D models can also be used in simulation of venous flow. There are three special features of venous system that need to be treated: inflow from venules bed, muscular contraction and valves. The inflow can be considered as a source term in the mass conservation equation; the muscular contraction can be described by an external pressure in the constitutive equation of the vessel wall; the valves, which in fact allow very small reverse flows, can be modeled by very large resistances when the pressure gradient is unfavorable to the blood flow to the heart [27].

The 1D model may be used to simulate the blood flow in the arterial tree truncated at the level of arteries as small as 0.1mm in diameter. From aorta to small branches of the tree, the changes of characteristics are summarized in Table 1.2.

1.5. Research context of the thesis

We briefly survey the recent literature and state the motivations of the thesis in the following two aspects.

Section	Radius (cm)	Womersley	Reynolds
Ascending Aorta	0.75	14.628	4543
Descending Aorta	0.65	12.677	-
Abdominal Aorta	0.45	8.777	-
Femoral Artery	0.2	3.901	605
Carotid Artery	0.25	4.876	1060
Arteriole	0.0025	0.049	-
Capillary	0.0003	0.006	-
Venule	0.002	0.039	-
Inferior Vena Cava	0.5	9.752	-
Main Pulmonary artery	0.85	16.578	-

Table 1.3.: Womersley and Reynolds number in the cardiovascular network

1. *Modeling and numerical solver.* To close the system of governing equations, an axial velocity profile and a tube law have to be prescribed. As discussed before (Section 1.4), the profile is dependent on time and location. Various models have been provided, of which the flat and Poiseuille (parabolic) profiles are the two simplest ones. Another class of models are described by power law [35] and more recently, models with viscous boundary layers have been proposed [5, 10, 38, 56].

   It has been known that the arterial wall show nonlinear viscoelastic behaviours. But usually linear elastic models are integrated into the 1D fluid models for simplicity. Recent studies indicate that the viscoelasticity may have significant influence on the the pulse waves [2, 9, 32, 60, 61, 62, 77].

   Keeping this in mind, we studied the fluid viscosity and wall viscoelasticity in a well defined experimental setup. The viscoelasticity parameters were measured accurately and compared with the value fitted from a 1D model (Chapter 5). Moreover, *in vivo* viscoelastic data measured on a group of sheep have been taken advantage of and the influence of viscoelasticity on pulse waves have been investigated (Chapter 6).

   On possible approach to solve the 1D models is to linearize the system by neglecting the convection term and then find solutions in frequency domain [53, 91]. Recently, a lot of numerical schemes have been designed to solve the nonlinear equations in time domain. Various finite difference [22, 56, 64, 67, 76, 80, 102], finite volume [15, 19, 94], finite element [2, 25, 46, 71, 87] and discontinuous Galerkin schemes [2, 48, 50, 51, 71] have been applied on this problem. We are motived to test and make a cross-comparison between them so that suitable application conditions of each scheme can be suggested (Chapter 3).

2. *Applications*

   The predictions of 1D models agree quantitively with experimental observations when accurate parameters of the models are available [2, 50, 67]. However, the numerical results only meet qualitatively with *in vivo* data [20, 56, 63, 64, 78, 81].

Beside the poor accuracy of non-invasive measurement techniques on the *in vivo* data, lack of patient-specific information on model parameters is another reason. To know the sensitivity of the output to the uncertainties of each parameter of the 1D models, some sensitive analysis have been done [16, 39, 98]. To estimate the parameters, we can compare the model output with measurements and minimize the difference by tuning the parameters [40, 44]. Many conjectured applications of the 1D models rely on the solution of the reverse problems. But researches on this direction are only on early stage. In these studies, the computations have to be run millions of times, which contribute to our motivations to develop a fast numerical code (Chapter 4).

In one class of applications of 1D models, we simulate the diseased blood flow and various surgery plans hoping that optimized guidance to surgeons may be given accordingly. Even though there are a lot of difficulties on setting the parameters of patient-specific models and usually only qualitatively accurate predictions can be given, we still can extract a lot of clinically relevant information. For example, Huberts et al. show that the mean pressures and flows after an arteriovenous fistula surgery can be simulated with 1D models with quite satisfactory accuracy [34]. Another successful example is the simulation of blood flow after femoro-popliteal bypass surgery [95]. Inspired by this, we simulated a whole systemic arterial network with a femoral stenosis and the blood flow after axillo-femoral, femorofemoral bypass surgeries. The applications of 1D models in this scenario are discussed (Chapter 7).

1.6. Outline of the thesis

This thesis consists of two parts, one part on development of a parallel code (Chapter 2-4) and another part on applications (Chapters 5-7). The content of the thesis is outlined as follows.

Chapter 1 is this introduction.

Chapter 2 talks about the derivation of a nonlinear viscoelastic 1D model. In this chapter, the viscoelasticity of the vessel wall was described by a Kelvin-Voigt model. This model was integrated into to the equation of momentum balance, and thus a hyperbolic-parabolic problem was obtained. The characteristic structures of the hyperbolic part was discussed. The boundary conditions, both at internal conjunction nodes and ends of a vessel network, have been treated with the method of characteristic.

Chapter 3 presents four numerical methods to solve the governing equations. Since most previous numerical schemes are deigned for pure hyperbolic problems, we extend them to treat the hyperbolic-parabolic problem. In one approach, we applied an operator splitting method to separate the problem into hyperbolic and parabolic parts. The hyperbolic part was solved by three schemes: MacCormack, MUSCL (Monotonic Upwind Scheme for Conservation Laws) and Taylor-Galerkin. The parabolic part was solved by Crank-Nicolson method. In another approach, we elaborated a local discontinuous Galerkin method to solve the problem without splitting. We highlighted that the

diffusive term cannot be treated by a simple central numerical flux and a local auxiliary variable was introduced to stabilize the discontinuous Galerkin scheme (thus the name local discontinuous Galerkin). We implemented the four numerical methods in Matlab, verified them and compared them in performance. The proper application conditions for each scheme were discussed accordingly.

Chapter 4 treats the development of a parallel code. Noting that a fast code is needed in many cases, we developed a parallel C++ code with two of the four schemes. This code was verified and the speedup was tested on multicore computers by computing networks with various number of arteries. Tested on a normal workstation with 12 cores, the classic systemic network with 55 arteries can be computed in a few seconds for one cardiac cycle. Compared with a sequential one, the speedup is at least 8. We also highlighted that an anatomically accurate network of mouse kidney with about 1500 segments (built by Dr. Sylvie LORTHOIS and Dr. Cecile DUPLAA) can be computed in a few minutes. This code enables us to do sensitivity analysis and to fit parameters in a reverse way of large networks. In both those cases, the code speed is crucial because the computations have to be run millions of times. Another highlight of the code is that the configuration of simulations can be set conveniently through several comma separated value (CSV) files. The topology of the network is set by a directed acyclic graph (DAG), which can describe a quite general class of networks with various branching and convergence types. To record the evolution of interested quantities, the location and time interval can also be set flexibly. All other configuration options such as viscoelasticity and meshes are also set by CSV files. The output files can be read by Python and Gnuplot for post-processing. The C++ code does not depend on any third party libraries, and all steps of the simulation and data analysis can be done with free open source tools.

Chapter 5 studies the effect of fluid and wall viscosity on the pulse wave with aids of an experimental setup built in Doshisha University (Mami MASTUKAWA group, Kyoto, Japan). In the experimental setup, a distensible polymer tube was connected with a piston pump. We simultaneously recorded the wall displacement with a laser surface velocimeter (LSV) and the internal pressure with a pressure sensor. The viscoelasticity of the tube was calculated from the two time series. This value was compared with the value fitted from the viscoelastic 1D model. The measurement of viscoelasticity is more accurate than tensile test because the precision of both the LSV and the pressure sensor is very high. Previous studies fit the viscoelasticity with an inviscid fluid model, or just used measurements with tensile test without fitting; thus there is a doubt on the values of the fluid viscosity and wall viscoelasticity, because both of them are damping factors of the pulse wave. This research helps clear this doubt.

Chapter 6 shows a study of the effect of viscoelasticity on the pulse waves in the systemic arterial tree of sheep. The research group led by R. L. ARMENTANO (Favaloro University, Argentina) recorded the diameter and internal pressure at several locations of the *in vivo* arterial tree of a group of sheep. We took advantage of the data and estimated the viscoelasticity values. With those values, we built a sheep network and computed the pulse waves with and without viscoelasticity. The damping effect of high frequency components in the waveforms was illustrated.

Chapter 7 simulates the blood flow before and after operations of axillofemeral and femeral-femeral anastomosis. The influence of stenosis on femoral artery and the choice of grafts with different elasticity were discussed. This work was done in collaboration with vascular surgeon S. ABOU TAAM (Hospital Foch, Paris, France).

Chapter 8 summarizes the thesis and makes some perspectives.

Part I.

Mathematical Model and Code Development

2. Mathematical models

2.1. Introduction

The previous chapter gives the assumptions of the 1D model and the justifications for vascular blood flow, especially in large and medium-sized arteries. This chapter first talks about the derivation of a 1D viscoelastic model, highlighting the approximations made on the axial velocity profile and the vessel mechanical law. After this, the hyperbolic-parabolic structure of the 1D model is discussed. The boundary conditions at the inflow, outflow and internal conjunction points are treated with the characteristic method.

2.2. 1D mathematical model

2.2.1. Integration along radius

There are two approaches to derive the 1D model: one starts from Reynolds transport equation [26, 86, 94] and another from the Navier-Stokes equations [7, 35, 66, 94]. We take the second approach and make clear some mathematical tricks in the derivation. Let us consider a distensible vessel segment in a cylindrical coordinate system (r, θ, x) as shown in Fig. 2.1. The internal radius of the vessel is a function of x and time t, $R(x, t)$. Blood inside the vessel is considered as a homogeneous, Newtonian and incompressible fluid. The density of blood is denoted by ρ and the kinematic viscosity is denoted by ν. It flows in the vessel with velocity (v_r, v_θ, v_x) and pressure P. We consider that the gravity is negligible in this thesis. With an assumption of axisymmetry, v_θ vanishes

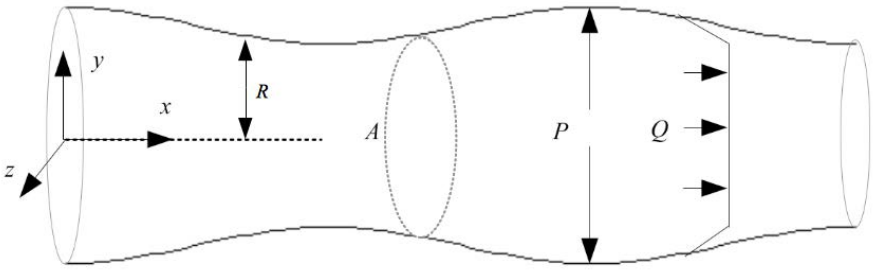

Figure 2.1.: Illustration of a distensible vessel segment. The flow rate is Q, the internal pressure P, the internal radius R and thus the cross sectional area $A = \pi R^2$. The two perpendicular surfaces at the ends of the vessel do not move horizontally.

and all other dependent variables do not depend on θ. Further invoking the long wave assumption, we can reduce the mass conservation equation and Navier-Stokes equations to the following form,

$$\frac{1}{r}\frac{\partial(rv_r)}{\partial r} + \frac{\partial v_x}{\partial x} = 0, \tag{2.1a}$$

$$\frac{\partial v_x}{\partial t} + v_r\frac{\partial v_x}{\partial r} + v_x\frac{\partial v_x}{\partial x} + \frac{1}{\rho}\frac{\partial P}{\partial x} = \frac{\nu}{r}\frac{\partial}{\partial r}\left(r\frac{\partial v_x}{\partial r}\right), \tag{2.1b}$$

$$\frac{1}{\rho}\frac{\partial P}{\partial r} = 0. \tag{2.1c}$$

Those governing equations are accompanied by the no-slip boundary condition

$$v_x(R) = 0,$$

and an assumption that the wall moves only along r

$$v_r(R, x, t) = \frac{\partial R}{\partial t}.$$

The third equation indicates that the pressure is constant along the radius.

First, we deduce the integral form of mass conservation equation. Multiplying Eq. (2.1a) with $2\pi r$ and integrating it along r, one gets

$$2\pi\left[\int_0^R \frac{\partial(rv_r)}{\partial r}dr + \int_0^R \frac{\partial v_x}{\partial x}rdr\right] = 0. \tag{2.2}$$

Before going forward, we recall the Reynolds transport theorem for a function $F(r, x)$ in the one dimensional domain $0 \le x \le R(x, t)$,

$$\frac{d}{dx}\left[\int_0^R F(r,x)dr\right] = \int_0^R \left[\frac{\partial F(r,x)}{\partial x}\right]dr + \frac{\partial R}{\partial x}F(r,x)|_{r=R}.$$

Applying this theorem to $v_x r$, we get

$$\frac{d}{dx}\int_0^R v_x r dr = \int_0^R \frac{\partial v_x}{\partial x}rdr + \frac{\partial R}{\partial x}\left[v_x r\right]_{r=R}.$$

If one invokes no-slip condition, $v_x(R) = 0$, the last term vanishes. By comparing this equation with Eq. (2.2), one gets

$$2\pi\int_0^R \frac{\partial(rv_r)}{\partial r}dr + 2\pi\frac{d}{dx}\int_0^R v_x r dr = 0,$$

or

$$2\pi R v_r(R) + \frac{d}{dx}\int_0^R 2\pi v_x r dr = 0.$$

We assume there is no gap between the fluid and the wall, thus $v_r(R) = \partial R/\partial t$. Also noting that the flow rate Q and cross area A are

$$Q = \int_0^R 2\pi v_x r dr, \quad A = \pi R^2,$$

we can write the mass conservation equation in terms of A and Q

$$\frac{\partial A}{\partial t} + \frac{\partial Q}{\partial x} = 0. \tag{2.3}$$

The integrations are straightforward for most terms in the momentum equation (2.1b). We only discuss the treatment of the convection terms: the second and third terms on the left hand side of Eq. (2.1b). We apply integration by part on the second term to get,

$$2\pi \int_0^R r v_r \frac{\partial v_x}{\partial r} dr = 2\pi \int_0^R \frac{\partial (r v_r v_x)}{\partial r} dr - 2\pi \int_0^R v_x \frac{\partial (r v_r)}{\partial r} dr.$$

The first term on the right hand side disappears because $v_x(R) = 0$. By invoking Eq. (2.1a), we can rewrite this equation as

$$2\pi \int_0^R r v_r \frac{\partial v_x}{\partial r} dr = 2\pi \int_0^R v_x \frac{\partial (r v_x)}{\partial x} dr.$$

With this equation, we can easily get the momentum equation in the form integrated over r

$$\frac{\partial Q}{\partial t} + \frac{\partial}{\partial x}\left(2\pi \int_0^R r v_x^2 dr\right) + \frac{A}{\rho}\frac{\partial P}{\partial x} = 2\pi\nu \left[r \frac{\partial v_x}{\partial r}\right]_{r=R}.$$

By letting

$$2\pi \int_0^R r v_x^2 = \alpha \frac{Q^2}{A},$$

where α is defined as:

$$\alpha = \frac{2\pi A}{Q^2} \int_0^R r v_x^2 dr = \frac{2\pi \int_0^R 2\pi r dr}{\left(\int_0^R r v_x dr\right)^2} \int_0^R r v_x^2 dr$$

we obtain

$$\frac{\partial Q}{\partial t} + \frac{\partial}{\partial x}\left(\alpha \frac{Q^2}{A}\right) + \frac{A}{\rho}\frac{\partial P}{\partial x} = 2\pi\nu \left[r \frac{\partial v_x}{\partial r}\right]_{r=R}. \tag{2.4}$$

2.2.2. Profile of axial velocity

To solve the system, we have to determine α and $\frac{\partial v_x}{\partial r}|_{r=R}$, which obviously depend on the profile of the axial velocity. In general, we assume that the velocity profile in one segment has the same shape $\Phi(r)$, or $v_x(r, x, t) = U(x, t)\Phi(r)$ with $U(x, t)$ as the average fluid velocity. The friction term can be rewritten as $-C_f U$ or $-C_f Q/A$, where C_f is dependent on $\Phi(r)$.

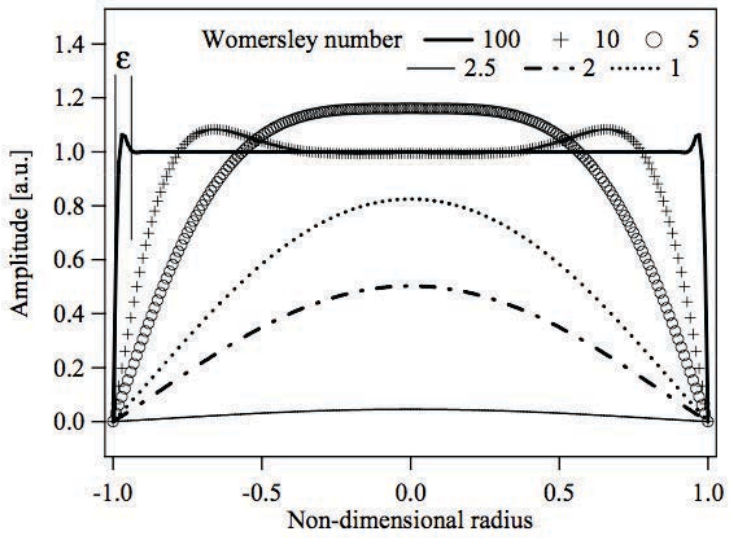

Figure 2.2.: Velocity profile in a stiff tube with various Womersley numbers. Reproduced from [65].

The Womersley number, defined as $\chi = R\sqrt{\omega/\nu}$ (it is usually denoted as α, but we have used α for the momentum correction coefficient), gives a strong indication on the profile. By applying Womersley's analysis method on a rigid tube, we can derive the two coefficients in two asymptotic cases [66],

$$\begin{cases} \alpha = 4/3 \quad C_f = 8\pi\nu, & \chi << 1 \\ \alpha = 1 \quad C_f = \sqrt{2}\pi\nu\chi, & \chi >> 1. \end{cases}$$

However, under physiological conditions the Womersley number is about 10 in large arteries and about 0.1 in small arteries. The values of the two coefficients should fall between the two cases listed above (see Fig. 2.2).

Hughes and Lubliner [35] introduced a power law velocity profile,

$$v_x = \frac{\gamma+2}{\gamma} U \left[1 - (\frac{r}{R})^\gamma\right]. \tag{2.5}$$

Through this formula, α and C_f are related in the equation

$$C_f = \frac{2\pi\nu\alpha}{\alpha - 1}.$$

By varying the parameter γ, we can approximate the velocity profile under various Womersley numbers. Fig. 2.3 plots the profile when γ is in the range from 2 to 9. We note that when $\gamma = 2$, the profile is a parabolic or Poiseuille one. As γ increases, the profile becomes closer to a flat one. When $\gamma = 9$, one gets $\alpha = 1.1$ and $C_f = 22\pi\nu$. The latter value was fitted from cardiovascular blood flow [76] and then was adopted by some following researches (e.g. [2, 48]).

In large arteries, predicted by Womersley theory, the central part of the profile is essentially flat and there is a viscous boundary layer to match the no-slip boundary condition. Olufsen et al. [56] assumed such an essentially flat profile and estimated the viscous layer by $\sqrt{\nu/\omega}$, where ν is the kinematic viscosity and ω is the angular frequency of the pulsatile flow. Noting that a phase difference between Q and wall shear stress is predicted by Womersley theory, Bessems et al. [10] added a correction term based on local Womersley number and $\partial P/\partial x$ to the friction term. There are some other models also based on the local Womersley number to approximate α and the friction term, such as [38, 101]. However, we do not elaborate them here.

Keeping in mind that α should vary in the range between 1.0 and 1.3 in the whole system, we take a uniform value everywhere the 1D model applies. The justification for this approximation is twofold. First, in large arteries, the thin boundary layer contributes very little to the integration of the convection term, thus α must be very close to 1.0. Second, in smaller arteries (where α is closer to 4/3), the whole convection term becomes relatively less important because the flow rate decreases and pressure drops more sharply (the convection term is even neglected to linearize the system in some studies). Thus we can set α to 1.0 or a slightly bigger value (1.1 for example), and this approximation sacrifices very little of modeling accuracy. For the friction term, however, we consider C_f depends on the local Womersley number (or the local radius since ν and ω are the same everywhere). The phase difference between Q and the friction is not considered because the value is vary small [86] and no evidence of clinical relevance about this small quantity is found. In one word, α can be fixed to a value very close to 1.0 and C_f varies across the whole vascular system, whose value must be fitted from observations.

We collect the final form of 1D governing equations in the following:

$$\frac{\partial A}{\partial t} + \frac{\partial Q}{\partial x} = 0, \tag{2.6a}$$

$$\frac{\partial Q}{\partial t} + \frac{\partial}{\partial x}(\alpha \frac{Q^2}{A}) + \frac{A}{\rho}\frac{\partial P}{\partial x} = -C_f \frac{Q}{A}. \tag{2.6b}$$

If we assume $\alpha = 1$, and replace Q by AU, the governing equations can be expressed in another form,

$$\frac{\partial A}{\partial t} + \frac{\partial (AU)}{\partial x} = 0,$$

$$\frac{\partial U}{\partial t} + U\frac{\partial U}{\partial x} + \frac{1}{\rho}\frac{\partial P}{\partial x} = -C_f \frac{U}{A}.$$

Both of those two forms of governing equations are often seen in literature. In this thesis, we choose to use the form in (A, Q, P) because it has a looser limitation on the velocity profile.

2.2.3. Viscoelastic tube law

To close the system, a tube law relating A and P should be given. It has been known for a long time that most biological materials are viscoelastic. For the arterial wall (or

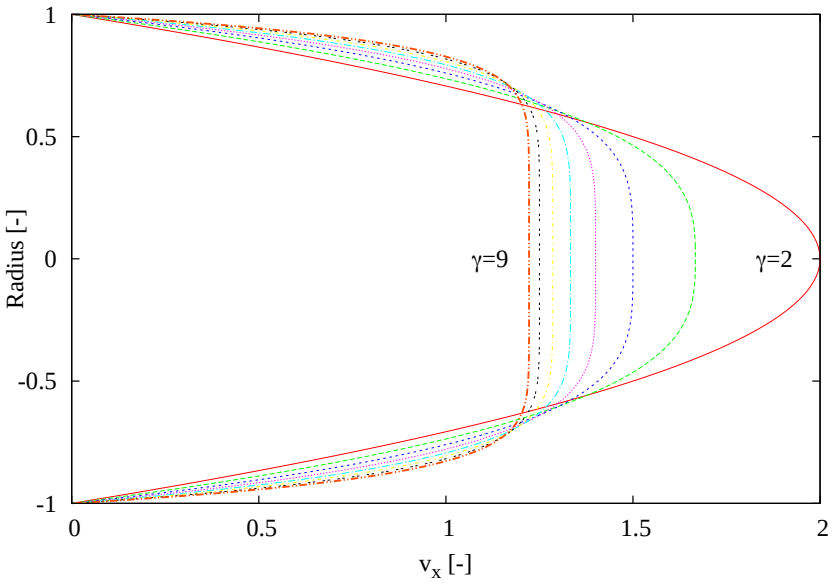

Figure 2.3.: Velocity profile described by the formula proposed by Hughes and Lubliner [35] when $\gamma = 2, 3, \ldots, 9$.

viscoelastic solids in general), when a fixed stress is loaded, the wall keeps extending gradually (creeping) after an instantaneous extension. If we denote the strain as ϵ and the stress as σ, the viscoelastic behaviour can be described as

$$\epsilon(t) = J(0)\sigma(t) + \int_0^\infty j(\tau)\sigma(t-\tau)d\tau,$$

where t is time and $j(t)$ is a creep function.

Writing ϵ and τ in the form $\epsilon = \epsilon_0 e^{i\omega t}$ and $\tau = \tau_0 e^{i\omega t}$, we can derive a complex modulus in analogy to Young's one [32],

$$E^* = \frac{\sigma}{\epsilon} = \left[J(0) + \int_0^\infty j(\tau)e^{-i\omega\tau}d\tau\right]^{-1}.$$

There are several other similar viscoelastic models as presented in [84]. When those models are integrated into a 1D blood flow model, the difference on the prediction of wave form is minor [61, 77]. A disadvantage of those models is the complexity of numerical integration incurred by the convolution when the nonlinear 1D models are solved.

Another widely used viscoelastic model is Kelvin-Voigt model (see Fig. 2.4), which writes,

$$\sigma(t) = E\epsilon(t) + \phi\frac{d\epsilon(t)}{dt}, \tag{2.8}$$

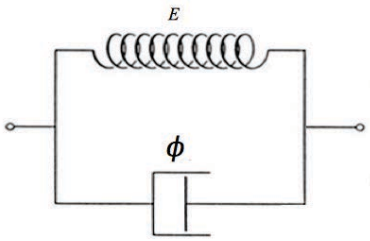

Figure 2.4.: Kelvin-Voigt viscoelastic model. The coefficients for the spring and dashpot are E and ϕ respectively.

where ϕ is a coefficient for the viscosity of the material. The complex modulus for this model is

$$E^* = \frac{\sigma}{\epsilon} = E + i\omega\phi.$$

We note that when $\phi = 0$, this reduces to a pure elastic model. This model is simpler when it is integrated with the 1D fluid model. However, previous studies show that this model captures the viscoelasticity of arteries quite well [2, 4]. Thus we adopt the Kelvin-Voigt model in this thesis.

We consider a cross section of a vessel with a thin wall ($h << R$) as shown in Fig.2.5. We also assume that the arterial wall is isotropic, homogeneous, incompressible, and moreover that it deforms axisymmetrically with each circular cross-section independently of the others. The circumferential strain $\epsilon_{\theta\theta}$ can be expressed as

$$\epsilon_{\theta\theta} = \frac{R - R_0}{(1-\eta^2)R_0}, \tag{2.9}$$

where R_0 is the reference radius without loading and η is the Poisson ratio, which is 0.5 for an incompressible material. By Laplace's law, the transmural difference between the internal pressure P and the external pressre P_{ext} is balanced with the circumferential stress $\sigma_{\theta\theta}$ in the relation

$$P - P_{ext} = \frac{h\sigma_{\theta\theta}}{\pi R}. \tag{2.10}$$

Combining Eq. 2.8, 2.9 and 2.10, we can easily write the tube law in terms of A and P

$$P = P_{ext} + \beta(\sqrt{A} - \sqrt{A_0}) + \nu_s \frac{\partial A}{\partial t}, \tag{2.11}$$

with the stiffness coefficient β,

$$\beta = \frac{\sqrt{\pi}Eh}{(1-\eta^2)A_0},$$

and the viscosity coefficient ν_s,

$$\nu_s = \frac{\sqrt{\pi}\phi h}{2(1-\eta^2)\sqrt{A_0}A}. \tag{2.12}$$

For convenience, we further define $C_v = \frac{A\nu_s}{\rho}$ for reasons which will be clear very soon in the next section.

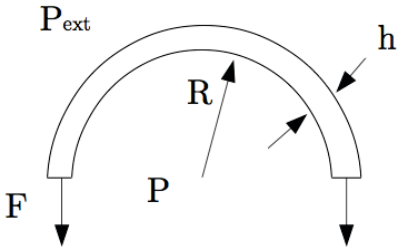

Figure 2.5.: Illustration of the vessel geometry. F is the circumferential tension, h the thickness of the wall, R the internal radius, P the internal pressure and P_{ext} the external pressure.

2.3. Characteristic structure of the system

After presenting the system of equations, we remind its hyperbolic feature by discussing the characteristic structure. The discussion is classical, and can be found in text books [26, 41, 83]. The notations we introduce here will be useful for the discussion of the numerical solvers. We assume P_{ext} is constant along the axial variable x, and substitute the constitutive relation (2.11) into Eq. (7.2). We note that $\frac{\partial A}{\partial t}$ can be replaced by $-\frac{\partial Q}{\partial x}$ thanks to Eq. (7.1). The equation for the balance of momentum turns out to

$$\frac{\partial Q}{\partial t} + \frac{\partial}{\partial x}\left(\frac{Q^2}{A} + \frac{\beta}{3\rho}A^{\frac{3}{2}}\right) - \frac{A}{\rho}\frac{\partial}{\partial x}\left(\nu_s \frac{\partial Q}{\partial x}\right) = -C_f \frac{Q}{A} + \frac{A}{\rho}\left(\frac{\partial(\beta\sqrt{A_0})}{\partial x} - \frac{2}{3}\sqrt{A}\frac{\partial \beta}{\partial x}\right). \quad (2.13)$$

Under the assumption of a small perturbation of A, we approximate the term $\frac{A}{\rho}\frac{\partial}{\partial x}(\nu_s \frac{\partial Q}{\partial x})$ by $C_v \frac{\partial^2 Q}{\partial x^2}$ with the already defined coefficient $C_v = \frac{A\nu_s}{\rho} = \frac{\sqrt{\pi}\phi h}{2\rho(1-\eta^2)\sqrt{A_0}}$, which turns out to be independent of A or Q. Also note that in this part, we set the correction factor of convection term α to be 1.0 for convenience of later analysis. The characteristics are only used to treat boundary conditions at the ends of a vessel segment. Except at the ends, α can still be set a proper value as discussed before.

The governing equations may be written in conservation form as:

$$\frac{\partial U}{\partial t} + \frac{\partial F}{\partial x} = S, \quad (2.14)$$

where

$$U = \begin{pmatrix} A \\ Q \end{pmatrix}, \quad F = F_c + F_v = \begin{pmatrix} Q \\ \frac{Q^2}{A} + \frac{\beta}{3\rho}A^{\frac{3}{2}} \end{pmatrix} + \begin{pmatrix} 0 \\ -C_v \frac{\partial Q}{\partial x} \end{pmatrix}$$

and

$$S = \begin{pmatrix} 0 \\ -C_f \frac{Q}{A} + \frac{A}{\rho}\left(\frac{\partial(\beta\sqrt{A_0})}{\partial x} - \frac{2}{3}\sqrt{A}\frac{\partial \beta}{\partial x}\right) \end{pmatrix}.$$

In this equation, U is the conservative variable, F the corresponding flux and S the source term. Note that the flux (scaled by constant density) consists of two parts, the

convective F_c and the diffusive F_v. We recognize $\frac{Q^2}{A}$ due to the fluid flow, $\frac{\beta}{3\rho}A^{\frac{3}{2}}$ due to the elasticity, and $-C_v\frac{\partial Q}{\partial x}$ due to the viscosity of the wall. In general, the suitable numerical techniques for the convective and diffusive fluxes are different. Thus it is common to separate the diffusive term and put it on the right side. Thus we may write the problem in a convection-diffusion form:

$$\frac{\partial U}{\partial t} + \frac{\partial F}{\partial x} = S + D \tag{2.15}$$

with

$$F = F_c, \quad D = \begin{pmatrix} 0 \\ C_v\frac{\partial^2 Q}{\partial x^2} \end{pmatrix}.$$

We consider firstly the homogeneous part and later the non-homogeneous part. Expanding the derivative of the flux, the homogeneous part can be written in a quasi-linear form

$$\frac{\partial U}{\partial t} + J_c\frac{\partial U}{\partial x} = 0, \tag{2.16}$$

where J_c is the Jacobian matrix

$$J_c = \begin{pmatrix} 0 & 1 \\ \frac{Q^2}{A^2} + c^2 & 2\frac{Q}{A} \end{pmatrix}$$

with the Moens-Korteweg celerity

$$c = \sqrt{\frac{\beta}{2\rho}A^{\frac{1}{2}}}. \tag{2.17}$$

Actually, A is always positive. Therefore c is real, which is the speed of the pressure wave with respect to the fluid flow. The matrix J_c has two different eigenvalues

$$\lambda_{1,2} = \frac{Q}{A} \pm c. \tag{2.18}$$

Linear algebra shows J_c must be diagonalizable in the form $J_c = R\Lambda R^{-1}$. The columns of R are the right eigenvectors of J_c. Left multiplying Eq. (2.16) by R^{-1}, one obtains

$$R^{-1}\frac{\partial U}{\partial t} + R^{-1}R\Lambda R^{-1}\frac{\partial U}{\partial x} = 0.$$

By introducing a new vector which satisfies $\partial_U W = R^{-1}$, the previous equation can be transformed into

$$\frac{\partial W}{\partial t} + \Lambda\frac{\partial W}{\partial x} = 0. \tag{2.19}$$

$W_{1,2}$ can be readily obtained by integrating $\partial_U W = R^{-1}$ componentwise

$$W_{1,2} = \frac{Q}{A} \pm 4c. \tag{2.20}$$

$W = [W_1, W_2]^T$ is called Riemann invariant vector or characteristics. In time-space plane, $W_{1,2}$ are constants along the lines $D_t X_{1,2}(t) = \lambda_{1,2}$. In physiological conditions, $\lambda_1 > 0 > \lambda_2$. The two families of characteristic propagate in opposite directions. The homogeneous part is a subcritical hyperbolic system. For further use, we get the expressions for A and Q by inverting the relation (2.20),

$$A = \frac{(W_1 - W_2)^4}{1024} \left(\frac{\rho}{\beta}\right)^2, \quad Q = A\frac{W_1 + W_2}{2}. \tag{2.21}$$

In the non-homogeneous part, the skin friction term dissipates the momentum and the second order derivative of Q is diffusive. Thus the full system has hyperbolic-parabolic features. In physiological conditions, the Womersley number is not too big and the artery is almost uniform, thus the source term will be very small and the system is dominated by the hyperbolicity feature. If the properties of the artery have sharp variations, large source terms will be introduced. In this case, we will treat the artery as different segments connected together.

2.4. Initial and boundary conditions

2.4.1. Initial conditions

Assume we are interested in the blood flow in an arterial segment $(0, L)$ within a time interval $(0, T)$. For an evolutionary problem, a proper I.C. is needed. In reality, the information contained in I.C. flows out after a certain interval of time, and it will not have influence on the system thereafter. Thus, the I.C. can be set arbitrarily, say, $U(t = 0, x) = (A_0, 0)$, for convenience.

2.4.2. Inlet and outlet of the homogeneous hyperbolic part

Because the system is dominated by the hyperbolicity, it must be driven mainly by the boundary conditions (B.C.) through the first subproblem. Thus we discuss the B.C. of the hyperbolic part in the next subsection and present the treatment of B.C. for the parabolic part in Section 3.2.5 together with Crank-Nicolson scheme.

Assuming the source terms are small, we can impose the B.C. approximately by taking advantage of the characteristic structure of the homogeneous part [25]. Let us look back to the vector Eq. (2.19) again. The two components of this system are

$$\frac{\partial W_1}{\partial t} + \lambda_1 \frac{\partial W_1}{\partial x}(U) = 0, \tag{2.22a}$$

$$\frac{\partial W_2}{\partial t} + \lambda_2 \frac{\partial W_2}{\partial x}(U) = 0. \tag{2.22b}$$

Since the two eigenvalues have opposite signs, there is exactly one incoming characteristic at each end of the computational domain. The incoming characteristic carries

information from outside of the domain and thus is essential to guarantee the problem to be well-posed. That is to say, the system must be supplemented by B.C.s in the form

$$W_1(0,t) = g_1(t), \quad W_2(L,t) = g_2(t), t > 0. \tag{2.23}$$

The outgoing characteristic carries information from inside of the domain, which can be given by the differential equations. Since $W_{1,2}$ are constants along the lines $D_t X_{1,2}(t) = \lambda_{1,2}$ in time-space plane, we can get $W_2^{n+1}(0)$ and $W_1^{n+1}(L)$ by interpolation in the data of the n-th time step:

$$W_2^{n+1}(0) = W_2^n\big(-\lambda_2^n(0)\Delta t\big), \quad W_1^{n+1}(L) = W_1^n\big(L - \lambda_1^n(L)\Delta t\big). \tag{2.24}$$

The characteristics are then transformed to physical variables by relation (2.21) for numerical computation.

In reality, we rarely have the explicit expression (2.23) for the incoming characteristics. Usually, we want to impose B.C. in physical term A, Q or P. At the inlet, if A^{n+1} is given, one can use the relation (2.20) to deduce:

$$W_1^{n+1} = W_2^{n+1} + 8\sqrt{\frac{\beta}{2\rho}\sqrt{A^{n+1}}}.$$

If Q^{n+1} is given, we approximate A^{n+1} by A^n and then obtain

$$W_1^{n+1} = -W_2^{n+1} + 2\frac{Q^{n+1}}{A^n}.$$

If P^{n+1} is given, from the wall relation (2.11) simplified with no viscous effect ($\nu_s = 0$), we in fact impose:

$$W_1^{n+1} = W_2^{n+1} + 8\sqrt{\frac{1}{2\rho}(P^{n+1} + \beta A_0^{1/2})}.$$

At the outlet, some part of the perturbation of outgoing characteristic W_1 may be reflected,

$$W_2^{n+1} = W_2^0 - R_t(W_1^{n+1} - W_1^0),$$

where R_t is the coefficient of reflection. If $R_t = 0$, the B.C. is nonreflecting. That means the outgoing characteristic goes out without leaving any effect and that the incoming characteristic is a constant in time. If there are changes of properties in the downstream of the vessel, usually a nonzero R_t will be incurred.

2.4.3. Conjunction points

There are many cases when conjunctions of different vessels need to be considered: when there are changes of topology, sharp variations in geometrical or mechanical properties. Topological changes correspond to the large amount of bifurcations and some trifurcations in the arterial network. Sharp variations may also arise in many conditions, for example when there are increases of stiffness β due to stenting or A_0 due to aneurysm.

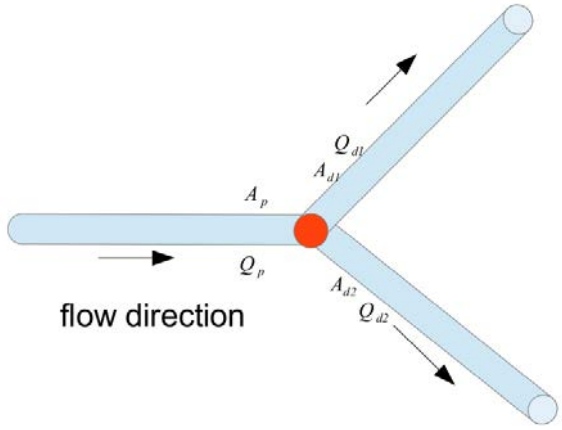

Figure 2.6.: Illustration of a branch. At the conjunction point, there are six unknowns: A_p and Q_p at the outlet of the parent vessel; A_{d_1}, Q_{d_1}, A_{d_2} and Q_{d_2} at the inlets of the daughter vessels.

In these cases, the derivatives of the corresponding variables in the source terms are very large or even near a singularity, and then the vessel can be treated as several joined segments with different properties.

Since all of the conjunction points can be treated with the same method, we consider a branching point as a sample problem: a parent vessel with two daughter arteries (see Fig. 2.6). At the branching point, there are then six boundary conditions, A_p^{n+1} and Q_p^{n+1} for the outlet of the parent artery and $A_{d_1}^{n+1}$, $Q_{d_1}^{n+1}$,$A_{d_2}^{n+1}$ and $Q_{d_2}^{n+1}$ for the inlets of the two daughter arteries. From the physical point of view, we have to preserve the conservation of mass flux

$$Q_p^{n+1} - Q_{d_1}^{n+1} - Q_{d_2}^{n+1} = 0, \tag{2.25a}$$

and conservation of momentum flux

$$\frac{1}{2}\rho(\frac{Q_p^{n+1}}{A_p^{n+1}})^2 + P_p^{n+1} - \frac{1}{2}\rho(\frac{Q_{d_i}^{n+1}}{A_{d_i}^{n+1}})^2 - P_{d_i}^{n+1} = 0 \quad i = 1, 2. \tag{2.25b}$$

The pressures P_p^{n+1} and $P_{d_i}^{n+1}$ shall be expressed in cross-sectional area A by the constitutive relation (2.11). In the Eqs. (2.25b), there may be some terms for energy losses due to the branching [25, 50, 78]. But in practice, these losses only have secondary effects on the pulse waves [50]. Therefore we did not include them.

Moreover, the outgoing characteristics of the joined arteries should be matched. In the parent artery, $(W_1)_p^{n+1}$ is given by the data on the n-th time step with the interpolation formula (2.24). It must be equal to $W_1(U_p^{n+1})$ which is given by relation (2.20). Thus we have the equation

$$(W_1)_p^{n+1} - W_1(U_p^{n+1}) = 0. \tag{2.25c}$$

The same principle holds for W_2 on the two daughter arteries,

$$(W_2)_{d_i}^{n+1} - W_2(U_{d_i}^{n+1}) = 0 \quad i = 1, 2. \tag{2.25d}$$

Combining Eqs. (2.25a), (2.25b), (2.25c) and (2.25d), there are 6 Eqs. with 6 unknowns. This nonlinear algebraic system can be readily solved by Newton-Raphson iterative method with U^n as the initial guess. In our test, the computation converges very fast. Usually a very few iterations are enough for a satisfactory accuracy.

2.5. Conclusion

In this chapter, we derived a viscoelastic 1D model by integrating a simplified conservation equation and Navier-stokes equqtions along the radius of a vessel. The treatment of axial velocity profile and tube law was discussed in detail. The final governing equations of the 1D model form a hyperbolic-parabolic system. The characteristic structure of the hyperbolic part was presented. Noticing that the hyperbolic part dominates the whole problem, we treat the boundary conditions with the characteristic method.

3. Numerical Schemes

3.1. Introduction

In case of weak nonlinearity (i.e. small perturbation around the equilibrium state [42, 59]), we can linearize the 1D governing equations and find analytical solutions in frequency domain [53, 91]. But for the full nonlinear system, analytical solutions are not available yet. Thus several numerical schemes have been proposed and used to solve the system in time domain. We roughly classify them in:

- Finite Difference (FD) [22, 56, 64, 67, 76, 80, 102]
- Finite Volume (FV) [15, 19, 94]
- Finite Element (FE) [2, 25, 46, 71, 87]
- Discontinuous Galerkin (DG) [2, 48, 50, 51, 71]

These schemes have been successfully applied in other communities where researchers have to solve similar hyperbolic problems. For instance, the MacCormack scheme (FD) was principally designed for gas dynamics (i.e. 1D compressible Euler equations) and it was then successfully used to compute blood flow [22, 27]. From ideas frequently applied in shallow water equations, Delestre et al. obtained "well balanced" schemes which properly treat the source term induced by a tapered artery [19]. The 1D model and the numerical solutions have been validated by *in vitro* experimental [2, 67, 92] or *in vivo* clinical data [20, 56, 63, 64, 78, 81]. But usually only one particular scheme was chosen in a study and no cross comparisons among the schemes can be found. Sherwin et al. presented a Taylor-Galerkin (FE) and a DG method in reference [71]. The results of the two methods agree very well in a test case of an idealized vessel implanted with a stent. But no further detailed comparisons were made. Moreover, their work considered an elastic arterial wall instead of a viscoelastic one. In fact, the diffusive term induced by the viscoelasticity needs careful treatment. To our knowledge, there are no discussions in literature on the advantage/drawback of each scheme for a viscoelastic model.

Our objective in this chapter is to make a cross comparison of the four numerical integration schemes and to suggest the suitable conditions of application for each scheme. In general, we note that FD schemes are not flexible enough to treat complex computational geometries in high dimensions (2D or 3D). However, FD, FE and FV schemes of low order accuracy are in fact completely equivalent for 1D linear problems. But for problems with large nonlinearities, solutions with sharp gradient may appear and the performances of different schemes could be different. Equally important is the numerical accuracy. For DG scheme it may be tuned either by the degree of the polynomial or by

the mesh size. But if a diffusive term is added to the governing equations, the term will be hard to treat by an implicit time marching method (e.g. Crank-Nicolson) in the DG setting, thus the time step may be very severely limited. Therefore, the performance of each scheme depends on the main features of the studied problems. In fact, the problems with different main features arise in a wide range of applications. For instance, no shock is observed in arteries in normal physiological conditions but shock-like phenomena may arise in veins [12, 24, 47] or in arteries when the human body suffers from a blunt impact by accident [36]. For another instance, in some conditions diffusive terms or dispersive terms may arise as source terms [2] and the proper treatment of these terms will pose different levels of difficulty in each numerical framework. Thus to make a cross comparison of the numerical schemes is interesting and useful.

In this chapter, Section 3.2 describes the numerical solvers. In particular, a large amount of details of computation are given because this kind of information is scattered in literature. First the hyperbolic-parabolic problem is split into a hyperbolic subproblem and a parabolic one. Then the hyperbolic subproblem is integrated by MacCormack, Taylor-Galerkin and MUSCL schemes and the parabolic subproblem is treated by a Crank-Nicolson method. At the end of this section, a local discontinuous Galerkin method is presented as an alternative approach without operator splitting. Section 3.3 shows the analytical solutions and numerical results of the proposed schemes. The system is linearized and asymptotic solutions are obtained with different source terms in the system. The effects of the skin friction and the viscosity of the wall on the pulse wave are clearly observed. Moreover, a wave with a step jump is computed and the ability of the four schemes to properly capture the shock-like phenomena is tested. After that, a simple bifurcation is computed and the numerical reflection and transmission coefficients are compared with the analytical ones predicted using linearized equations. Finally, a network with 55 arteries is computed. All the numerical solutions are compared favorably with the analytical, semi-analytical solutions or clinical observations. In the last section, comparisons among the four schemes are made in four important aspects: accuracy, ability to capture shock-like phenomena, computational speed and implementation complexity. The suitable conditions for the application of each scheme are discussed.

3.2. Numerical solvers

Having defined the problem and notations, in this section we present the numerical solvers. In one approach, we split the original problem into two subproblems which are respectively hyperbolic and parabolic. Three numerical schemes are presented to treat the hyperbolic subproblem. For the parabolic subproblem, Crank-Nicolson method is suitable. In another approach, we presented a local discontinuous Galerkin scheme to solve the problem without splitting.

3.2.1. Operator splitting

There are explicit high resolution schemes for hyperbolic problems. But for parabolic problems, implicit schemes are necessary in general for a reasonable time step for time

integration. Thus we applied a fractional step or operator splitting method. Starting from Eq. (2.15), the original problem is split into to a hyperbolic subproblem,

$$\frac{\partial U}{\partial t} + \frac{\partial F}{\partial x} = S \tag{3.1}$$

and a parabolic one,

$$\frac{\partial U}{\partial t} = D. \tag{3.2}$$

Let us consider the time intervals (t^n, t^{n+1}), for $n = 0, 1, ...$, with $t^n = n\Delta t$. In every time interval, the hyperbolic problem is solved to get a predictor U^*, which is used as the initial condition (I.C.) of the second problem. The second step can be viewed as a corrector. The original problem is approximated by a sequential application of the two subproblems in a certain order.

From data U^n, we may make a prediction U^* by evolving time Δt of the hyperbolic subproblem, and correct it with the evolution over Δt of the parabolic subproblem,

$$U^n \xrightarrow{e^{\Delta t\mathcal{H}}} U^* \xrightarrow{e^{\Delta t\mathcal{P}}} U^{n+1},$$

where $e^{\Delta t\mathcal{H}}$ ($e^{\Delta t\mathcal{P}}$) means to solve the hyperbolic (parabolic) subproblem over Δt. This method is called Godunov splitting. If the two subproblems are not commutable, the splitting error is $\mathcal{O}(\Delta t)$, see Chapter 17 of reference [41].

There is a 3-stage splitting called Strang splitting, which has a leading error term $\mathcal{O}(\Delta t^2)$,

$$U^n \xrightarrow{e^{\frac{1}{2}\Delta t\mathcal{P}}} U^* \xrightarrow{e^{\Delta t\mathcal{H}}} U^{**} \xrightarrow{e^{\frac{1}{2}\Delta t\mathcal{P}}} U^{n+1}.$$

But in most cases the errors induced by the two splittings are very close. That is because the coefficient of the term $\mathcal{O}(\Delta t)$ is much smaller then the coefficient of $\mathcal{O}(\Delta t^2)$ [41]. We will see in Section 3.3.3 a test case on the diffusion term. The results show that the Godunov splitting is sufficient for our problem.

3.2.2. MacCormack scheme

In FD framework, MacCormack method [45] is very suitable for nonlinear hyperbolic systems of conservation laws. It is equivalent to the Lax-Wendroff scheme for linear systems. It has the following characteristics: conservative form, three-point spatial stencil and two time levels (predictor and corrector), second-order accuracy in time and space.

The numerical solution is performed in a mesh with $N+1$ points and thus the spatial resolution is $\Delta x = \frac{L}{N}$, see Figure 3.1. For the conservative system (3.1), an approximate solution $\mathbf{U}^*$ is obtained first from $\mathbf{U}^n$ and then $\mathbf{U}^*$ is corrected to give the solution $\mathbf{U}^{n+1}$ at the time step $t + \Delta t$. The finite difference equations (at the interior grid points) are then :

1. predictor step

$$U_i^* = U_i^n - \frac{\Delta t}{\Delta x}(F_{i+1}^n - F_i^n) + \Delta t S_i^n, \quad i = 2, ...N$$

2. corrector step

$$U_i^{n+1} = \frac{1}{2}(U_i^n + U_i^*) - \frac{\Delta t}{2\Delta x}(F_i^* - F_{i-1}^*) + \frac{\Delta t}{2}S_i^*, \quad i = 2, ...N$$

where $\mathbf{F}^*$ and $\mathbf{S}^*$ are evaluated as functions of the predicted solution $\mathbf{U}^*$. Note that the predictor step applies a forward differencing and the corrector step a backward differencing. The order of the two kinds of differencing can be reversed. The grid points x_1 and x_{N+1} represent the boundary conditions.

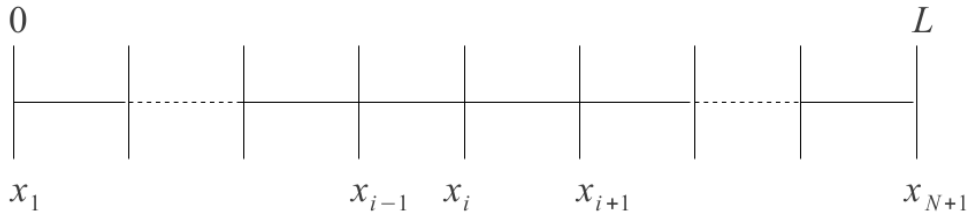

Figure 3.1.: Mesh for FD and FE

3.2.3. Taylor-Galerkin scheme

In this section, we follow the presentations of Formaggia et al. [25, 26] and Sherwin et al. [71] for the Taylor-Galerkin scheme. Other forms are also possible, see the reference [89] for example.

From Eq. (3.1), one may obtain,

$$\frac{\partial U^n}{\partial t} = S^n - \frac{\partial F^n}{\partial x}. \tag{3.3}$$

Differentiating both sides with respect to t and exchanging the order of spatial and temporal differentiations in the second term give

$$\frac{\partial^2 U^n}{\partial t^2} = \Big(S_U \frac{\partial U}{\partial t}\Big)^n - \frac{\partial}{\partial x}\Big(H \frac{\partial U}{\partial t}\Big)^n, \tag{3.4}$$

where $S_U = \frac{\partial S}{\partial U}$ and $H = \frac{\partial F}{\partial U}$. Substituting Eq. (3.3) into Eq. (3.4) and then both of them into the Taylor series of U^{n+1} up to the second order, one gets,

$$\begin{aligned} U^{n+1} = U^n - \Delta t \frac{\partial}{\partial x}\big[F^n + \frac{\Delta t}{2} H^n S^n\big] - \frac{\Delta t^2}{2}\big[S_U^n \frac{\partial F^n}{\partial x} - \frac{\partial}{\partial x}\big(H^n \frac{\partial F^n}{\partial x}\big)\big] \\ + \Delta t\big(S^n + \frac{\Delta t}{2} S_U^n S^n\big). \end{aligned} \tag{3.5}$$

For convenience, we adopt the notations

$$F_{LW}(U) = F(U) + \frac{\Delta t}{2} H(U) S(U),$$
$$S_{LW}(U) = S(U) + \frac{\Delta t}{2} S_U(U) S(U).$$

The piecewise linear function space associated with the mesh (Figure 3.1) is given as

$$V_h^0 = \{[v_h]^2 | v_h \in \mathcal{C}^0, v_h|_{[x_i, x_{i+1}]} \in \mathcal{C}^1, v_h(0) = v_h(L) = 0, i = 1...N\}.$$

This is both the trial function space and the test function space in Galerkin framework. We further define the inner product

$$(U, V) = \int_0^L U \cdot V dx.$$

At the interior points $x_2, ...x_N$, if we approximate U by $U_h \in V_h^0$ in Eq. (3.5), multiply both sides by basis test functions $\psi_i \in V_h^0$, and integrate over the domain $[0, L]$, finally we can get

$$\begin{aligned}(U_h^{n+1}, \psi_i) = (U_h^n, \psi_i) + \Delta t\big(F_{LW}(U_h^n), \frac{d\psi_i}{dx}\big) - \frac{\Delta t^2}{2}\big(S_U(U_h^n)\frac{\partial F(U_h^n)}{\partial x}, \psi_i\big) \\ -\frac{\Delta t^2}{2}\big(H(U_h^n)\frac{\partial F(U_h^n)}{\partial x}, \frac{d\psi_i}{dx}\big) + \Delta t(S_{LW}(U_h^n), \psi_i)\end{aligned} \tag{3.6}$$

In computation, we enforce the Eq. (3.6) componentwise. That is,

$$\begin{aligned}(A_h^{n+1}, v_i) &= RHS1_i^n, \\ (Q_h^{n+1}, v_i) &= RHS2_i^n,\end{aligned}$$

where v_i is one component of the vector ψ_i and

$$\begin{aligned}RHS1_i^n = (A_h^n, v_i) + \Delta t\Big(\big[F_{LW}(U_h^n)\big]_1, \frac{dv_i}{dx}\Big) - \frac{\Delta t^2}{2}\Big(\big[S_U(U_h^n)\frac{\partial F(U_h^n)}{\partial x}\big]_1, v_i\Big) \\ -\frac{\Delta t^2}{2}\Big(\big[H(U_h^n)\frac{\partial F(U_h^n)}{\partial x}\big]_1, \frac{dv_i}{dx}\Big) + \Delta t\Big(\big[S_{LW}(U_h^n)\big]_1, v_i\Big).\end{aligned} \tag{3.7}$$

The form $[\cdot]_1$ indicates the first component of the vector in the bracket. $RHS2_i^n$ can be expressed in a similar way.

To elaborate the computing details, we take the Eq. (3.7) as an example. In the FE framework, A_h^{n+1} and A_h^n are expanded as $A_h = \sum_{j=2}^{j=N} A_j v_j$. We denote the unknown vector $(A_2, \dots A_N)^T$ by $\mathbf{A}$. Instead of evaluated directly as nonlinear functions of U_h^n, the terms $F(U_h^n)$, $F_{LW}(U_h^n)$, $S_{LW}(U_h^n)$, $S_U(U_h^n)$ and $H(U_h^n)$ are projected onto the trial function space and expanded by a group finite element method. That is, for example, $[F(U_h^n)]_1 = \sum_{j=2}^{j=N} [F_j^n]_1 v_j$ with $[F_j^n]_1 = [F(U_j^n)]_1$. Finally, the matrix form of Eq. (3.7) writes

$$\begin{aligned}\mathcal{M}\mathbf{A}^{n+1} = \mathcal{M}\mathbf{A}^n + \Delta t\mathcal{K}^T[\mathbf{F}_{LW}^n]_1 - \frac{\Delta t^2}{2}(\tilde{\mathcal{M}_1}[\mathbf{F}^n]_1 + \tilde{\mathcal{M}_2}[\mathbf{F}^n]_2) \\ -\frac{\Delta t^2}{2}(\tilde{\mathcal{K}_1}[\mathbf{F}^n]_1 + \tilde{\mathcal{K}_2}[\mathbf{F}^n]_2) + \Delta t\mathcal{M}[\mathbf{S}_{LW}^n]_1,\end{aligned} \tag{3.8}$$

where

$$\mathcal{M}_{ij} = (v_i, v_j), \quad \mathcal{K}_{ij} = (v_i, \frac{\partial v_j}{\partial x})$$

and

$$\tilde{\mathcal{M}}_1(S_u)_{ij} = \Big(\sum_k (S_u^{(1,1)})_k v_k \frac{\partial v_i}{\partial x}, v_j \Big), \quad \tilde{\mathcal{M}}_2(S_u)_{ij} = \Big(\sum_k (S_u^{(1,2)})_k v_k \frac{\partial v_i}{\partial x}, v_j \Big),$$
$$\tilde{\mathcal{K}}_1(H)_{ij} = \Big(\sum_k H_k^{(1,1)} v_k \frac{\partial v_i}{\partial x}, \frac{\partial v_j}{\partial x} \Big), \quad \tilde{\mathcal{K}}_2(H)_{ij} = \Big(\sum_k H_k^{(1,2)} v_k \frac{\partial v_i}{\partial x}, \frac{\partial v_j}{\partial x} \Big).$$

The form $(S_u^{(\cdot,\cdot)})_k$ indicates the k-th component of the vector at the position $(\cdot,\cdot)$ of the discretized matrix $\mathbf{S}_u$. Please note that the operators $\tilde{\mathcal{M}}_1$ etc. are functions of $\mathbf{S}_u$ and $\mathbf{H}$, therefore they must be updated in every time step.

3.2.4. MUSCL

In this section, we mainly follow the presentation [19] but with a different temporal integration method. For finite volume method, the domain is decomposed into finite volumes or cells with vertex x_i as the center of cell $[x_{i-1/2}, x_{i+1/2}]$, see Figure 3.2. In every cell, the conservation law must hold,

$$\int_{x_{i-1/2}}^{x_{i+1/2}} \frac{\partial U}{\partial t} dx + \int_{x_{i-1/2}}^{x_{i+1/2}} \frac{\partial F}{\partial x} dx = \int_{x_{i-1/2}}^{x_{i+1/2}} S dx.$$

Application of Gauss's theorem on the second term gives

$$\int_{x_{i-1/2}}^{x_{i+1/2}} \frac{\partial U}{\partial t} dx + F|_{x_{i+1/2}} - F|_{x_{i-1/2}} = \int_{x_{i-1/2}}^{x_{i+1/2}} S dx. \tag{3.9}$$

In the cells, average values are considered,

$$U_i = \frac{1}{\Delta x} \int_{x_{i-1/2}}^{x_{i+1/2}} U(x) dx, \quad S_i = \frac{1}{\Delta x} \int_{x_{i-1/2}}^{x_{i+1/2}} S(x) dx.$$

Thus Eq. 3.9 turns into an ordinary differential equation

$$\frac{dU_i}{dt} = -\frac{(F|_{x_{i+1/2}} - F|_{x_{i-1/2}})}{\Delta x} + S_i. \tag{3.10}$$

We have a local Riemann problem at each interface of neighboring cells, since $U_{i+1/2-}$ and $U_{i+1/2+}$, the left limit of U_i and the right limit of U_{i+1} at $x_{i+1/2}$ respectively, are not equal in general. By solving the Riemann problem, a numerical flux F^* can be obtained. Depending on the approximate approaches on solving the Riemann problem, different numerical fluxes are possible. Among them, Rusanov (or called local Lax-Friedrichs) flux is widely used. According to reference [11], it writes

$$F^*_{i+1/2} = \frac{F(U_{i+1/2-}) + F(U_{i+1/2+})}{2} - c\frac{U_{i+1/2+} - U_{i+1/2-}}{2},$$

with

$$c = \max\big(\lambda_1(U_{i+1/2-}), \lambda_1(U_{i+1/2+})\big),$$

where λ_1 is the biggest eigenvalue of J_c. Other numerical fluxes with less numerical diffusivity are possible, such as Harten-Lax-van Leer (HLL) flux [11, 19]. Since Rusanov flux is more simple and robust, it is adopted in this paper. If $\mathbf{U}_-$ and $\mathbf{U}_+$ are equal to the average values at the cells, the scheme will be of first order accuracy. Reconstructions of $\mathbf{U}_-$ and $\mathbf{U}_+$ from $\mathbf{U}$ are necessary for a scheme of higher resolution.

Let us consider the techniques of reconstruction. For a scalar s within the i-th cell, we denote its slope as Ds_i, which can be approximated by $(s_i - s_{i-1})/\Delta x$, $(s_{i+1} - s_i)/\Delta x$ or $(s_{i+1} - s_{i-1})/2\Delta x$. Then the values of s at the interfaces associated with this cell can be recovered as

$$s_{i-1/2+} = s_i - \frac{\Delta x}{2} Ds_i, \quad s_{i+1/2-} = s_i + \frac{\Delta x}{2} Ds_i.$$

The discretization of derivative in space can achieve a second order accuracy by this method. But the solution will have nonphysical oscillations. Some examples of oscillations induced by these methods can be found in Chapter 6 of reference [41]. Slope or flux limiter and non-oscillatory solutions are integral characteristics of FV schemes. MUSCL (monotonic upwind scheme for conservation law) is one popular slope limited linear reconstruction technique. To present MUSCL, we first define a slope limiter,

$$\text{minmod(x,y)} = \begin{cases} \min(\text{x,y}) & \text{if } x, y \geq 0, \\ \max(\text{x,y}) & \text{if } x, y \leq 0, \\ 0 & \text{else} \end{cases}$$

Then the slope Ds_i is modified as

$$Ds_i = \text{minmod}(\frac{s_i - s_{i-1}}{\Delta x}, \frac{s_{i+1} - s_i}{\Delta x}).$$

The values of $\mathbf{U}_-$ and $\mathbf{U}_+$ at the interfaces can be obtained as

$$A_{i-1/2+} = A_i - \frac{\Delta x}{2} DA_i, \quad A_{i+1/2-} = A_i + \frac{\Delta x}{2} DA_i$$

and

$$Q_{i-1/2+} = Q_i - \frac{\Delta x}{2} DQ_i, \quad Q_{i+1/2-} = Q_i + \frac{\Delta x}{2} DQ_i.$$

It is easy to verify that the variables are conserved by this reconstruction

$$\frac{A_{i-1/2+} + A_{i+1/2-}}{2} = A_i, \quad \frac{Q_{i-1/2+} + Q_{i+1/2-}}{2} = Q_i.$$

After the discretization in space, we have the semi-discrete form,

$$\frac{dU_i}{dt} = \Phi(U_{i-2}, ...U_{i+2})$$

where

$$\Phi(U_{i-2}, ...U_{i+2}) = -\frac{(F^*_{i+1/2} - F^*_{i-1/2})}{\Delta x} + S_i.$$

The numerical fluxes $F^*_{i+1/2}$ and $F^*_{i-1/2}$ are given by Rusanov flux with the reconstructed values at the two sides of the interfaces. Note that this is a scheme with five stencils. The values at x_1 and x_{N+1} are determined by the aforementioned characteristic method. One ghost cell at each end of the computational domain is needed and we approximate the values at these cells by the ones at the neighboring boundary cells.

For the temporal integration, we may apply a 2-step second order Adams-Bashforth (A-B) scheme,

$$\mathbf{U}^{n+1} = \mathbf{U}^n + \Delta t\big(\frac{3}{2}\Phi(\mathbf{U}^n) - \frac{1}{2}\Phi(\mathbf{U}^{n-1})\big).$$

This scheme can be initiated by a forward Euler method. Also, a second order Runge-Kutta (R-K) approach, namely Heun method is possible [75]. It writes

$$\begin{aligned}\mathbf{U}^* &= \mathbf{U}^n + \Delta t\Phi(\mathbf{U}^n),\\ \mathbf{U}^{**} &= \mathbf{U}^* + \Delta t\Phi(\mathbf{U}^*),\\ \mathbf{U}^{n+1} &= (\mathbf{U}^* + \mathbf{U}^{**})/2.\end{aligned}$$

Comparing the two methods, we note that $\Phi(\mathbf{U})$ has to be computed twice in R-K in every time step while the A-B method only needs once since $\Phi(\mathbf{U}^{n-1})$ is stored in the previous step and reused in the current step. Because the boundary conditions are determined dynamically to compute $\Phi(\mathbf{U})$, the R-K also incurs one more resolution of the nonlinear algebraic equations at conjunction points. For these reasons, we choose the A-B method for the temporal integration, although the R-K method usually allows a larger time step for convergence.

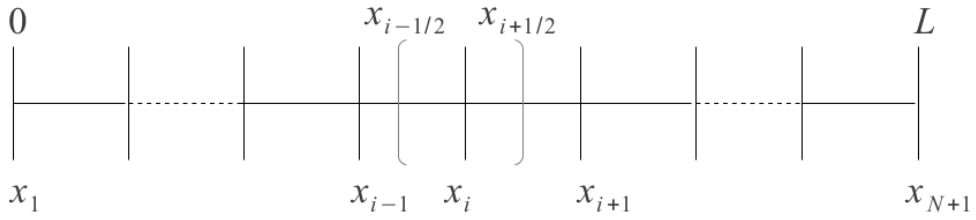

Figure 3.2.: Mesh for FV

3.2.5. Treatment of the parabolic subproblem

For the previous 3 schemes, only the hyperbolic subproblem resulted from splitting is solved. For the parabolic subproblem, Crank-Nicolson method is very suitable. The temporal and spatial discretization has the form,

$$\frac{U_i^{n+1} - U_i^*}{\Delta t} = \frac{C_v}{2}\big(\frac{U_{i+1}^{n+1} - 2U_i^{n+1} + U_{i-1}^{n+1}}{\Delta x^2} + \frac{U_{i+1}^* - 2U_i^* + U_{i-1}^*}{\Delta x^2}\big),$$

where $\mathbf{U}^*$ is the solution of the first hyperbolic subproblem. The matrix of the resulting algebraic system is tridiagonal, which is quite cheap to invert. This scheme is second

order accurate both on time and space. Moreover, it is unconditionally stable. It is natural to set a homogeneous Neumann B.C. for the parabolic subproblem, $\partial_x U_p(0,t) = \partial_x U_p(L,t) = 0$. The subscript p stands for parabolic. We note that a second-order implicit FE method can also be applied here. But since this subproblem is linear and is in 1D, the FE method would be exactly equivalent to this FD method.

3.2.6. Local Discontinuous Galerkin scheme

In the FV framework, the recovery of $\mathbf{U}_-$ and $\mathbf{U}_+$ of higher accuracy requires a big stencil. In higher dimensions, this kind of reconstruction leads to difficulties if the mesh is unstructured. On the other hand, it is quite straightforward to increase the order of approximation polynomials in one finite element. Unlike the global FE, the neighboring elements do not share the same values at the interfaces. Numerical fluxes are obtained from these values, where the dynamics of the system can be considered. We present a nodal DG scheme, following Hesthaven and Warburton's book [31]. The domain is decomposed into K non-overlapping elements, see Figure 3.3. At each element, the local approximation to the solution is a polynomial of order $N = N_p - 1$. The global approximation to U is the direct summation of these local solutions:

$$U_h = \bigoplus_{k=1}^{k=K} U_h^k. \tag{3.11}$$

Similarly, the flux F and the source term S can also be approximated by the direct summation of piecewise N-th degree polynomials. The local form of the conservation law on the k-th element is

$$\frac{\partial U_h^k}{\partial t} + \frac{\partial F_h^k}{\partial x} = S_h^k. \tag{3.12}$$

Multiplying both sides of Eq. (3.12) with a test function ψ^k, and integrating over one element give

$$\left(\frac{\partial U_h^k}{\partial t}, \psi^k\right)_{D_k} + \left(\frac{\partial F_h^k}{\partial x}, \psi^k\right)_{D_k} = \left(S_h^k, \psi^k\right)_{D_k}. \tag{3.13}$$

Applying integration by part on the second term, we have:

$$\left(\frac{\partial U_h^k}{\partial t}, \psi^k\right)_{D_k} - \left(F_h^k, \frac{\partial \psi^k}{\partial x}\right)_{D_k} + F_h^k \psi^k \Big|_{x_k}^{x_{k+1}} = \left(S_h^k, \psi^k\right)_{D_k}. \tag{3.14}$$

At the interface of x_k, the values of U_h at the two sides, $U_h^{k-1}(x_k)$ and $U_h^k(x_k)$, are not guaranteed equal. A numerical flux F_k^* is introduced here. Through the numerical flux, information is communicated between elements. In practice, the second term is integrated by part again for convenience of computation. Thus we have

$$\left(\frac{\partial U_h^k}{\partial t}, \psi^k\right)_{D_k} + \left(\frac{\partial F_h^k}{\partial x}, \psi^k\right)_{D_k} + \psi^k(-F_h^k + F^*)\Big|_{x_k}^{x_{k+1}} = \left(S_h^k, \psi^k\right)_{D_k}. \tag{3.15}$$

If we introduce N_p nodes within the element D_k (Figure 3.3), the local solution can be expanded as

$$U_h^k(x,t) = \sum_{i=1}^{N_p} U_h^k(x_i^k,t)\ell_i^k(x), \tag{3.16}$$

where $\ell_i^k(x)$ is the Lagrange interpolant associated with the i-th node. For the Galerkin scheme, Eq. (3.15) must hold for every test function $\ell_i^k(x)$. Thus we have N_p equations for N_p unknowns. In matrix form, the system can be written as,

$$\mathcal{M}^k \frac{d\mathbf{U}^k}{dt} + \mathcal{K}^k \mathbf{F}^k + \boldsymbol{\ell}^k(-F_h^k + F^*)\Big|_{x_k}^{x_{k+1}} = \mathcal{M}^k \mathbf{S}^k, \tag{3.17}$$

where

$$\mathcal{M}_{(i,j)}^k = \left(\ell_i^k, \ell_j^k\right)_{D_k}, \quad \mathcal{K}_{(i,j)}^k = \left(\ell_i^k, \frac{d\ell_j^k}{dx}\right)_{D_k},$$

and $\boldsymbol{\ell}^k$ is the vector of functions $(\ell_1^k, \ell_2^k, ..\ell_{N_p}^k)^T$. The system of equations can be turned into a semi-discrete form,

$$\frac{d\mathbf{U}^k}{dt} = -\mathcal{D}^k \mathbf{F}^k + (\mathcal{M}^k)^{-1}\boldsymbol{\ell}^k(F_h^k - F^*)\Big|_{x_k}^{x_{k+1}} + \mathbf{S}^k, \tag{3.18}$$

where

$$\mathcal{D}_{(i,j)}^k = \left((\mathcal{M}^k)^{-1}\mathcal{K}^k\right)_{(i,j)} = \left.\frac{d\ell_j^k}{dr}\right|_{r_i}$$

is the local differentiation operator [31]. The computation of $\mathcal{M}^k$ and $\mathcal{D}^k$ is crucial. We define an affine mapping from a reference element $(-1,1)$ to D_k,

$$x(r) = x_k + \frac{1+r}{2}(x_{k+1} - x_k).$$

The local operators can be readily computed as

$$\mathcal{M}_{(i,j)}^k = \mathcal{J}_k \int_{-1}^{1} \ell_i \ell_j dr, \quad \mathcal{D}_{(i,j)}^k = \mathcal{J}_k^{-1} \left.\frac{d\ell_j}{dr}\right|_{r_i},$$

where $\mathcal{J}_k = (x_{k+1} - x_k)/2$ and ℓ_i, ℓ_j are the Lagrange interpolants at the reference element. Note that the operators $\mathcal{M}^k$ and $\mathcal{D}^k$ can be precomputed and stored. Legendre-Gauss-Lobatto points have to be chosen as the interpolation points to minimize computation error. For more details, we refer to Chapter 3 of reference [31]. For the temporal integration, a second order A-B scheme is applied for reasons as discussed in Section 3.2.4.

The scheme previously presented can treat a hyperbolic problem. But in this setting Crank-Nicolson method is hard to apply, because the values at the interfaces are duplicated. We consider the problem formulation of Eq. (2.14), where the flux contains convective part F_c and diffusive part F_v. For the convective part, Rusanov flux as mentioned in Section 3.2.4 is applicable. For the diffusive flux, a straight idea is to use the

central flux, $(F_v(U_-) + F_v(U_+))/2$. But as pointed out by Shu el al. [74], this choice is inconsistent.

To solve this problem, we rewrite the original equations as

$$\frac{\partial U}{\partial t} + \frac{\partial (F_c - C_v q)}{\partial x} = S$$
$$q - \frac{\partial Q}{\partial x} = 0$$

In semi-discrete form, the equations for one element are

$$\frac{d\mathbf{U}_k}{dt} = -\mathcal{D}^k \mathbf{F}^k + (\mathcal{M}^k)^{-1} \boldsymbol{\ell}^k (F_h^k - F^*)\Big|_{x_k}^{x_{k+1}} + \mathbf{S}^k$$
$$\mathbf{q}^k = \mathcal{D}^k \mathbf{Q}^k - (\mathcal{M}^k)^{-1} \boldsymbol{\ell}^k (Q_h^k - Q^*)\Big|_{x_k}^{x_{k+1}}$$

The fluxes in these equations have to be modified accordingly: $\mathbf{F}^k = \mathbf{F}_c^k - C_v \mathbf{q}^k$, $F_h^k = (F_c)_h^k - C_v q_h^k$ and $F^* = F_c^* - (C_v q)^*$. The convective flux F_c^* is defined by Rusanov flux. The fluxes $(C_v q)^*$ and Q^* are defined by the central flux. The introduction of an auxiliary variable q stabilizes the scheme. Note that the auxiliary equation does not involve time evolution. The computation and storage of $\mathbf{q}^k$ incur very limited extra costs. This method is called local discontinuous Galerkin scheme.

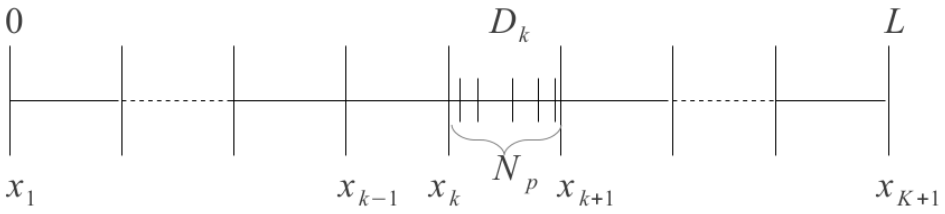

Figure 3.3.: Mesh for DG

3.3. Verification and comparison among schemes

The implementation codes can be verified by analytical solutions of linearized model or manufactured solutions of the full system without linearization [60, 61]. In this paper, except comparisons with the homogeneous linearized model and results in literature, we derived asymptotic solutions with different source terms. The verification by asymptotic analysis is a different approach from previous works. In this section, the computations are done on a single uniform vessel at first. In case of small perturbations, a linearized system is obtained. If this system is homogeneous, it allows pure wave solution. If the source terms due to the skin friction and the viscosity of the wall are added respectively,

asymptotic solutions are obtained. In case of larger perturbations, the full nonlinear system allows shocks. The shock-capturing property of each scheme is tested in this case. After the tests on a single vessel, a simple bifurcation is computed and the reflection and transmission coefficients are compared with analytical ones predicted by linearized system. At the end of this section, a network with 55 arteries is computed and the numerical solutions are checked against clinical observations reported in literature.

3.3.1. Propagation in a uniform tube

In this subsection, we compare the numerical results with analytical ones for a pulse wave on a single uniform vessel ($\partial_x(\beta\sqrt{A_0}) = \partial_x\beta = 0$). To avoid reflections, nonreflecting B.C. is set at the outflow to mimic a semi-infinite tube. Adding a small perturbation $((\epsilon\tilde{A}, \epsilon\tilde{Q}))$ to the equilibrium solution ($U = (A_0, 0)$), substituting it into the governing equations and dropping the terms with quadratics of ϵ, we obtain the equations for the perturbations in a linear form:

$$\frac{\partial\tilde{A}}{\partial t} + \frac{\partial\tilde{Q}}{\partial x} = 0, \quad \frac{\partial\tilde{Q}}{\partial t} + c_0^2\frac{\partial\tilde{A}}{\partial x} = -\frac{C_f}{A_0}\tilde{Q} + C_v\frac{\partial^2\tilde{Q}}{\partial x^2} \tag{3.19}$$

with $c_0 = \sqrt{\frac{\beta}{2\rho}\sqrt{A_0}}$, the Moens-Korteweg celerity. To investigate the propagation phenomena at first, we drop the non-homogeneous part ($C_f = 0$ and $C_v = 0$). Then Eqs. (3.19) become d'Alembert equations, which admit the pure wave solution. We assume that the initial condition is at equilibrium and the inflow is prescribed as $Q(0,t) = Q_{in}(t)$ with

$$Q_{in}(t) = Q_c \sin(\frac{2\pi}{T_c}t)H(-t + \frac{T_c}{2}), \quad t > 0,$$

where $H(t)$ is the Heaviside function, T_c the period of the sinusoidal wave and Q_c the amplitude. The solution is $c_0\tilde{A} = \tilde{Q} = Q_{in}(x - c_0t)$, which means that the waveform propagates to the right with a speed of c_0.

We propose a numerical test with parameters of the tube inspired by [71]: $L = 250$cm, $A_0 = 3.2168\text{cm}^2$, $\beta = 1.8734 \times 10^6$Pa/m, $\rho = 1.050 \times 10^3\text{kg/m}^3$, and accordingly $c_0 = 400$cm/s. To impose a small perturbation, we choose $Q_c = 1$ml/s and $T_c = 0.4$s. In this case the change ratio of the radius is $\Delta R/R_0 = Q_c/(2A_0c_0) = 0.04\%$, thus the perturbation is assured small enough. We take the linearized analytical solution at time $t = 0.4s$ as reference to compute the errors of the numerical solutions. The normalized error is defined by $||E|| = ||\mathbf{Q}_{numerical} - \mathbf{Q}_{analytical}||_{rms}/Q_c$, where $||\cdot||_{rms}$ stands for the root-mean-square error. To specify the time step, we note that it first should satisfy the CFL (Courant-Friedrichs-Lewy) condition which writes

$$\Delta t \leqslant n_{CFL}\min_{i=0}^{N+1}\Big[\frac{h_i}{\max(\frac{Q_i}{A_i} + c_i, \frac{Q_{i+1}}{A_{i+1}} + c_{i+1})}\Big],$$

where h_i is the element (cell) size. For the second order Taylor-Galerkin scheme, a linear stability analysis shows that $n_{CFL} = \frac{\sqrt{3}}{3}$ [25]. For the second order MUSCL,

$n_{CFL} = \frac{1}{2}$ [19]. Practice shows that $n_{CFL} = 1$ for MacCormack scheme [22]. A sharp estimation of the coefficient n_{CFL} for the DG scheme is challenging. We define an approximate formula, $\Delta t = C_t \frac{L}{Nc_0}$, to test the stability. In our test, the approximate threshold values of C_t for the schemes to become unstable are: 0.5 for MUSCL, 0.56 for Taylor-Galerkin and 1.0 for MacCormack. The results agree with the report in literature. For the DG scheme, the time step formula is modified accordingly as $\Delta t = \frac{C_t}{\mathcal{P}} \frac{L}{Nc_0}$, with $\mathcal{P}$ the degree of the polynomial. For the DG scheme, C_t can not be greater than 0.1 (see Figure 3.4(b)).

To further test the temporal convergence, we fix the mesh ($N_{TG} = N_{FV} = N_{FD} = 800$, $N_{DG-\mathcal{P}_1} = N_{DG-\mathcal{P}_2} = 100$) and plot the numerical errors as a function of C_t (see Figure 3.4(a)). The errors vary slightly for all of the schemes except MUSCL. For the convergence of the temporal integration, the MUSCL scheme has to choose a smaller time step than the value prescribed by the CFL condition. But note this is only a test in linear case, in practical applications, the coefficient C_t may be much smaller for convergence (Section 3.3.6).

To test the spatial convergence, we fix $C_t = 0.1$, and vary the number of mesh nodes N. The log-log plot of $||E||$ against Δx can be seen in Figure 3.4(c). We have two main observations. First, all of the schemes converge with an order between 1 and 2 and the DG scheme converges faster (see Figure 3.4(c)). Second, as shown by Figure 3.4(d) the differences between the analytical solution and all of the numerical solutions are hardly discernible with a moderate number of mesh points ($N_{TG} = N_{FV} = N_{FD} = 800$, $N_{DG-\mathcal{P}_1} = N_{DG-\mathcal{P}_2} = 100$).

To compare the actual speed and accuracy of the four schemes, we set N and C_t (see Table 3.1) such that the errors achieve the same order of magnitude (see Figure 3.4(f)). Except the Taylor-Galerkin scheme, all the schemes have the similar accuracy with very close running time (see Figure 3.4(e) and 3.4(f)). At this point, the Taylor-Galerkin scheme shows the worst accuracy and needs to run the longest time. We note that large global matrices arise in Taylor-Galerkin scheme while the operators in other schemes are local and have small size. That explains the relative poor performance of Taylor-Galerkin even though a larger time step is allowed by this scheme. We will see that in case of a network of real size, the largest number of N is about 100 and Taylor-Galerkin shows a good balanced property between accuracy and speed (Section 3.3.6).

scheme	N	C_t
Taylor-Galerkin	800	0.5
MUSCL	800	0.3
MacCormack	1600	0.5
DG-$\mathcal{P}_1$	200	0.1
DG-$\mathcal{P}_2$	100	0.1

Table 3.1.: Number of elements and coefficient of time step

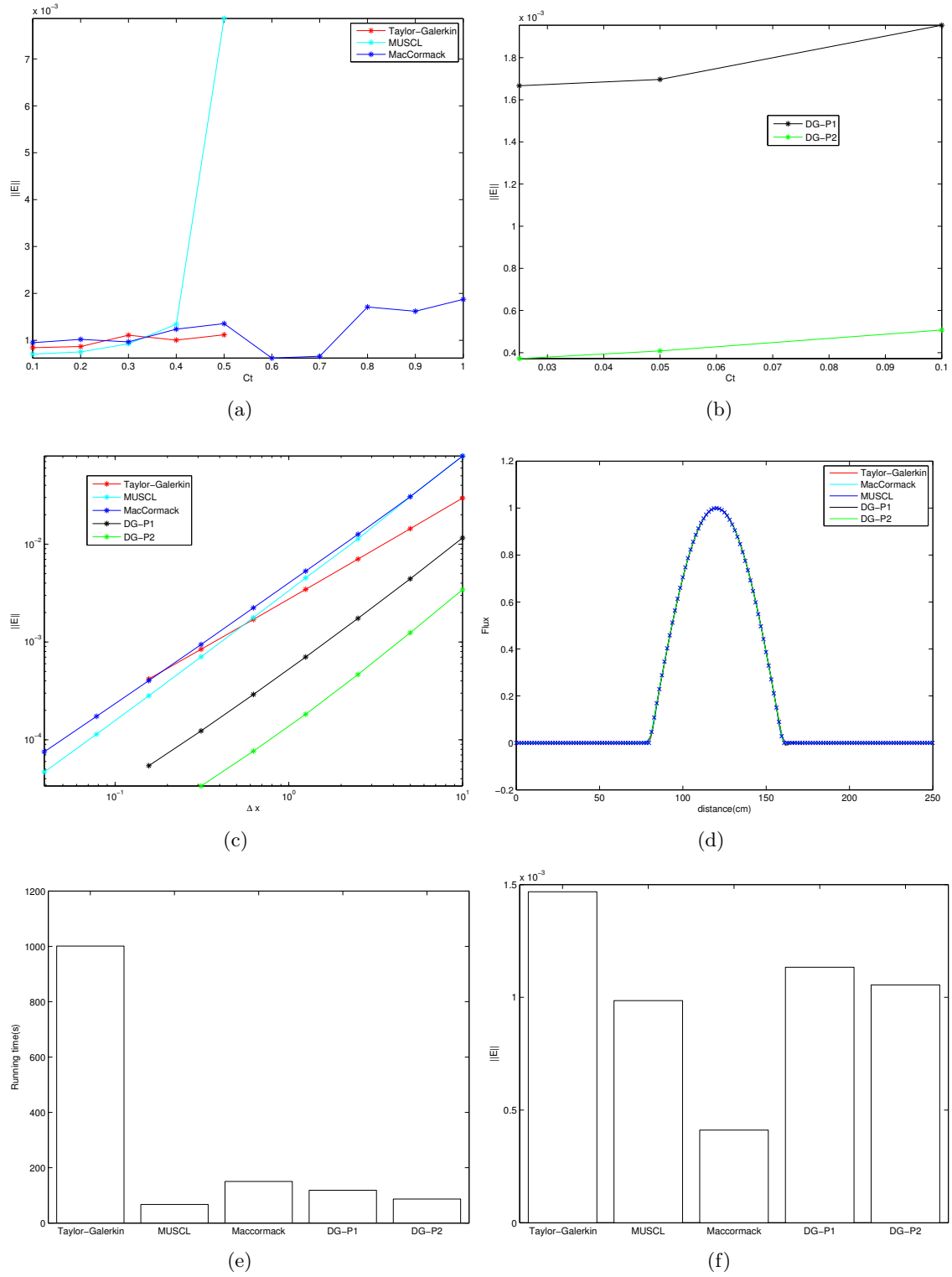

Figure 3.4.: Test on a uniform tube. Top left and right: With a fixed mesh ($N_{TG} = N_{MUSCL} = N_{FD} = 800, N_{DG-\mathcal{P}_1} = N_{DG-\mathcal{P}_2} = 100$), errors as functions of coefficient C_t. Middle left: Errors as functions of the sizes of elements (cells). Middle right: All the numerical solutions for the pulse wave at time 0.4s are overlapped, the analytical solution is indicated by cross signs. Bottom left and right: Running time and error of each scheme for the configuration shown in Table 3.1.

3.3.2. Attenuation due to the viscosity of blood

We now consider the same linearized Eq. (3.19) with the small term due to skin friction ($C_f \neq 0$ and $C_v = 0$). The main dynamics of the system will be grossly the same traveling wave but attenuated by viscosity of blood. This behaviour can be predicted by asymptotic analysis. We have a small non-dimensional parameter $\epsilon_f = T_c C_f / A_0$, which is the ratio of the characteristic time of pulse T_c to the characteristic time of attenuation A_0/C_f. In order to see how the waveform slowly evolves when it propagates to, say right, we make a change of variables to $\tau = \epsilon_f t$ and $\xi = x - c_0 t$ (slow time, moving frame). The two differential operators ∂_t and ∂_x expand as

$$\frac{\partial}{\partial t} = \frac{\partial \tau}{\partial t}\frac{\partial}{\partial \tau} + \frac{\partial \xi}{\partial t}\frac{\partial}{\partial \xi} = \epsilon_f \frac{\partial}{\partial \tau} - c_0 \frac{\partial}{\partial \xi}$$
$$\frac{\partial}{\partial x} = \frac{\partial \xi}{\partial x}\frac{\partial}{\partial \xi} = \frac{\partial}{\partial \xi}.$$

The solution has the asymptotic expansion

$$\tilde{A} = \tilde{A}_0 + \epsilon_f \tilde{A}_1 + ..., \quad \tilde{Q} = \tilde{Q}_0 + \epsilon_f \tilde{Q}_1 + ...$$

Substituting these into the governing equations expressed in new variables and collecting the terms with the same order of ϵ_f, one has

$$(-c_0 \frac{\partial \tilde{A}_0}{\partial \xi} + \frac{\partial \tilde{Q}_0}{\partial \xi}) + \epsilon_f (\frac{\partial \tilde{A}_0}{\partial \tau} - c_0 \frac{\partial \tilde{A}_1}{\partial \xi} + \frac{\partial \tilde{Q}_1}{\partial \xi}) + .. = 0$$
$$(-c_0 \frac{\partial \tilde{Q}_0}{\partial \xi} + c_0^2 \frac{\partial \tilde{A}_0}{\partial \xi}) + \epsilon_f (\frac{\partial \tilde{Q}_0}{\partial \tau} - c_0 \frac{\partial \tilde{Q}_1}{\partial \xi} + c_0^2 \frac{\partial \tilde{A}_1}{\partial \xi} + \frac{\tilde{Q}_0}{T_c}) + .. = 0.$$

We take the first order term in ϵ_f in the first equation, substitute it in the first order term in ϵ_f in the second equation. Then we obtain

$$(\frac{\partial \tilde{Q}_0}{\partial \tau} + c_0 \frac{\partial \tilde{A}_0}{\partial \tau} + \frac{\tilde{Q}_0}{T_c}) = 0.$$

From the terms of the zeroth order in ϵ_f, which involve derivative in ξ only, the solution must have the form $\tilde{Q}_0 = c_0 \tilde{A}_0(\tau, \xi) + \delta(\tau)$. Substituting it into the previous equation generates terms $\frac{\partial \delta}{\partial \tau}$ and $\delta(\tau)$. These are secular terms and thus can be set null. So we have $c_0 \tilde{A}_0 = \tilde{Q}_0$ and $\frac{\partial \tilde{Q}_0}{\partial \tau} = -\frac{1}{2T_c}\tilde{Q}_0$, or

$$\tilde{Q}_0 = \tilde{Q}_0(0, \xi) e^{-\tau/(2T_c)} = \tilde{Q}_0(0, x - c_0 t) e^{-\epsilon_f t/(2T_c)}.$$

For more on asymptotic analysis of blood flow in large blood vessels, we refer to reference [100].

In Figure 3.5, we plot the snapshots of the waveform at time 0.2s, 0.4s, 0.6s and 0.8s. In the computation, the inflow is a half sinusoidal flux as described in the previous subsection and the outflow is nonreflecting. The skin friction coefficient C_f is $40\nu\pi$, and

the parameter $2A_0c_0/C_f$ is about 2000cm. The damping rate of the amplitude of the waveform agrees very well with the analytical prediction, $\exp(-\frac{C_f x}{2A_0c_0})$, which is indicated by the dashed line. Also note that the errors of different schemes are not the same. The MUSCL scheme causes the peak of the wave to slightly flatten, while all of the other schemes are dispersive: we have small oscillations at the foot of the signal.

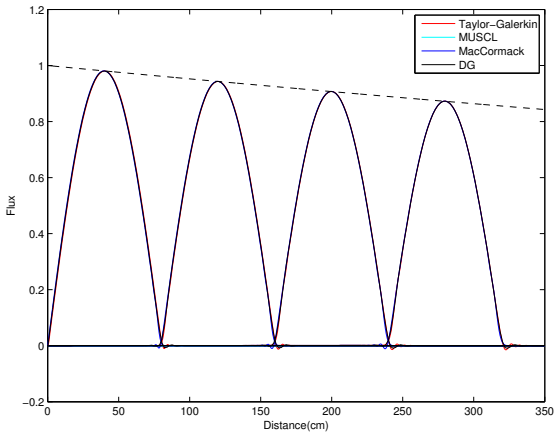

Figure 3.5.: Attenuation due to the skin friction. The snapshots are at time 0.2s, 0.4s, 0.6s and 0.8s. The dashed line is $\exp(-\frac{C_f x}{2A_0c_0})$ with $2A_0c_0/C_f \simeq 2000$cm. The flux is normalized with respect to Q_c.

3.3.3. Diffusion due to the viscosity of the arterial wall

This time we consider the linearized Eqs. (3.19) with the Kelvin-Voigt effect but no viscous fluid effect ($C_f = 0$ and $C_v \neq 0$). The small parameter is now $\epsilon_v = C_v/(c_0^2 T_c)$. If we apply the same technique as described in the previous subsection, we can readily obtain the diffusive behaviour of the pulse wave in the moving frame:

$$\frac{\partial \tilde{Q}_0}{\partial \tau} = \frac{c_0^2 T_c}{2} \frac{\partial^2 \tilde{Q}_0}{\partial^2 \xi}. \tag{3.20}$$

The solution of this equation can be given by the convolution

$$\tilde{Q}_0(\tau, \xi) = \int_{-\infty}^{+\infty} \tilde{Q}_0(0, \xi) G(\tau, \xi - \zeta) d\zeta$$

where G is the fundamental solution of the Eq. (3.20)

$$G(\tau, \xi) = \frac{1}{\sqrt{2\pi\tau c_0^2 T_c}} e^{-\xi^2/(2\tau c_0^2 T_c)}$$

and $\tilde{Q}_0(0, \xi)$ is the initial state. In the test vessel, the parameters are kept the same as in the case of attenuation. The coefficient C_v is $0.6275\text{m}^2/\text{s}$ and $\epsilon_v \simeq 0.1$. This

corresponds to ϕ=5000Pa $\cdot$ s, which is in the range of observed values on animals [4]. To facilitate the calculation of the analytical solution, nonreflecting B.C.s are imposed at the two ends of the vessel and the I.C. is a half sinusoidal waveform for Q (dashed line in Figure 3.6) and a constant value for A_0. It is clear that half of the initial wave propagates to right and at the same time the waveform is spread out due to the diffusive effect. The analytical solution at time 0.4s (indicated by cross signs) agrees well with the corresponding numerical solutions.

Another point worthy noticing is the operator splitting errors. In the DG scheme, no operator splitting error is induced. All of the other numerical schemes adopt operator splitting method. They produce very accurate solutions as well as DG. Thus it verifies the *a priori* judgement that Godunov splitting is sufficient.

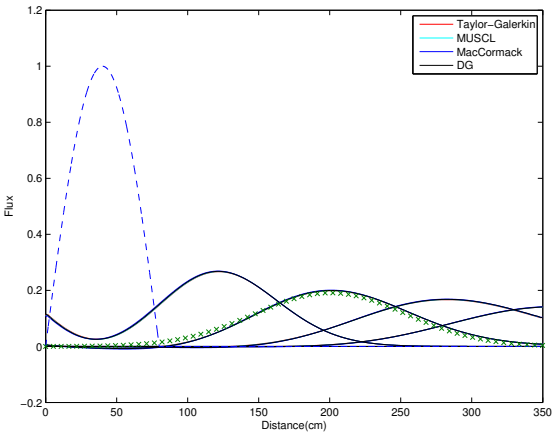

Figure 3.6.: Diffusion due to the viscosity of the wall. The dashed line is the initial condition. One half of the original waveform propagates to right. The snapshots are at time 0.2s, 0.4s, 0.6s and 0.8s. The analytical prediction from the convolution at time 0.4s is indicated by cross signs. The difference between the different numerical solutions is not discernible. The flux is normalized with respect to Q_c.

3.3.4. Shock-like phenomena due to the nonlinearity

We now consider the full nonlinear system, but without any source terms ($C_f = 0$ and $C_v = 0$). The small parameter is now $\epsilon_2 = Q_c/(c_0 A_0)$. If we apply the same technique as described in the previous subsection, we can readily obtain an equation for the nonlinear behaviour of the pulse wave in the moving frame (inviscid Burgers' equation):

$$\frac{\partial \tilde{Q}_0}{\partial \tau} = \frac{1}{2A_0}\tilde{Q}_0 \frac{\partial \tilde{Q}_0}{\partial \xi}$$

One important consequence of nonlinear hyperbolic system is that shocks may arise even if the initial condition is very smooth. In normal physiological conditions, shocks are

not observed in arterial systems. But in venous system, shock-like phenomena may occur on muscular veins during walking and running. The intramuscular pressure (equivalent to P_{ext} in our model) can rise to $20-40$ kPa in a few milliseconds [6]. In such situation, experiments and numerical simulations [24, 47] have shown this critical behaviour. For some large mammals, for instance giraffes, even in static postures, the gravity-driven flow in a long inclined vein may develop into shock-like waves, like the roll waves in a shallow-water channel [12, 13]. For another example, the traumatic rupture of the aorta is responsible for a significant percentage of traffic death and the rupture may be well accounted for by the shock-like transition resulted from the blunt impact to the thorax [36]. For possible applications in these situations, we test all the schemes with a shock-like wave.

To generate a shock, we impose a step jump signal of flux at the inlet. For a vessel of 1 meter, the numbers of elements for Taylor-Galerkin, MacCormack and MUSCL schemes are 100, 200 and 800 respectively. The DG scheme uses 25 elements and the order of polynomial is 2. Figure 3.7 shows that the MUSCL scheme with a flux limiter captures the shock without nonphysical oscillations, whereas the other numerical schemes cause spurious oscillations. This verifies the total-variation-diminishing (TVD) property of the MUSCL scheme. But the MUSCL is very diffusive at the shock, thus a very fine mesh is required. For the DG scheme, limiters may be introduced as well to eliminate the oscillations [31]. This remedy will be necessary for DG to be applicable on problems with shocks. On Figure 3.7(b) we plot a case with some viscosity of the wall. The added moderate physical diffusive term smoothens the wave and all the schemes give almost the same result.

3.3.5. Reflection and transmission at a branching point

Up to now, we focused on the various behaviours of wave within a single vessel: propagation, attenuation, diffusion, etc. Now, we look at the boundaries of each artery. Indeed, pressure waves are reflected and transmitted at the conjunction points of a network. For a linearized system, given the impedance $Z = \frac{\rho c_0}{A_0}$, the reflection and transmission coefficients at a branching point can be calculated by the formula,

$$\mathcal{R} = \frac{Z_p^{-1} - (Z_{d_1}^{-1} + Z_{d_2}^{-1})}{Z_p^{-1} + (Z_{d_1}^{-1} + Z_{d_2}^{-1})}, \quad \mathcal{T} = \frac{2Z_p^{-1}}{Z_p^{-1} + (Z_{d_1}^{-1} + Z_{d_2}^{-1})}, \tag{3.21}$$

where Z_p and Z_d are the characteristic impedance of the parent and daughter vessels [29, 59]. In Figure 3.8, for sake of illustration, the configuration of the branching and the time profiles of pressure at two locations are shown. The amplitude is normalized with respect to $Q_c = 1\times10^{-6}\mathrm{m}^3/\mathrm{s} = 1\mathrm{ml/s}$. For the parent vessel: $\beta = 2.3633\times10^6\mathrm{Pa/m}$, $A_0 = 4\mathrm{cm}^2$ and for each of the daughter vessels: $\beta = 6.3021\times10^6\mathrm{Pa/m}$, $A_0 = 1.5\mathrm{cm}^2$. The B.C.s at the outlets of the daughter vessels are nonreflecting. Thus the reflected pulse wave is generated at the conjunction point. According to the formula (3.21), $\mathcal{R} = 0.2603$ and $\mathcal{T} = 1.2603$. The pressure profiles at the points A and B agree very well with the analytical predictions. All of the numerical schemes are compatible with this treatment

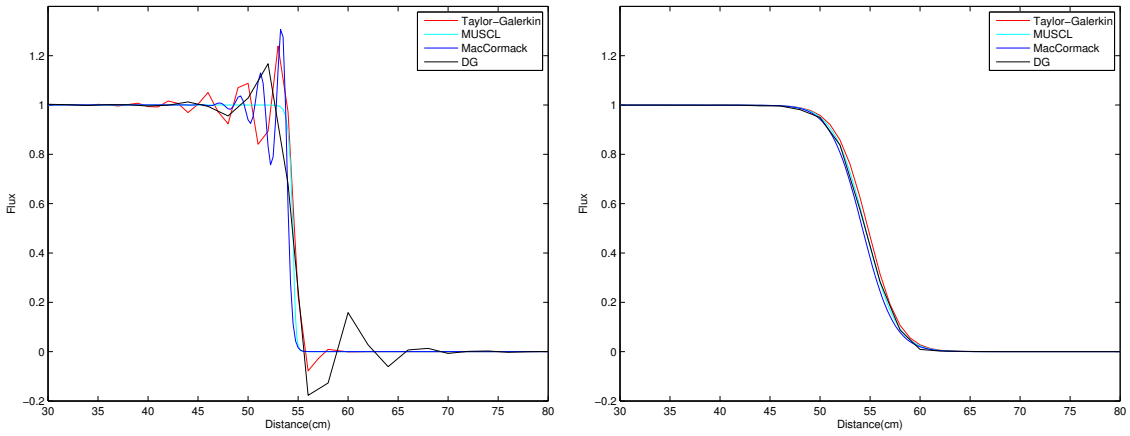

(a) (b)

Figure 3.7.: A shock in the system. A step jump signal of flux is imposed at the inlet and a snapshot is shown. The left figure (a) shows that the MUSCL scheme with a flux limiter captures the shock without nonphysical oscillations, whereas the other numerical schemes cause spurious oscillations. The right figure (b) shows that all the schemes give almost the same result for a system with a moderate physical diffusive term.

of conjunction point. Note that in healthy arterial system, the related arteries of most conjunctions are well matched such that there are essentially no reflections ($\mathcal{R}$=0) at the conjunctions [91, 57]. The purpose of the proposed configuration is just to test the numerical schemes.

3.3.6. Application on a full systematic arterial network

As already mentioned in the introduction, a relatively realistic description of arterial system has been done in 1D simulations, with different numerical solvers by different teams. For example, in [51, 71], Galerkin approach is used. In these papers, wall viscosity is not included. Note that [64] gives a survey of literature on the details the model, and adopted a viscoelastic model of the wall. But, in all of those papers, usually only one numerical scheme is adopted and cross comparisons among them are not available. In this subsection, we compute a network of 55 arteries with the viscoelastic model presented above and make a cross comparison among the numerical schemes. To this end, the topology and properties value of the arterial network are adapted from [71]. But the viscosity coefficient of the Kelvin-Voigt model on human body is not given in this paper. In reference [4], the viscosity of aortic wall of dogs was modeled by a Kelvin-Voigt model and it shows that the value of ϕ is in the range of $3.8 \pm 1.3 \times 10^3 \mathrm{Pa} \cdot \mathrm{s}$ to $7.8 \pm 1.1 \times 10^3 \mathrm{Pa} \cdot \mathrm{s}$. Hence, we assume $\phi = 5 \times 10^3 \mathrm{Pa} \cdot \mathrm{s}$ to calculate the coefficient C_v. The final parameters of the network we used are shown in Table 3.3. We note that there may be differences between arteries in human and dog and the arteries in different

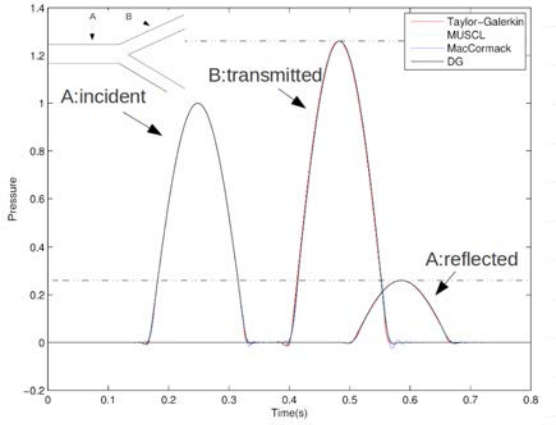

Figure 3.8.: Reflection and transmission of pressure wave at a branching point. The time profiles of pressure at points A and B are plotted. The analytical reflection and transmission coefficients are 0.2603 and 1.2603 (indicated by the dashed line).

locations may cause a considerable variation. Nevertheless the inclusion of viscosity term makes it possible to test the numerical schemes in a more realistic condition.

The peak value of the input flux Q_c is 500 ml/s. This value is very close to the peak flow rate at the root of aortic artery [64]. We choose $\min_{i=1}^{i=55}(L^i/c_0^i)$ as a reference length, with L^i the vessel length and c_0^i the linearized wave speed of the i-th artery. For a coarsest possible mesh, the number of elements (cells) of the i-th artery is $N_{base}^i = \lfloor \frac{L^i/c_0^i}{\min_{i=1}^{i=55}(L^i/c_0^i)} \rfloor$, where $\lfloor \cdot \rfloor$ is the floor function. We computed the relative change of solutions when the number of the elements (cells) is doubled. Figure 3.9 shows the relative change of the solutions when the number of the elements (cells) is changed from $2N_{base}$ to $4N_{base}$. The relative change of a quantity (for example flux Q) with two meshes N_1 and N_2 is defined as $||\mathbf{Q}_{N_1} - \mathbf{Q}_{N_2}||_{rms}/(Q_{max} - Q_{min})$, where $||\cdot||_{rms}$ is the root-mean-square error as before, Q_{max} and Q_{min} are the maximum and minimum values within one heart beat. Figure 3.9 shows that the changes of flux and pressure are less than 1.5% for all of of the schemes except DG. Thus we plotted in Figure 3.10 the results computed with mesh $2N_{base}$. The DG scheme is not tested in this manner because it is already converged: results in Figure 3.10 show that there is no discernible difference between the DG solutions with the others even with the coarsest possible mesh. In this computation, the order of polynomial of DG is 1, thus the total number of free degrees is $2N_{base}$, which is equal to those of the other schemes. Time step is prescribed by $\Delta t = C_t \min_{i=1}^{i=55}(\frac{L^i}{N^i c_0^i})$. The coefficient C_t and the corresponding real time steps in the computation are shown in Table 3.2.

In Figure 3.10 we plot the history profiles of flux and pressure at the middle of four representative arteries. All of the numerical solutions agree very well. The main features of the pressure and flux profiles reported in literature [64, 71] are observed. The peak

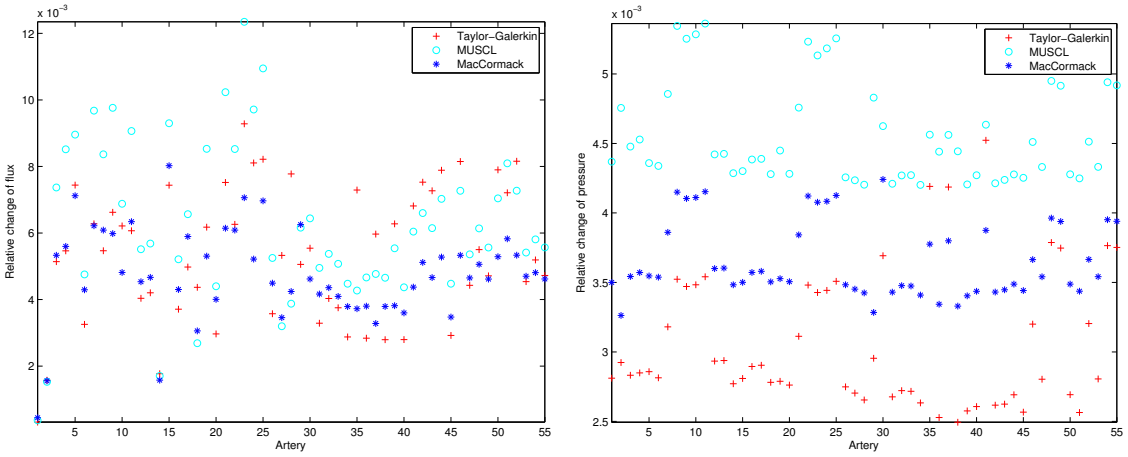

(a) (b)

Figure 3.9.: Relative changes of the solutions when the mesh is doubled from $2N_{base}$ to $4N_{base}$. The left figure shows that the relative changes of all the fluxes are less than 1.3 %. The right figure shows that the relative changes of all the pressures are less then 0.6% .

scheme	C_t	Δt (10^{-6}s)	running time (min)
Taylor-Galerkin	0.4	222	22.0
MUSCL	0.25	139	31.9
MacCormack	0.1	55.5	91.2
Local DG	0.006	6.66	576

Table 3.2.: Time steps and running time for one heart beat using one processor on a standard Linux work station with MATLAB.

value of pressure waveform increases as we travel down the system. We can also see the dicrotic notch at artery 1. At artery 37, a reverse flow is observed (see Figure 3.10(f)), which agrees with clinical measurement [64].

Both *in vivo* [32, 64] and *in vitro* [2] studies show that the models with viscoelasticity predict the pulse waves better. This effect is most pronounced at the peripheral sites [2, 70]. The predictions by the elastic and viscoelastic models are compared at two locations, see Figure 3.11. We can clearly see the smoothening effect on the pulse curves at both sites. The biggest relative difference is observed on the flow rate curve at the peripheral site (see Figure 3.11(c)). This study confirms again the necessity to consider the viscoelasticity in the 1D model.

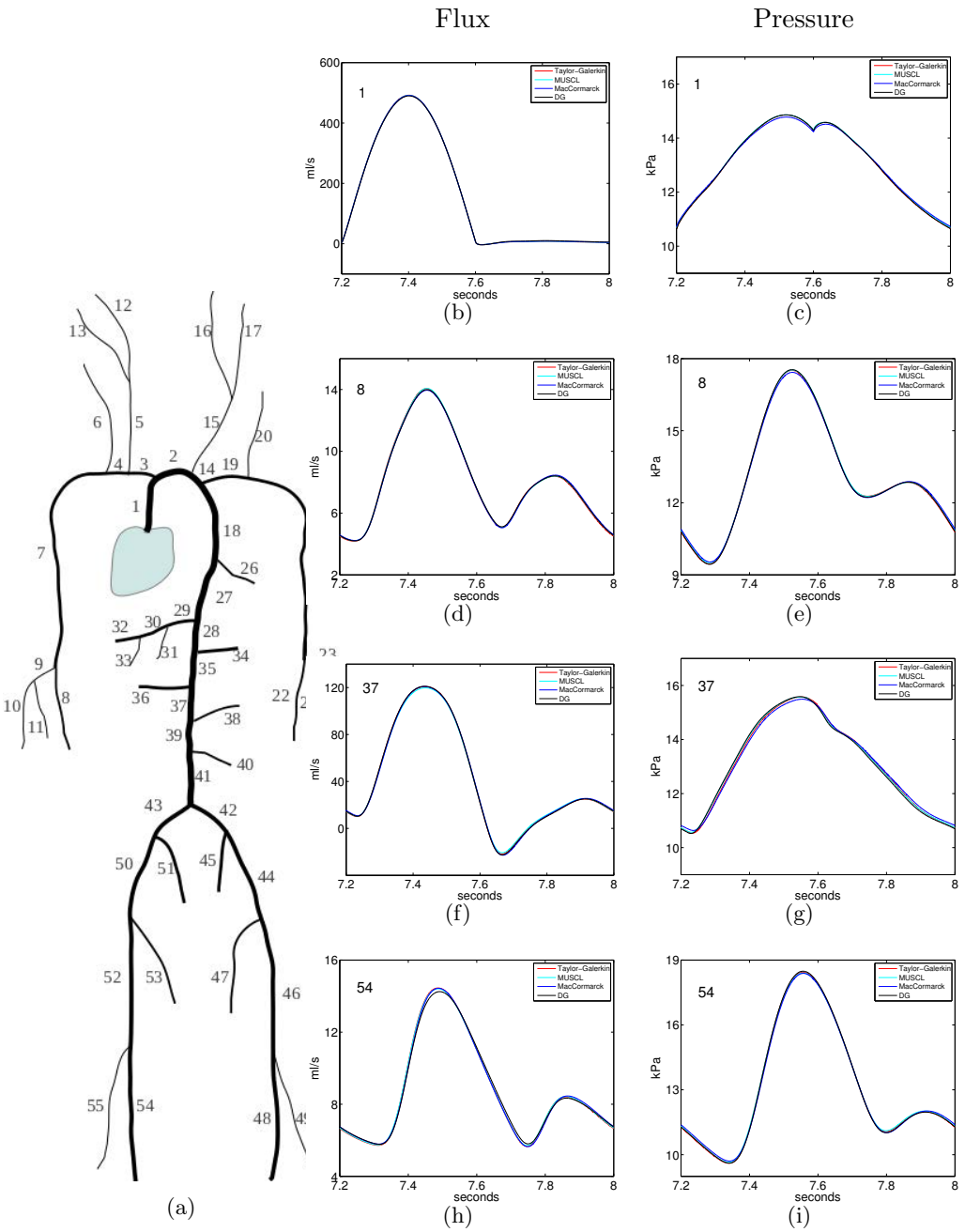

Figure 3.10.: The history profiles of flux and pressure at four locations. Ten heart beats are computed to secure that steady state is achieved, but only the tenth heart beat is plotted. The differences between the four numerical schemes are very small. See Table 3.3 for time steps and running time of each scheme.

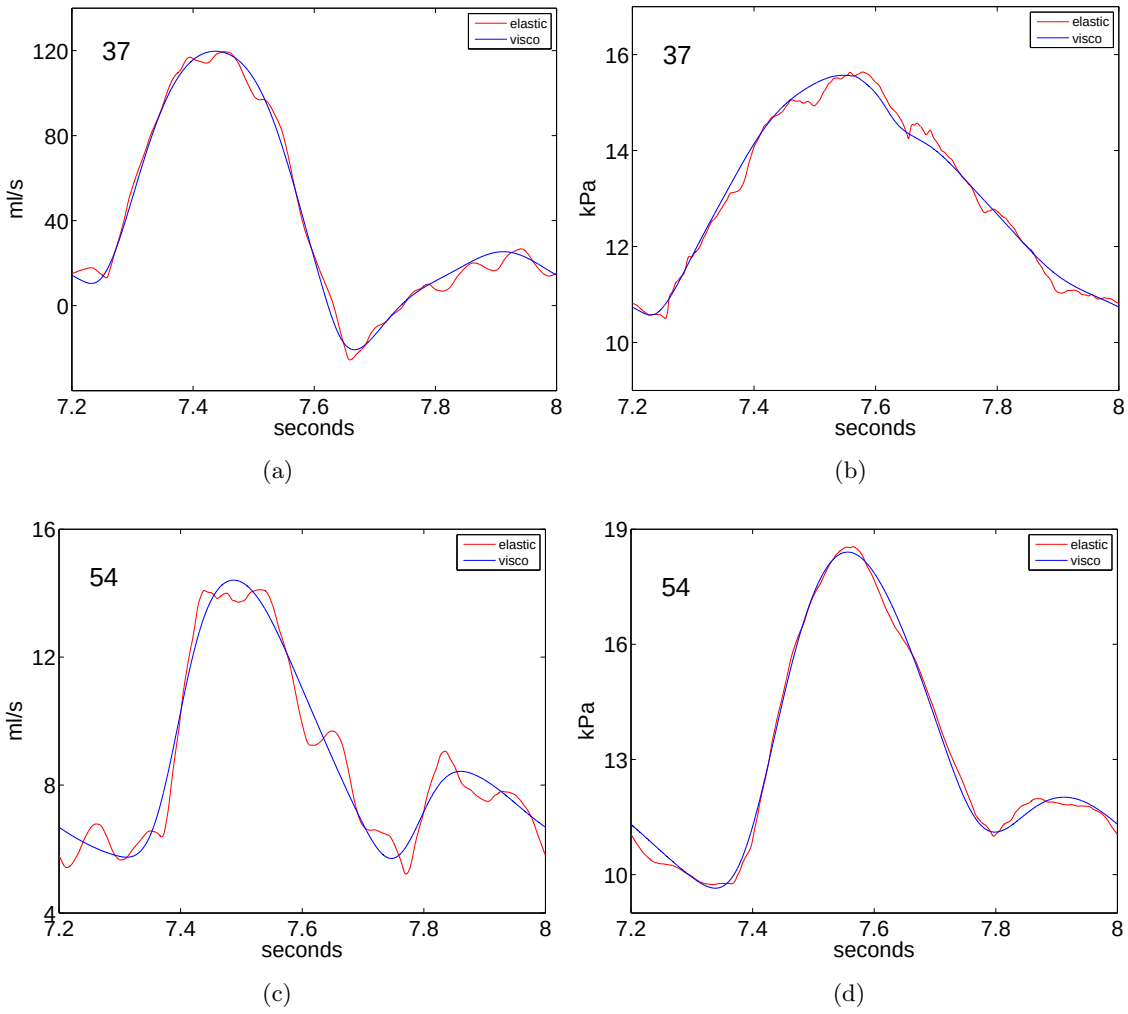

Figure 3.11.: The comparison between elastic and viscoelastic models (MUSCL scheme). The viscoelasticity damps the oscillations of high frequency.

3.4. Conclusion

In this chapter, we solved the hyperbolic-parabolic system with four numerical schemes: MacCormack, Taylor-Galerkin, MUSCL and local discontinuous Galerkin. The implementations were verified with analytical, semi-analytical or clinical observations in many cases. At first, a single uniform tube was considered. Under the assumption of small nonlinearities, we obtained asymptotic solutions of the linearized system with different source terms. The propagation, attenuation and diffusion of the waveform were illustrated by both the numerical and analytical solutions. Moreover, in case of a larger nonlinearity, the shock capturing property of each scheme was tested. After the test on a single vessel, a simple bifurcation was computed to check the numerical coupling of different arteries. Finally, we computed a relatively realistic network with 55 arteries. The check of the numerical solutions in all cases was very favorable for all of the schemes. We can compare the schemes in four aspects: accuracy, shock-capturing property, computational speed and implementation complexity.

1. MacCormack and Taylor-Galerkin schemes generate small oscillations. MUSCL scheme has slight arbitrary steepening effect. Both diffusion and dispersion errors are very small for DG. Nevertheless all of the schemes converge with a moderate fine mesh and precisely capture the various phenomena of this hyperbolicity-dominated hyperbolic-parabolic system.

2. MacCormack, Taylor-Galerkin and DG generate spurious oscillations when the solution is near a shock. Numerical flux limiters are possible to filter out the oscillations. That will further complicate the schemes and both the theory and technique are still under research [37, 47]. On the other hand, there are very mature techniques to impose a slope limiter in the FV scheme. Shock capturing property is unique for MUSCL among the four schemes presented in this paper. But it is very diffusive at a shock, thus a very fine mesh is necessary when a shock may appear.

3. For a network of human size, the speed of computation can be ordered from fast to slow as: Taylor-Galerkin, MUSCL, MacCormack and local DG. The temporal integration in the Taylor-Galerkin scheme is more efficient than Adams-Bashforth 2-step method. Thus it allows a larger time step with a comparable accuracy. But if the number of elements for one artery is too large (larger than 500), Taylor-Galerkin becomes slower because the sizes of the global matrices increase quadratically and thus the storing and inverting of matrices become very expensive. The DG scheme prevents the application of Crank-Nicolson method on the diffusive term. An explicit method called local DG scheme was adopted in this paper. Even with a moderate diffusion coefficient (within the range observed in physiological condition), a very small time step is necessary for stability. To compute one heart beat, the local DG takes about 9 hours while all other schemes take only 20-90 minutes (using one processor on a standard Linux workstation with Matlab).

4. From easiest to hardest, the implementation of the schemes can be ordered: MacCormack, MUSCL, Taylor-Galerkin and local DG.

As a final conclusion from the point of view of practical application, we recommend MacCormack in case of small nonlinearities as it is very simple and robust. MUSCL will be a very good option if there may be shock-like phenomena in the system. Taylor-Galerkin has quite balanced properties between speed and accuracy if no shock-like phenomena may present in the system. Local DG is suitable for systems with very small physical diffusive terms since both the numerical diffusion and dispersion are very small in this scheme.

Table 3.3.: Arterial network

ID	Name	l (cm)	A_0 (cm^2)	β (10^6Pa/cm)	C_v ($10^4 cm^2$/s)	R_t
1	Ascending aorta	4.0	6.789	0.023	0.352	–
2	Aortic arch I	2.0	5.011	0.024	0.317	–
3	Brachiocephalic	3.4	1.535	0.049	0.363	–
4	R.subclavian I	3.4	0.919	0.069	0.393	–
5	R.carotid	17.7	0.703	0.085	0.423	–
6	R.vertebral	14.8	0.181	0.470	0.595	0.906
7	R. subclavian II	42.2	0.833	0.076	0.413	–
8	R.radius	23.5	0.423	0.192	0.372	0.82
9	R.ulnar I	6.7	0.648	0.134	0.322	–
10	R.interosseous	7.9	0.118	0.895	0.458	0.956
11	R.ulnar II	17.1	0.589	0.148	0.337	0.893
12	R.int.carotid	17.6	0.458	0.186	0.374	0.784
13	R. ext. carotid	17.7	0.458	0.173	0.349	0.79
14	Aortic arch II	3.9	4.486	0.024	0.306	–
15	L. carotid	20.8	0.536	0.111	0.484	–
16	L. int. carotid	17.6	0.350	0.243	0.428	0.784
17	L. ext. carotid	17.7	0.350	0.227	0.399	0.791
18	Thoracic aorta I	5.2	3.941	0.026	0.312	–
19	L. subclavian I	3.4	0.706	0.088	0.442	–
20	L. vertebral	14.8	0.129	0.657	0.704	0.906
21	L. subclavian II	42.2	0.650	0.097	0.467	–
22	L. radius	23.5	0.330	0.247	0.421	0.821
23	L. ulnar I	6.7	0.505	0.172	0.364	–
24	L. interosseous	7.9	0.093	1.139	0.517	0.956
25	L. ulnar II	17.1	0.461	0.189	0.381	0.893
26	Intercostals	8.0	0.316	0.147	0.491	0.627
27	Thoracic aorta II	10.4	3.604	0.026	0.296	–
28	Abdominal aorta I	5.3	2.659	0.032	0.311	–
29	Celiac I	2.0	1.086	0.056	0.346	–
30	Celiac II	1.0	0.126	0.481	1.016	–
31	Hepatic	6.6	0.659	0.070	0.340	0.925
32	Gastric	7.1	0.442	0.096	0.381	0.921
33	Splenic	6.3	0.468	0.109	0.444	0.93
34	Sup. mesenteric	5.9	0.782	0.083	0.439	0.934
35	Abdominal aorta II	1.0	2.233	0.034	0.301	–
36	L. renal	3.2	0.385	0.130	0.481	0.861
37	Abdominal aorta III	1.0	1.981	0.038	0.320	–
38	R. renal	3.2	0.385	0.130	0.481	0.861
39	Abdominal aorta IV	10.6	1.389	0.051	0.358	–
40	Inf. mesenteric	5.0	0.118	0.344	0.704	0.918
41	Abdominal aorta V	1.0	1.251	0.049	0.327	–
42	R. com. iliac	5.9	0.694	0.082	0.405	–
43	L. com. iliac	5.8	0.694	0.082	0.405	–
44	L. ext. iliac	14.4	0.730	0.137	0.349	–
45	L. int. iliac	5.0	0.285	0.531	0.422	0.925
46	L. femoral	44.3	0.409	0.231	0.440	–
47	L. deep femoral	12.6	0.398	0.223	0.419	0.885
48	L. post. tibial	32.1	0.444	0.383	0.380	0.724
49	L. ant. tibial	34.3	0.123	1.197	0.625	0.716
50	R. ext. iliac	14.5	0.730	0.137	0.349	–
51	R. int. iliac	5.0	0.285	0.531	0.422	0.925
52	R. femoral	44.4	0.409	0.231	0.440	–
53	R. deep femoral	12.7	0.398	0.223	0.419	0.888
54	R. post. tibial	32.2	0.442	0.385	0.381	0.724
55	R. ant. tibial	34.4	0.142	1.210	0.628	0.716

Data adapted from [71] and [4].

4. Development of a parallel code

4.1. Introduction

Patient-specific modeling of blood flow in vascular networks is a very changing task. There are billions of vessels in the systemic arterial network alone, and they vary largely in scale. The diameter of vessels ranges from 30 mm (aorta) to 5×10^{-3} mm (capillary), and the Womersley number ranges from 20 to 10^{-3}. The main features of blood flow in various locations can be drastically different. For instance, in the large and medium-sized vessels, the blood flow is convection-dominated and significantly pulsatile; in the arteriole and capillary bed, the blood flow is dominated by fluid viscosity and pulsates slightly in time. Models with various complexity from 3-dimensional to 0-dimensional have been proposed and the coupling between them is also a hot research topic (multi-scale modeling). Among those models, the 1D model plays a very special role due to its balance between modeling complexity and computing cost.

Currently, simulation of a network with about 50 segments for one cardiac cycle can be done in a few minutes [2, 16, 48]. Keeping this in mind, we want to develop a code which will have the following features:

1. *Fast.* Besides the mathematical model, accuracy of a patient-specific simulation also heavily relies on properly-set parameters. However, most of those parameters cannot be measured invasively and accurately, such as inflow rate, viscoelasticity, downstream impedance, etc. The uncertainties of the parameters propagate to the output of the model, and this process can be evaluated by sensitive analysis [16, 39]. In the reverse direction, the parameters of the model may be estimated by techniques of data assimilation where the differences between the output of the model and observations are minimized to obtain best estimations [44]. In all those cases, the simulations have to be run a lot of times, which necessitates a fast code.

2. *Easy to be set for large networks.* If we only consider the part of the network where a 1D model is applicable, the number of vessel segments is well beyond our simulation capacity. Usually the network of the 1D model is truncated at certain levels and a simplified model is designed to mimic the downstream sub-networks. This simplified model may be a tapered long tube [51], a structured network of linearized 1D models [56] or a 0D model [88]. This is usually a good compromise between economy and efficacy. However, in many cases, the distributed 1D model cannot be replaced by lumped models. For instance, to simulate some special circulations (e.g. coronary, renal and cerebral circulations), we usually must include a larger number of vessels in the 1D model to obtain detailed information on the

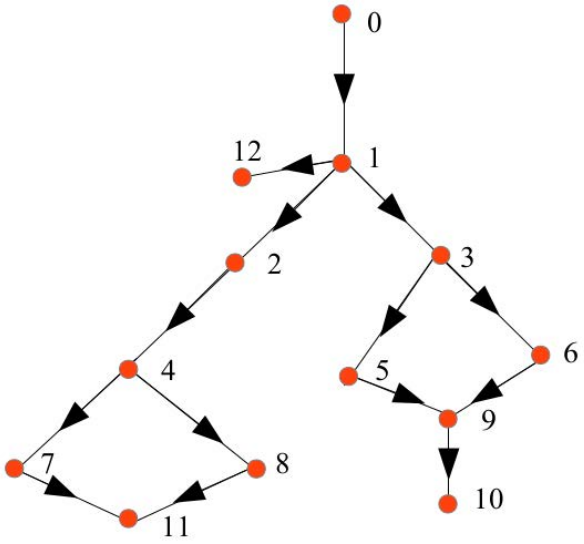

Figure 4.1.: A network described by Directed Acyclic Graph (DAG). Nodes represent conjunctions, directed edges represent vessels.

distribution of blood flow. Thus, our code should be easily scaled to such large networks.

3. *User friendly.* The configurations of a simulation, such as network topology, vessel properties and boundary conditions, should be easy to set. The whole workflow of a simulation, including pre-processing, computing and post-processing, should can be done with free open source software.

4.2. Development of the code

4.2.1. Design

The geometry of a network is described by a Directed Acyclic Graph (DAG), as shown in Fig. 4.1. In the DAG, the nodes represent the vessel conjunctions and the directed edges stand for blood vessels. Various kinds of conjunctions can be defined in a DAG. In Fig. 4.1, we show several kinds: one parent vessel connected with one daughter vessel (node 2), one parent vessel branching into two (nodes 3, 4) or three (node 1) daughter vessels, and two vessels converge with (node 9) or without (node 11) a third downstream vessel etc. But there are no closed loops in a DAG. That is to say, if one starts from any one node and follows the direction of each edge, he cannot come back to the starting node through a circle path. We can use DAG to describe both arterial and venous networks.

A DAG can be easily represented by a comma separated value (CSV) file, whose first column writes the starting node of a directed edge and the second column the ending node. The row numbers of the records are mapped one-to-one to the numbers

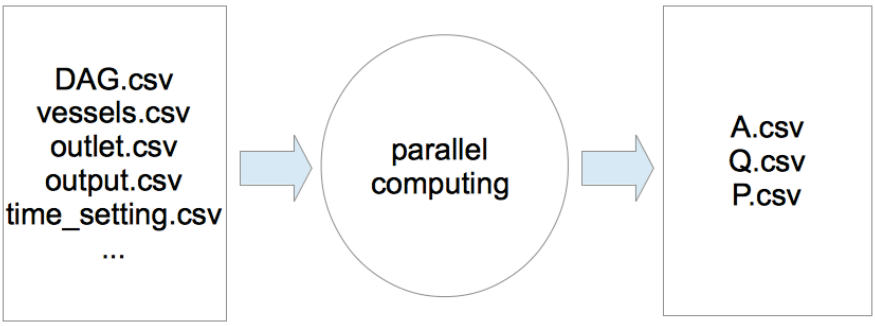

Figure 4.2.: Input/Output of the code. DAG.csv specifies topology of the network; vessels.csv specifies physical parameters, meshes etc.; outlet.csv is for outlet boundary conditions, output.csv specifies the locations of interests to be recorded; time_setting.csv is for the time control of computing and recording.

of the arteries. The properties of each vessel are also set through CSV files, such as the viscoelasticity, the mesh, the reference cross sectional area etc. In the same way, we specify the size of discretized time step, the location and time intervals to keep records of the evolutionary history of the system, etc. As shown by Fig. 4.2, the C++ code reads those files, makes computations and writes the results to specified destinations for further processing. The computing is done in parallel to improve speed if there are multi-segments in the network. For convenience, the parameter files can be prepared by a scripting language. In appendix A, using a circle of arteries as a computing case, we show more details of the structure of CSV files. We also briefly talk about how to prepare the parameter files with Python scripts; how to track errors of parameter files; and how to make animations of the computing result with Gnuplot as the plotting engine. In fact, the whole workflow of a simulation, including computing and data analysis, can be done conveniently only with free open source softwares.

4.2.2. Implementation of parallel C++ code

We take an object-oriented approach to develop the C++ code. In the code, there are two main classes of objects: **artery** and **conjunction**. The **artery** class has a virtual method called **stepMarch**. This method is implemented in the subclasses with different numerical schemes for the 1D governing equations. We implemented MacCormack and MUSCL for **stepMarch** in two subclasses: **artery_FV** and **artery_FD** (see Fig. 4.3). Besides this method, the base **artery** class contains arrays for A, Q, P and some methods to manage the arrays. Fig. 4.4 illustrates the data structure of an object of **network**, which has two vectors of pointers: one contains pointers to the arteries, and another one is used for the conjunctions. The local connectivity information is stored in the **conjunction** by two vectors of pointers which point to the parent and daughter arteries respectively. The **conjunction** also has a method **stepMarch** (notice it is not the same method in the arteries) which solves the domain decomposition problem.

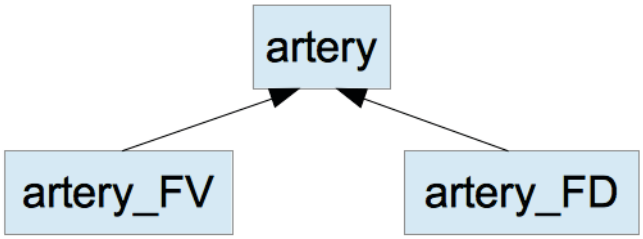

Figure 4.3.: Illustration of the hierarchy of artery. The class **artery** defines a virtual method **stepMarch**, which is implemented in the subclasses **artery_FV** and **artery_FD** with different numerical schemes.

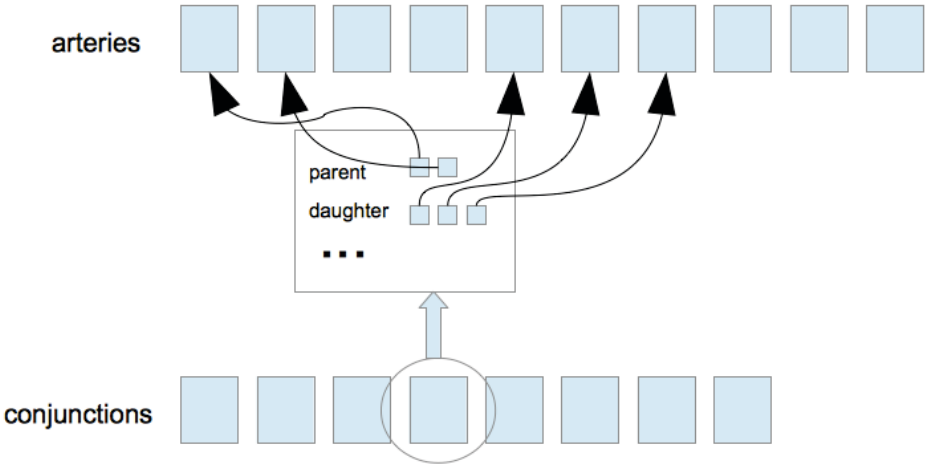

Figure 4.4.: Illustration of data structure of a network. Each conjunction contains one vector of artery pointers to parent vessels and another one to daughter vessels.

At the interior of each artery, the state evolves independently and there are only interactions between connected arteries in the conjunctions. Thus this problem is very suitable for parallelization. We take an coarse-grain strategy to parallelize the computing with OpenMP. Listing 4.1 shows one simplified segment of the code. From line 3 to 16, the whole computational domain is divided evenly among different threads. From line 19 to 26, the conjunctions are iterated to update boundary conditions of each artery. If the conjunction does not have any parent arteries, the method **isRoot** returns **true** and we impose an inflow boundary condition. Similarly, if the conjunction only has parent arteries, the method **isLeaf** returns **true** and outflow boundary conditions are imposed (specified by reflection coefficients). If both the two checks fail, the conjunction must locate in the interior of the DAG graph and **stepMarch** is called to solve the system of coupled equations. In line 27, there is an barrier to synchronize all the conjunctions. When all the new boundary values of the arteries have been imposed, the next **for** loop starts to update the interior values within each artery. The recordings of quantities designated by the user are also done in parallel manner. They are not shown here for the reason of space. By this coarse-grain parallelization, the overhead for spawning threads are minimized. Its performance is better in general than fine-grained parallel code.

4.3. Test with cases

4.3.1. A circle of arteries

There are a lot of native anastomoses in both arterial and venous networks, e.g., the Willis circle, joint anastomoses and dorsal venous arches. A lot of surgery imposed anastomosis also usually make circles of large blood vessels. For instance, in clinical practice, fistulas are created by connecting an artery with a vein to facilitate hemodialysis. Fig. 4.5 shows a series of snapshots of a pressure wave traveling through a circle of arteries. At the inlet of artery 1 we imposed a half sinusoidal wave with a small amplitude (Fig. 4.5(a)). The wave travels down and a small part of it is reflected back after encountering the branching point (Fig. 4.5(c)–Fig. 4.5(e)). With the formula of reflection coefficient at a conjunction point for a linearized system, the calculated amplitude of the reflected wave in this case is 0.086. In Fig. 4.6, the history profiles of pressure at the middle of three arteries (indicated in Fig. 4.5(a)) are shown. All pressures are normalized with the amplitude of the injected wave. The second peak of the blue dashed line in Fig. 4.6 shows the reflected wave. The amplitude meets the analytical value which is indicated by a horizontal line. Two waves are also transmitted into the daughter arteries. Since the two arteries in the upside and downside half circles are the same, the two waves are symmetric and they arrive at the convergence point at the same time. Again, predicted with a linearized system, the amplitudes of the waves at artery 2 and artery 3 should be 1.09 and 0.91. As shown by Fig. 4.6, those waves also meet the the analytical predictions. Through this computation case and other verification techniques described in [93], we gained confidence on the code and applied it to more complicated networks.

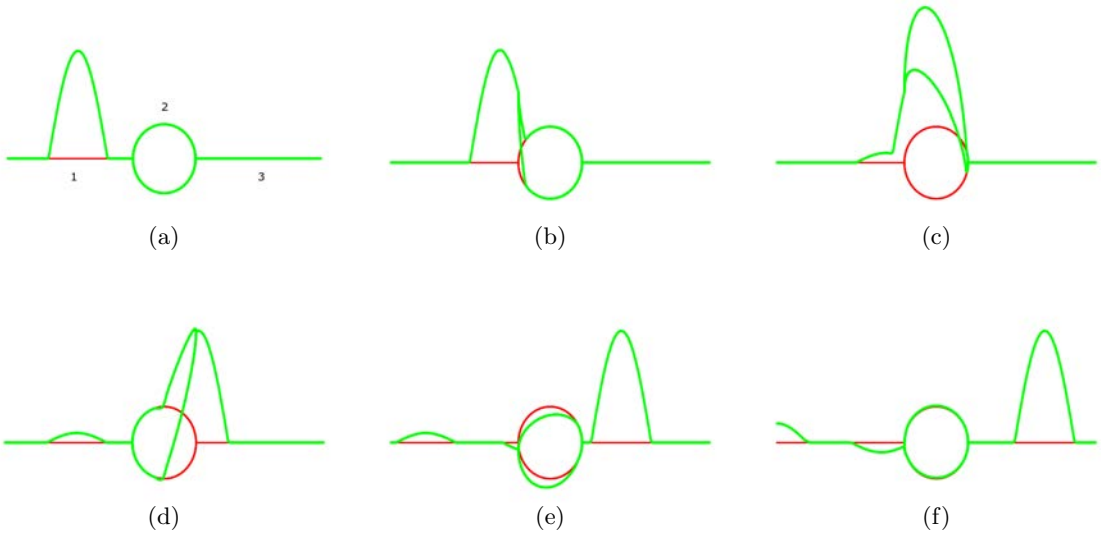

Figure 4.5.: One pulse wave propagating through a circle of arteries. The reflection and transmission at the branching and converging points are clear.

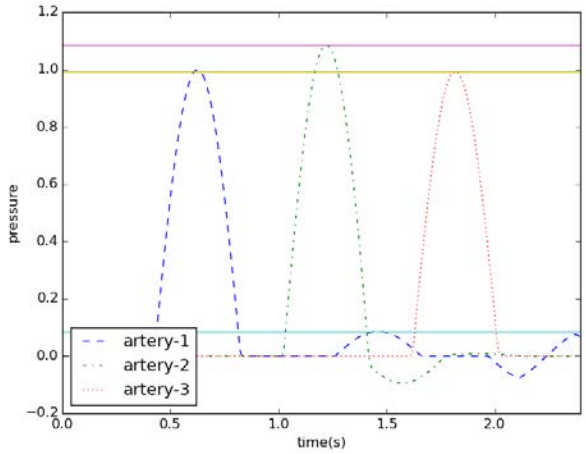

Figure 4.6.: History profiles at the middle of three arteries of the network with a circle (see Fig. 4.5(a) for the locations). The reflection and transmission coefficients meet analytical prediction. See Fig. 4.5 for a series of snapshots of the wave.

4.3.2. A network of human systemic arterial tree

A systemic arterial network with 55 main arteries has been computed in literature. We adapted the parameters of the arteries from paper [91]. Fig. 4.7 shows a series of snapshots of pressure distribution map of the systemic network. The top subfigure in each distribution map shows the heart function and the moment of the snapshot is indicated by the vertical line. The heart function is a curve of flow rate with a period of 0.8 s (heart rate is 70 beats per minute). The systole stage is a half sinusoidal wave with a period of 0.4 s. One stroke volume is 120 ml, thus the peak value of flow rate at the root of aorta is about 471 ml/s. The subfigure in the middle shows the pressure at abdominal aorta. After the peak, the pressure is damped approximately with an exponential rate, which meets clinical observations. The systole pressure at the aorta is about 110 mmHg, and the diastole pressure is about 75 mmHg. This model mimics a health adult. From series of the snapshots, we can recognize the propagation pattern of a pressure wave in the systemic arterial network. We notice that the peak pressure at the limbs are higher than at the aorta as shown by Fig. 4.7(e)–4.7(g). This may be explained by the blood leaks to small side branches which are not considered in this network. This simulation shows that it is possible to use this code to study more complex scenarios.

4.3.3. A kidney network of a mouse

The kidneys take up about 25% of the total cardiac output. That is because the kidneys are the natural filters of the blood to maintain a constant internal chemical environment. Besides the best-known function of removing metabolic waste products, they also serve in many other activities of the body, e.g. regulation of blood pressure; production of hormones. To facilitate the high blood perfusion, the renal impedance is low. Thus a large part of the pulsations in the aorta are propagated into the renal networks. As a consequence, the kidneys are very vulnerable to the stiffening of the systemic arteries. This may explain partially the fact that high blood pressure is always accompanied by renal diseases [52].

An anatomically accurate network of kidney of a mouse is constructed. The information about the geometry of the network is precise. There are 1399 arterial segments, ranging from 0.2 mm to 32.0 mm in length, and from 0.164 mm to 3.745 mm in diameter. Since the elasticity is not known, we set the value in a general sense, $Eh = 0.1 \times 10^4$ Pas$\cdot$ cm. Calculated with those values, the linearized wave speed varies from 150 cm/s to 880 cm/s among the various segments. The boundary conditions are not known neither. At the inlet, we impose a flow rate function with a period of 0.1 s and the total input volume of one period is 1 ml. Accordingly, the peak value of the flow rate is 31.4 ml/s. For the outlet boundary conditions, there are evidences that the reflections are very weak due the low impedance of the renal network [52]. Thus we set non-reflecting boundary conditions at the outlets.

Fig. 4.8 shows the pressure distribution of the network. The propagation of the pulse wave in the arterial tree is clear.

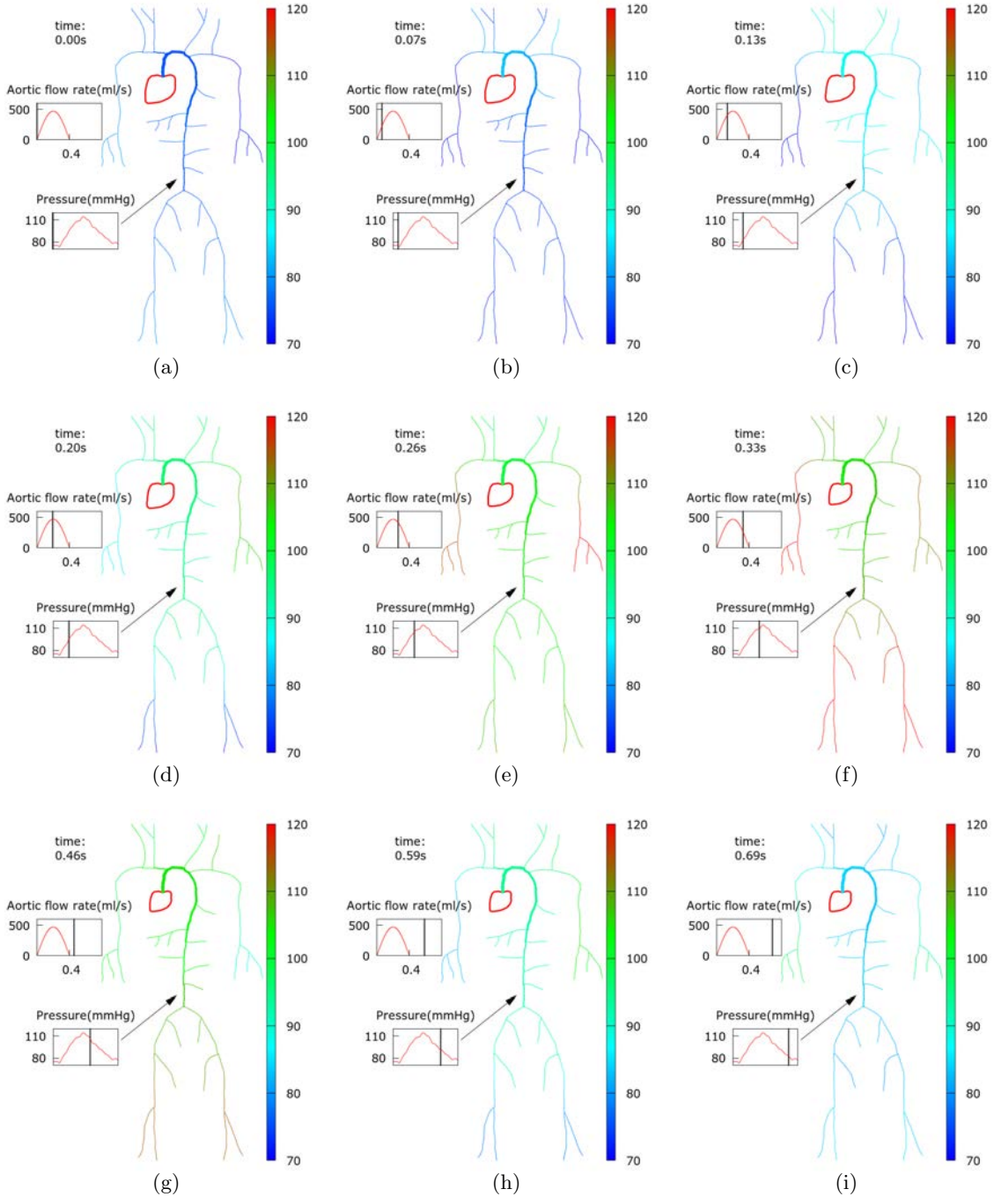

Figure 4.7.: The pressure distribution of the systemic network (mmHg).

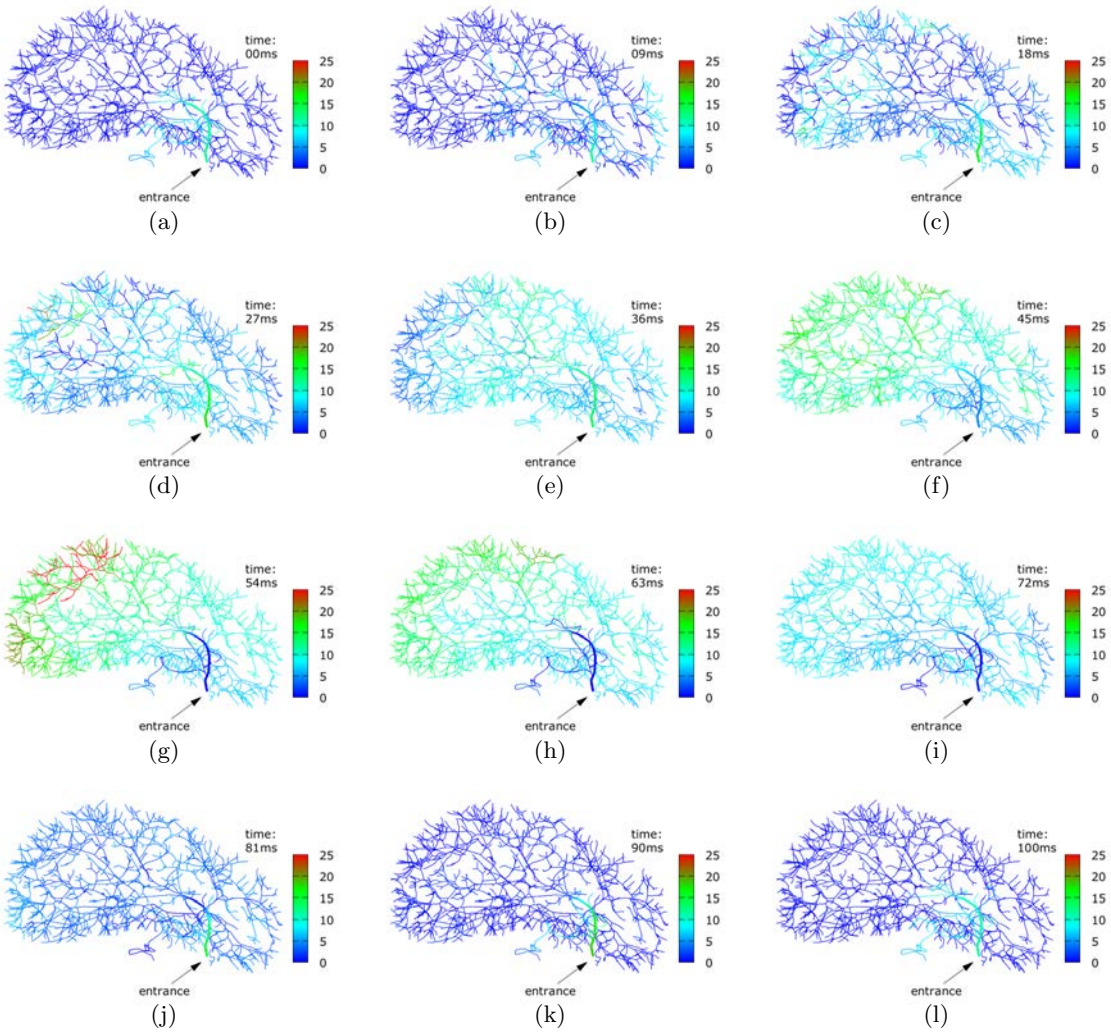

Figure 4.8.: One pulse propagating in a kidney of a mouse (mmHg). In order to see the propagation pattern of the pulse wave in this small network, we make the period arbitrarily short, i.e. 0.1 s.

4.3.4. Speedup of parallelization

The speedup was tested on workstations with 12 cores (Intel(R) Xeon(R) X5650 2.67GHz). We use the tool **time** in the Linux environment to count the time run by the code. For the network of human systemic circulation, we computed 10 cardiac cycles, corresponding to simulating 8 seconds of the network. The time step size was set to 0.01ms, and therefore there are 0.8 million time steps. The number of mesh points in the $i-$th artery is set with the formula

$$N^i = 4\lfloor \frac{L^i/c_0^i}{\min_{i=1}^{i=55}(L^i/c_0^i)} \rfloor,$$

where L is the length and c_0 is the linearized velocity. We roughly have 4 cells in every one centimeter of segment. In fact, this is a quite refined discretization in both time and space. The code runs 20 minutes with one core and 3 minutes with 12 cores. That is to say, for the classic case of the systemic network with 55 segments, we need 18 seconds for one cardiac cycle. For the case of the mouse kidney, we used a mesh with over 20 thousand mesh nodes, and we simulated 0.8 seconds with the time step size set as before. The wall clock time was reduced from 29 minutes with one core to 5 minutes with 12 cores. As shown in Fig. 4.9, the speedup can achieve at about 6 with 12 cores. The difference with the ideal speedup curve may be due to the cache effect because some conjunctions are shared by two processors. The synchronization overhead among the processors may be another barrier for the speedup. The serial part of the code on reading and writing data files takes a few milliseconds, thus their influence on the speedup is minor. To improve the performance of speedup with more cores, implementing it with MPI is a possible approach [18].

4.4. Discussion

Simulating blood flow in networks with the 1D model is a very important approach since it can give distributed information of the blood flow in the network and the computation cost is relatively low. To do a patient-specific simulation, we need a code which is fast and can be set easily for networks of various sizes. We developed a code with two numerical schemes: MacCormack and MUSCL. The MUSCL is shock-capturing and thus the code can be extended to simulate venous flows. The topology of the network is accounted by a DAG, which can describe networks with various types of conjunctions. The computing part of the code is written in C++ with an object oriented approach. The code is parallelized with OpenMP and then tested with networks originated from real problems. Compared with a sequential code, the speedup with 12 cores is about 6. In particular, we can compute one cardiac cycle of the classic arterial tree with 55 segments in order of second, which is reported in recent papers to be done in order of minute [2, 48]. The C++ code reads and writes files in CSV formate. For convenience, we can use a scripting language (like Python) to set the configurations of the simulations and make various post-processing of the computing result.

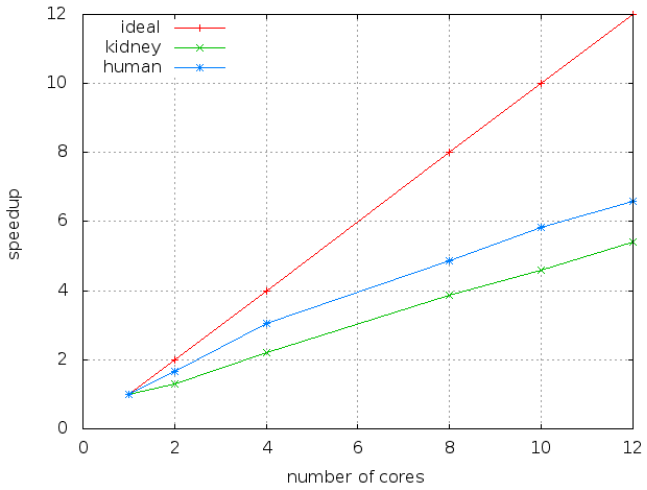

Figure 4.9.: The speedup the two computing cases tested on a workstation with 12 cores.

4.5. Conclusion

In this chapter, we developed a parallel code for the simulation of blood flow in networks. The code was verified and tested on various cases. A good speedup was observed on workstations with multicores. With this code, one cardiac cycle of the classic arterial tree can be computed in order of second. It is also very convenient to setup this code to compute very large networks.

Listing 4.1: piece of code parallelized with OpenMP

```
#pragma omp parallel
{
  int num_streads=omp_get_num_threads();
  // for the conjunctions
  int iStart_con, iEnd_con;
  int chunk_con=ceil( num_conjuncs/float(num_streads) );
  int myID=omp_get_thread_num();
  iStart_con=myID*chunk_con;
  if( (myID+1)*chunk_con-1 < num_conjuncs-1 )
    iEnd_con=(myID+1)*chunk_con-1;
  else
    iEnd_con=num_conjuncs-1;

  // for the arteries
  int iStart_art, iEnd_art
  ...// values set as the case of conjunctions

  while ( currentTime<finishTime ) {
    for ( int i=iStart_con; i<=iEnd_con; i++) {
      if(conjs[i]->isRoot())
        conjs[i]->BC_inflow();
      else if(conjs[i]->isLeaf())
        conjs[i]->BC_outflow();
      else
        conjs[i]->stepMarch();
      }
    #pragma omp barrier

    for(int i=iStart_art; i<=iEnd_art; i++)
      arts[i]->stepMarch();

    currentTime+=stepSize;
    }  // end while
}  // pragma omp parallel end
```

Part II.

Applications

5. Fluid friction and wall viscosity of the 1D blood flow model: study with an in-vitro experimental setup

5.1. Introduction

Although the modeling of blood flow has a long history of development, it is still a very challenging problem until now. Recently the time-domain-based 1D model of blood flow, which is well balanced between modeling complexity and computational cost, has attracted more and more attention (see e.g. [3, 55, 72, 86, 99]). It not only predicts quite well the time-dependent distributions of flow rate and pressure in a network, but also the mechanical properties of the network may be estimated via analysis of the waves. This makes the 1D model useful for many applications, such as non-invasive diagnosis, surgical planning, etc. Moreover, in the context of multi-scale modeling, the 1D model also plays a very important role along with the 3D and 0D (lumped) models.

The basic time-domain-based 1D model predicts nonlinear waves of flow and pressure. There are also many damping factors in the system, such as fluid viscosity, wall viscoelasticity, geometrical changes of vessels (e.g. curvature, bifurcation), etc. Previous studies show that the energy loss at bifurcations is minor [50] and in vessels without drastic geometrical variations (i.e. no severe aneurysms or stenoses), the fluid viscosity and wall viscoelasticity seem the most significant damping factors. Comparisons between the 1D model and *in-vivo* data [32, 64] suggest that the predictions of a viscoelastic 1D model is significantly more physiological than those of an elastic one. But the comparisons were only qualitative or semi-quantitative due to the limited accuracy of non-invasive measurements and the lack of patient-specific parameter values of the 1D model for each subject.

Quantitative comparisons can be done with *in-vitro* experimental setups, which can be well defined and measured. Reuderink et al. [62] connected a distensible tube to a piston pump, which ejects fluid in pulse forms into the tube. The experimental measurements were compared with the predictions of several formulations of the 1D model. In the first formulation, they used an elastic tube law and Poiseuille's theory to account the fluid viscosity. They found this formulation underestimates the damping of the waves and predicts shocks, which were not observed in the experiments. In another formulation, they modeled the fluid viscosity with Womersley's theory and adopted a viscoelastic tube law in the frequency domain. But to use those models, the nonlinear

The experiments were done in Doshisha University (Kyoto, Japan) with the collaboration of Prof. Matsukawa's group.

term (convective term) in the momentum equation of the fluid were neglected. Nevertheless, a better match between the predictions of this formulation and the experiments was found. Bessems et al. [9] built a similar experimental setup and in their simulation they integrated a 3-component Kelvin viscoelastic model to the 1D fluid model. Compared with the 1D model with an elastic tube law, the viscoelastic model predicts waveforms in much better agreement with the experiments. However, to estimate the coefficients of the 3-component Kelvin model, both the convective and fluid viscosity terms were neglected. Alastruey et al. [2] did a comparison study on an experimental setup of a network. They measured the coefficients of a Kelvin-Voigt viscoelastic model with tensile tests instead of fitting them from the waves. They found that the viscoelasticity damps significantly the high frequent components of the waves at the peripheral locations of the network. But for the fluid viscosity term, they adopted a value from literature, which was fitted from waves of coronary blood flow with elastic model for the wall [76].

In this chapter, we study the friction and wall viscoelasticity with the 1D model and a similar experimental setup where pulse waves are propagating in one distensible tube. However, there are three main differences between our study and previous ones:

1. *Both of the two damping factors are evaluated.* Although there are several theories to estimate the friction term (see, e.g. [10, 38, 56]), the value is rarely determined experimentally besides the study of Smith et al. with an elastic model [76]. Since the fluid viscosity and wall viscoelasticity have similar damping influences on the pulse waves, it is difficult to evaluate them separately from pulse waves. However, the viscoelasticity has smoothing effect on the waveforms whereas the fluid friction does not. We take the advantage of this difference and evaluate both of the two factors in this study.

2. *The viscoelasticity of the wall is measured in a new manner.* The viscoelasticity of a solid material is hard to measure accurately, even in an *in-vitro* setup. In our study, the viscoelasticity is determined through the pressure-wall perturbation relation of the vessel under operating conditions. The internal pressure is measured by a pressure sensor and the perturbation of the wall is measured by a Laser Doppler Velocimetry (LDV). Both of the instruments have very high precision and fast response time.

3. *A shock-capturing scheme is applied as the numerical solver.* In a nonlinear hyperbolic system, shocks may arise even if the initial condition is smooth. The Monotonic Upstream Scheme for Conservation Laws (MUSCL) scheme is able to capture shocks without non-physical oscillations. In this paper, the MUSCL is applied to discretize the governing equations alongside with the MacCormack scheme. Solutions of the two schemes are cross compared to check their applicabilities on this problem.

5.2. Methodology

5.2.1. One dimensional model

Let us remind the distensible vessel with a variable internal radius $R(x,t)$, where x is the axial distance and t is the time. The 1D model is on the flow rate Q, cross-sectional area A and internal pressure P. The governing equations describe the conservation of mass and the balance of momentum respectively,

$$\frac{\partial A}{\partial t} + \frac{\partial Q}{\partial x} = 0, \tag{5.1}$$

$$\frac{\partial Q}{\partial t} + \frac{\partial}{\partial x}(\alpha \frac{Q^2}{A}) + \frac{A}{\rho}\frac{\partial P}{\partial x} = -2\pi\nu \left[\frac{\partial v_x}{\partial r}\right]_{r=R}, \tag{5.2}$$

where v_x is the axial velocity, ρ is the fluid density and ν is the kinematic viscosity of the fluid. In general, the profile of axial velocity also depends on the radius coordinate r, v.i.z. $v_x = v_x(r,x,t)$. If we assume the profile has the same shape $\Phi(r)$ in one segment of vessel, the profile function can be separated as $v_x = U(x,t)\Phi(r)$, with U the average velocity. If $\Phi(r)$ is known, both α and the derivative in the friction term can be calculated. The friction drag can thus be approximated by $-C_f U = -C_f Q/A$. The profile $\Phi(r)$ is strongly dependent on the Womersley number defined by $R\sqrt{\omega/\nu}$, where the newly introduced quantity ω is the angular frequency. If ω and ν are considered as constant approximately, only R influences α and C_f, whose values should be determined by experiments for vessels with various diameters. In practice, there are various pairs of values for α and C_f, of which several paris are often seen in literature. In one asymptotic case when the transient inertial force is very large, the profile is essentially flat, then we have $\alpha = 1$. If we introduce a very thin viscous boundary layer to match the inviscid core and a no-slip boundary, the friction term can be estimated (see e.g. [10, 56]). In another asymptotic case, the fluid viscosity force is dominating and a parabolic profile appears. In this case, $\alpha = 4/3$ and the friction term is $-8\pi\nu Q/A$. As fitted by Smith et al. [76] for coronary blood flow, $C_f = 22\pi\nu$ and α is calculated to be 1.1 according to the power law profile proposed by Hughes and Lubliner [35]. Some other literature adopted this value of C_f but assumed $\alpha = 1$ for simplification [2, 48].

To describe the viscoelasticity of the wall, several models have been proposed, see e.g. [32, 84]. Those models incur various levels of difficulties when they are integrated with the 1D fluid model and solved numerically. Comparisons between predictions of the 1D model with different viscoelasticity models show that the difference is minor [61, 77]. We choose the two-component Kelvin-Voigt model, which relates the strain ϵ and stress σ in the equation

$$\sigma = E\epsilon + \phi\frac{d\epsilon}{dt}, \tag{5.3}$$

where E is the Young's modulus and ϕ is a coefficient for the viscosity.

For a tube with a thin wall, the circumferential strain $\epsilon_{\theta\theta}$ can be expressed as

$$\epsilon_{\theta\theta} = \frac{R - R_0}{(1-\eta^2)R_0}, \tag{5.4}$$

where R_0 is the reference radius without loading and η is the Poisson ratio, which is 0.5 for an incompressible material. By Laplace's law, the transmural difference between the internal pressure P and the external pressure P_{ext} is balanced with the circumferential stress $\sigma_{\theta\theta}$ in the relation

$$P - P_{ext} = \frac{h\sigma_{\theta\theta}}{\pi R}. \tag{5.5}$$

Combining Eq. 5.3, 5.4 and 5.5, we have

$$P - P_{exp} = \nu_e(R - R_0) + \nu_s \frac{dR}{dt}, \tag{5.6}$$

with

$$\nu_e = \frac{Eh}{(1-\eta^2)A_0}, \text{ and } \nu_s = \frac{\phi h}{(1-\eta^2)A_0}.$$

Note that the R in the denominators of the two coefficients is approximated by R_0 under the assumption that the perturbations are small.

If we assume P_{ext} is constant and insert Eq. 5.6 into the 1D momentum equation to remove P, the governing equations can be transformed into

$$\frac{\partial A}{\partial t} + \frac{\partial Q}{\partial x} = 0, \tag{5.7}$$

$$\frac{\partial Q}{\partial t} + \frac{\partial}{\partial x}\left(\alpha \frac{Q^2}{A} + \frac{\beta}{3\rho} A^{\frac{3}{2}}\right) = -C_f \frac{Q}{A} + C_v \frac{\partial^2 Q}{\partial^2 x}, \tag{5.8}$$

where

$$\beta = \frac{\sqrt{\pi} Eh}{(1-\eta^2)A_0}, \text{ and } C_v = \frac{\sqrt{\pi}\phi h}{2\rho(1-\eta^2)\sqrt{A_0}}.$$

For this formulation of the 1D model, there are detailed discussions on the treatment of boundary conditions and numerical solvers in [93].

5.2.2. Experimental setup

The experimental setup is shown in Fig. 5.1. The piston pump (TOMITA Engineering) injects fluid (water) into the home-made polyurethane tube. The output of the pump is a sinusoidal function in time, whose period and duration can be programmed through a computer. At the measurement point, a pressure sensor (Keyence, AP-10S) is inserted into the tube. The perturbation of the tube wall is measured by a LDV (Polytec, NLV-2500). The pump, the pressure sensor and the LDV are controlled by a computer, which synchronizes the operations of the instruments and stores the measurement data. The end of the tube is closed by a stainless rod and thus a total reflection boundary condition is imposed at the outlet. Pulse waves are bounced backward and forward in the tube multiple times before equilibrium state is restored. We measured at two points, A and B, which locate close to the proximal and distal ends of the tube respectively. Table 5.1 summarizes the parameters of the tube and fluid: the thickness of the wall h, the reference diameter D, the total length of the tube L, the distances from the inlet to the two measurement points L_A and L_B, the fluid density ρ and the kinematic viscosity ν.

h (cm)	D (cm)	L (cm)	L_A (cm)	L_B (cm)	ρ (kg/cm^3)	ν (cm^2/s)
0.2	0.8	192	28.3	168.2	1.050×10^{-3}	1×10^{-2}

Table 5.1.: Parameters of the tube and fluid.

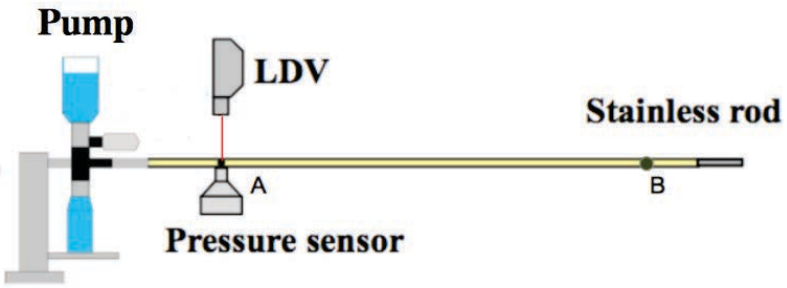

Figure 5.1.: Experimental setup. Parameters of the tube and fluid are summarized in Table 5.1.

5.2.3. Parameter estimation

We estimated the fluid friction and wall viscoelasticity by fitting the pressure wave with the nonlinear 1D model. To improve the confidence on the estimation, we also measured the viscoelasticity with two more methods: analysis of the pressure-wall perturbation and tensile test.

Data fitting via the 1D model

The 1D model was numerically solved by MacCormack and MUSCL methods, see [19, 93] for more details. In the experiments, we imposed a half sinusoidal wave of flow rate as the output function of the pump, see Fig. 5.2(a). Since the velocity of pulse wave is directly related with the stiffness, we fit the Young's modulus by matching the arrival times of the wave peaks. Because the amplitude of the wave is damped by both the fluid friction and wall viscosity, we fitted those two factors in pairs. The fitting was done on both the two measurement points A and B, and the consistency of the results estimated from the two sets of data was checked.

Pressure-Wall perturbation

To generate a pulse perturbation, we imposed a sinusoidal wave of one full period for each time of test, see Fig. 5.2(b). The net volume of fluid injected into the tube was zero, so the tube would return to the original state finally. Fig. 5.3 shows the time series of pressure and wall displacement, which were measured simultaneously at one point. We can see that the wave is reflected several times at each end of the tube and the amplitude is damped roughly exponentially. After about 6 seconds, the tube restores to the initial equilibrium state. The energy loss due to the wall viscosity is the work done during the

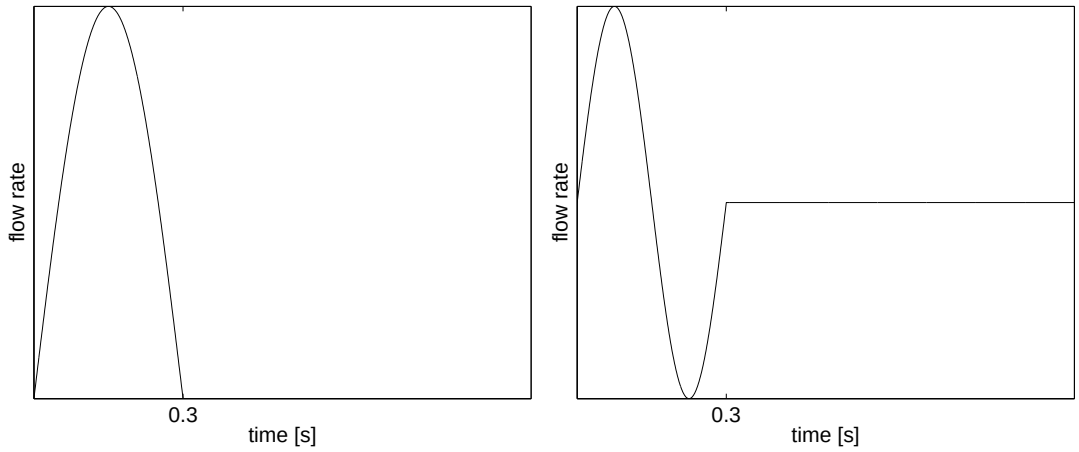

(a) (b)

Figure 5.2.: Output function of the pump for the two tests. Left (a): data fitting vie the 1D model, and right (b): Pressure-Wall perturbation. The actual waveform may deviate slightly from this ideal one due to experimental uncertainties.

test. Assuming that the test starts at $t = t_0$, where $R = R_0$ and ends at $t = t_e$ where $R = R_e$, we integrate the viscoelastic tube law (5.6) along the path of the moving wall from t_0 to t_e,

$$\int_{R_0}^{R_e} P dR = \int_{R_0}^{R_e} \left[P_{ext} + \nu_e(R - R_0)\right] dR + \nu_s \int_{R_0}^{R_e} \frac{dR}{dt} dR.$$

Because the radius at the start and the end of the recorded time interval is the same, $R_0 = R_e$, and the external pressure P_{ext} is constant, the first term on the right hand side disappears. Thus we obtain

$$\nu_s = \frac{\int_{t_0}^{t_e} P \frac{dR}{dt} dt}{\int_{t_0}^{t_e} (\frac{dR}{dt})^2 dt}.$$

But the relationship between dR/dt and the wall velocity V_w measured by LDV is not straightforward. In the experiment, the tube was put on a desktop in air and the wall perturbation was measured from the top (see Fig. 5.1). If we assume the mass center of each cross section essentially doesn't change due to the inertial force, we have $dR/dt = V_w$. However, if the inertial force is neglected, we may assume $dR/dt = V_w/2$. In reality, the change rate of the radius should fall between the two values, so we estimated a range between the two extreme cases. After the viscosity part is subtracted, the elastic coefficient can then be estimated using linear regression.

Tensile test

We prepared some specimens of the polymer of the vessel wall for a tensile test machine (Shimadzu EZ test). The specimens were elongated at a rate of 0.5 m/min and then

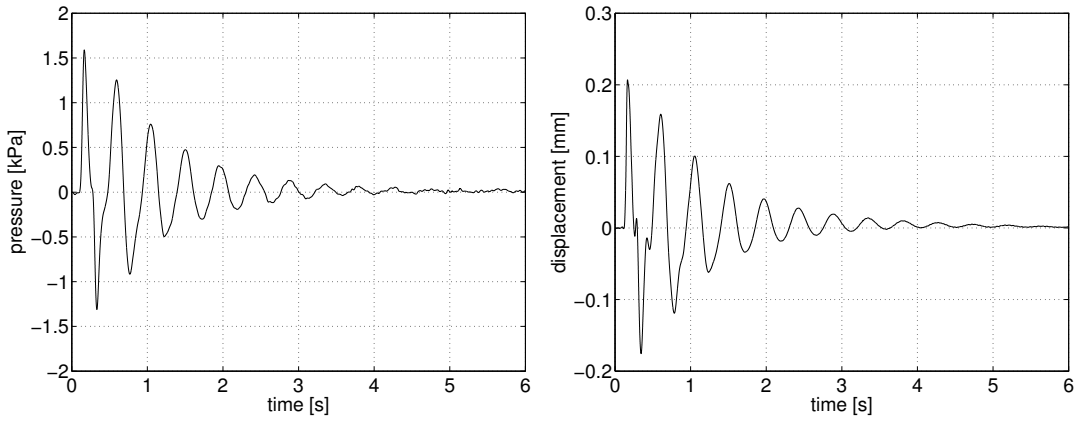

(a) (b)

Figure 5.3.: Simultaneous recording of pressure and displacement of wall at one location: left (a) pressure, right (b) displacement.

released at the same rate. Fig. 5.4 shows one example where the tension force F is plotted as a function of elongation ΔL. We applied least square method to fit the curve against a linear function $F = C_0 + ES\Delta L/L$, where C_0 is a constant, E is the Young's modulus, S is the cross-sectional area of the specimens and L is the original length. The Young's modulus was then calculated from the slope of the fitted line. The viscosity was not estimated with this method.

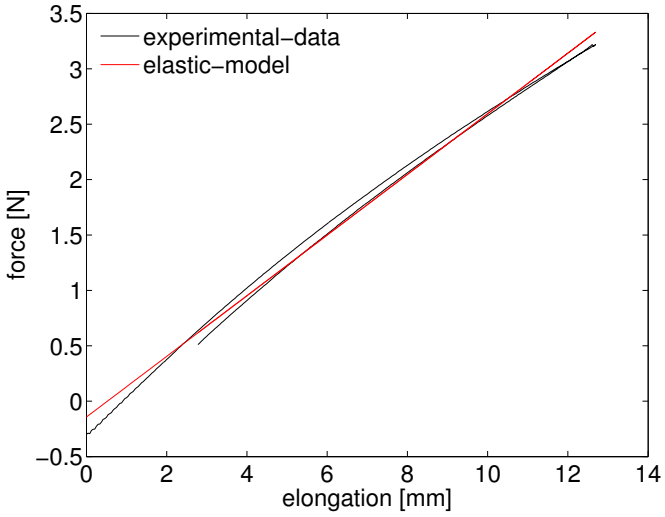

Figure 5.4.: Tensile test and linear regression with the linear elastic model.

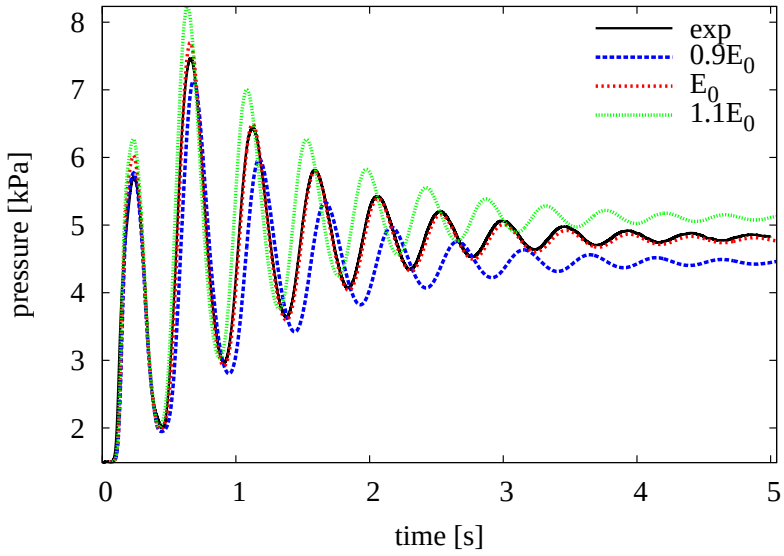

Figure 5.5.: Pressure time series at measurement point A. E_0 is the best fit for the Young's modulus. If E_0 is perturbed 10%, the arrival time of each peak changes significantly. $C_f = 22\pi\nu$ and $\phi = 0.9$ kPa $\cdot$ s.

5.3. Results

5.3.1. Young's modulus

We have the best fit between the 1D model and the experiment when $E = E_0 = 2.08 \times 10^5$ Pa. This value falls in the range estimated with the P-W perturbation method and is about 8% bigger than the tensile test value. Besides the test error, the variance in the home-made polymer tubes may also contribute to the difference. Fig. 5.5 compares the experiment with the 1D model when E has a variance of 10% around E_0. The arrival time of each peak is significantly later if E decreases and vice versa. Please note that the final state has a higher pressure than the initial state. That is because this time we imposed a half sinusoidal wave at the inlet and thus a net volume of about 4.5 cm^3 fluid was injected into the tube.

5.3.2. Fluid friction and wall viscosity

It is more tricky to fit the friction and wall viscosity terms because both of them are damping factors. First we used an elastic model and varied the friction coefficient. Fig. 5.6 shows the waves with three values of friction coefficient C_f: $8\pi\nu$, $22\pi\nu$ and $33\pi\nu$. With the first value, which is derived from a parabolic velocity profile, the predicted pressure wave has two features: overestimated amplitude and shocks, which obviously contradict the measurement. The second value is fitted from coronary blood flow by Smith et al. [76], and the amplitude becomes closer to the experimental one. The third

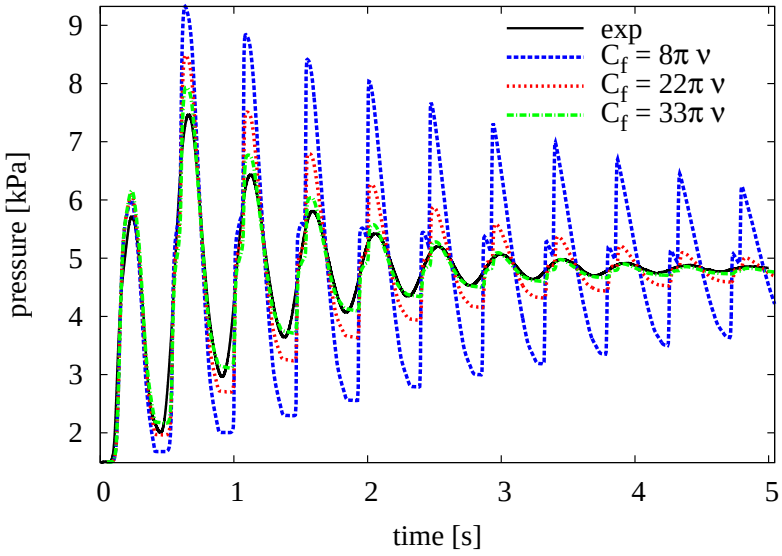

Figure 5.6.: Pressure time series at measurement point A. The elastic model predicts shocks. Increasing the friction term can damp the amplitude effectively, but the shocks still exist. $E = 2.08 \times 10^5$ Pa and $\phi = 0$.

value predicts the best in amplitude but the shocks still exist.

	wave1	wave2	wave3	wave4	wave5	wave6	wave7
$C_f(\pi\nu)$	8	14	18	22	26	30	33
ϕ(kPa · s)	2.0	1.6	1.3	1.0	0.8	0.5	0.4
NRMS (%)	1.96	1.75	1.66	1.64	1.74	1.92	2.15

Table 5.2.: Parameters of fluid friction and wall viscosity and the corresponding NRMS.

To make quantitative comparisons, the Normalized-Root-Mean-Square (NRMS) error is defined by

$$NRMS = \frac{1}{\max(P_{exp}) - \min(P_{exp})} \sqrt{\frac{\sum (P_{sim} - P_{exp})^2}{N}},$$

where N is the number of data points. We fixed C_f at a series of values ranging from $8\pi\nu$ to $33\pi\nu$ and fitted ϕ by varying its value to minimize the NRMS. Around the estimated minimum point, ten values of ϕ were tested with a step size of 0.1 kPa·s. As an example, Fig. 5.7 shows NRMS as a function of ϕ when $C_f = 22\pi\nu$. In this case, 1.0 kPa·s is obviously the minimum point. Table 5.2 summarizes the tested values of C_f, the minimum points of ϕ and the corresponding residuals of NRMS. From wave1 to wave7, the value of C_f increases and that of ϕ decreases. The residual achieves a minimum at wave4 and the worst cases are wave1 and wave7 at the two ends of the table.

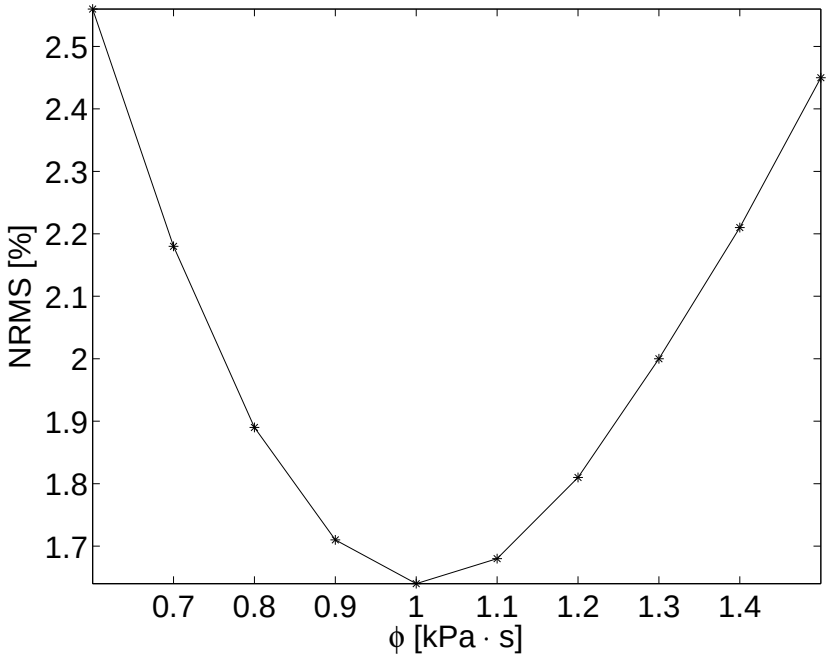

Figure 5.7.: Normalized-Root-Mean-Square error as a function of wall viscosity. $E = 2.08 \times 10^5$ Pa, and $C_f = 22\pi\nu$.

In Fig. 5.8, wave4 is plotted alongside wave1 and wave7. First we notice that the shocks disappear and the amplitude of the three waves is very close to the experimental data. However, in the first two seconds, the wave-front of wave7 is more steepened than others. This difference is more clear in the plot of spectrum (Fig. 5.9), which shows that the high frequent components of wave7 are underdamped. This is because the damping effect of wall viscosity is stronger on high frequent waves while that of fluid friction does not depend on frequency in our model. In the last several seconds, only the main hormonic is left, thus the difference between the three simulated waves is very small. With wave4, we can estimate that $C_f = 22\pi\nu$ and $\phi = 1.0$ kPa $\cdot$ s. The viscoelastic parameters estimated with various methods are summarized in Table 5.3. The values estimated by the data fitting with the 1D model fall into the range measured by the P-W perturbation. Even though the tensile test does not give reliable information on the wall viscosity, this method estimates a very close Young's modulus as the 1D model.

method	E (10^5 Pa)	ϕ (kPa $\cdot$ s)
Fitting with the 1D model	2.08	1.0
P-W perturbation	1.45—2.90	0.97—1.94
Tensile test	1.92±0.06	-

Table 5.3.: Viscoelasticity of the polymer.

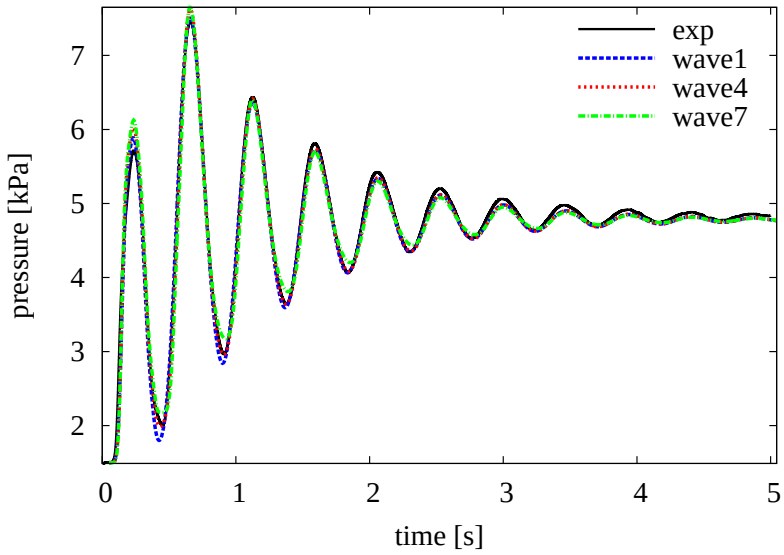

Figure 5.8.: Pressure time series at measurement point A. $E = 2.08 \times 10^5$ Pa. The values of C_f and ϕ for the three simulated waves are shown in Table 5.2.

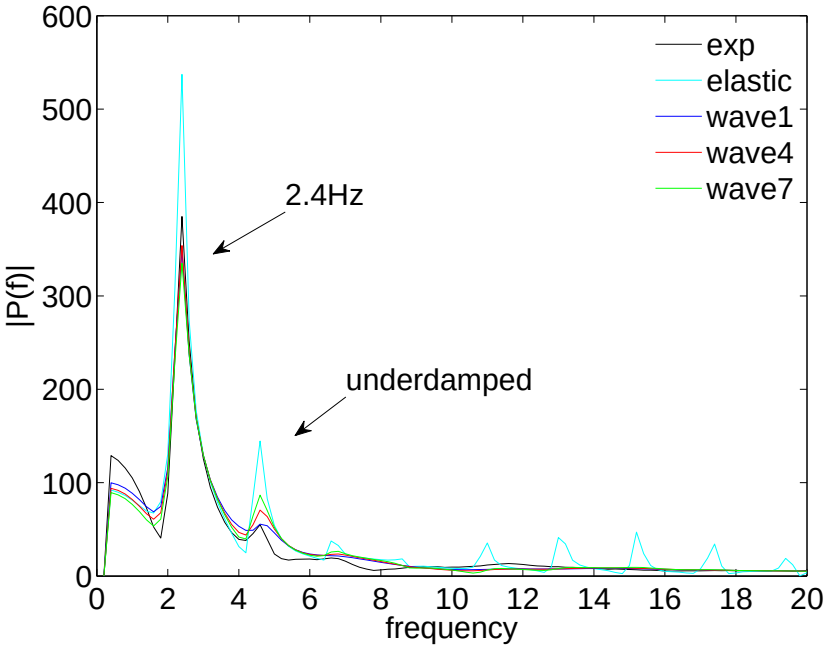

Figure 5.9.: Spectrum of the pressure series (only frequencies less than 20 Hz are shown). $E = 2.08 \times 10^5$ Pa. For the elastic case, $C_f = 22\pi\nu$ and $\phi = 0$. The values of C_f and ϕ for the three viscoelastic waves are shown in Table 5.2.

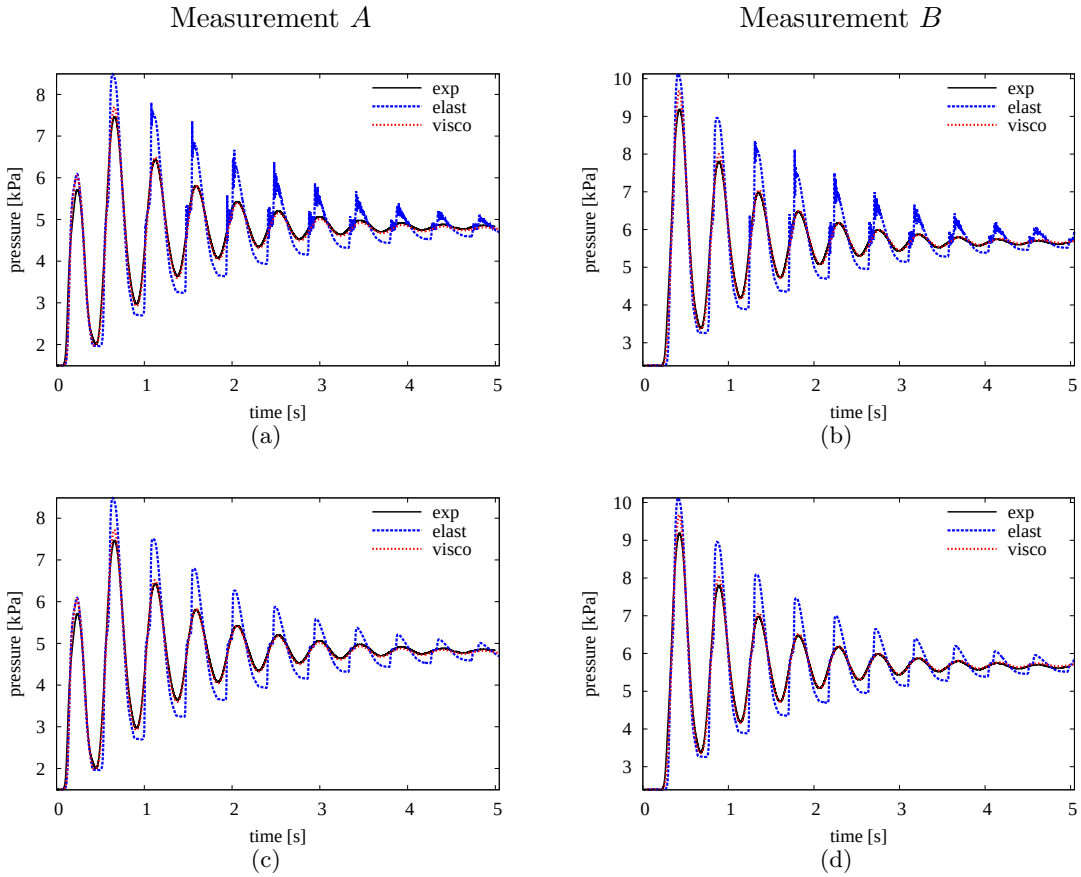

Figure 5.10.: Pressure time series at the two measurement points with two numerical schemes. Left column: point A, right column: point B. Top row: MacCormack method, bottom row: MUSCL method. The viscoelastic model predicts much better than the elastic model at both the measurement points. The MUSCL method depresses the numerical oscillations when there are shocks. The parameters are: $E = 2.08 \times 10^5$ Pa, $C_f = 22\pi\nu$, and ϕ=1.0 kPa $\cdot$ s (visco).

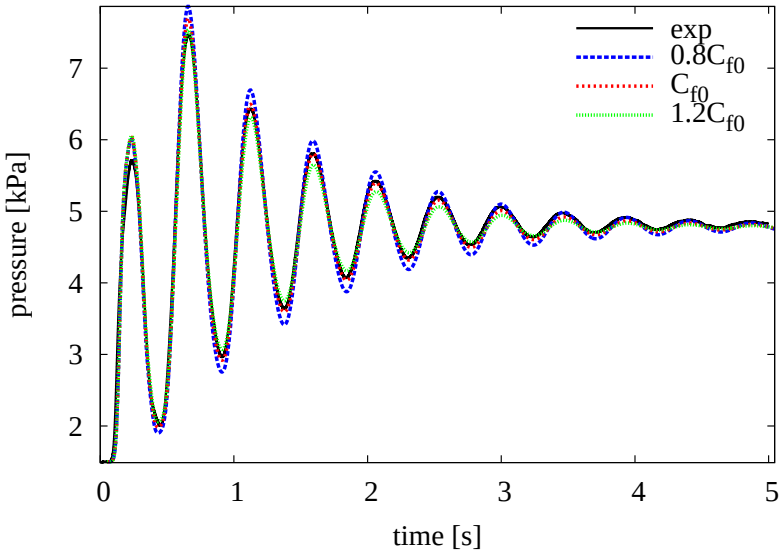

Figure 5.11.: Time series of pressure with a 20% uncertainty of C_f.

In Fig. 5.10, we plotted the pressure waves at the two measurement points: left column for point A and right column for point B. The shocks predicted by the elastic model are very obvious. The MacCormack scheme produces numerical oscillations (top row) whereas the MUSCL scheme depresses them because of a slope limiter of this scheme (bottom row). For the viscoelastic model, the shocks disappear and a much better agreement is achieved at both the locations. If the solution is quite smooth, there is essentially no difference between the two numerical schemes in accuracy. The good consistency between the tests at the two locations gives us more confidence on the experiments and numerical simulations.

We also tested the sensitivity of the model output to the uncertainty of the four parameters: E, C_f, ϕ and α. As shown by Fig. 5.5, a perturbation of 10% of E can change significantly the predicted waves, both on the amplitude and velocity. For C_f and ϕ, an uncertainty of about 20% produces a moderate variance on the predicted wave (see Fig. 5.11 and 5.12). The sensitivity of the output to C_f and ϕ is in the same order. In contrast, if α varies in the range from 1.0 to 1.3, there is no noticeable difference between the predictions (see Fig. 5.13).

5.4. Discussion

With a well defined and measured experimental setup, we investigated the parameters of a nonlinear 1D viscoelastic model of blood flow. A small variance of stiffness can change significantly the mean pressure, pulse pressure and wave velocity. The value of vessel stiffness can be estimated precisely by the 1D model. It shows again that the 1D model is a very promising tool of diagnosis of the cardiovascular system.

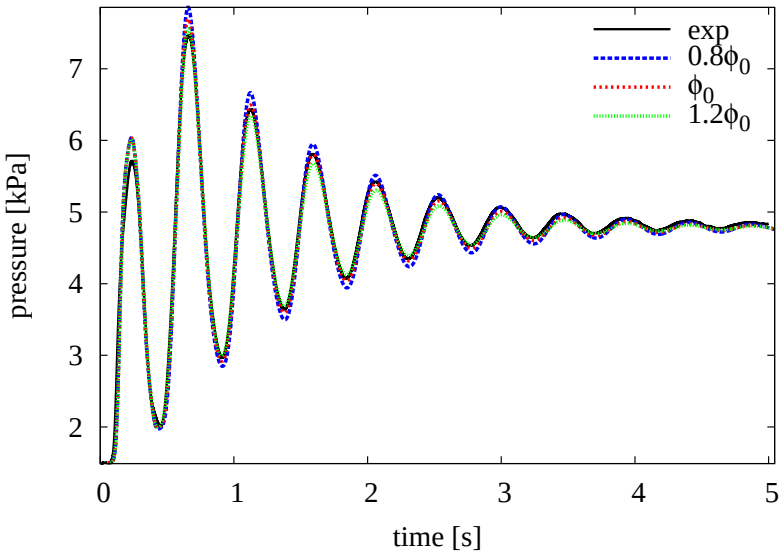

Figure 5.12.: Time series of pressure with a 20% uncertainty of ϕ.

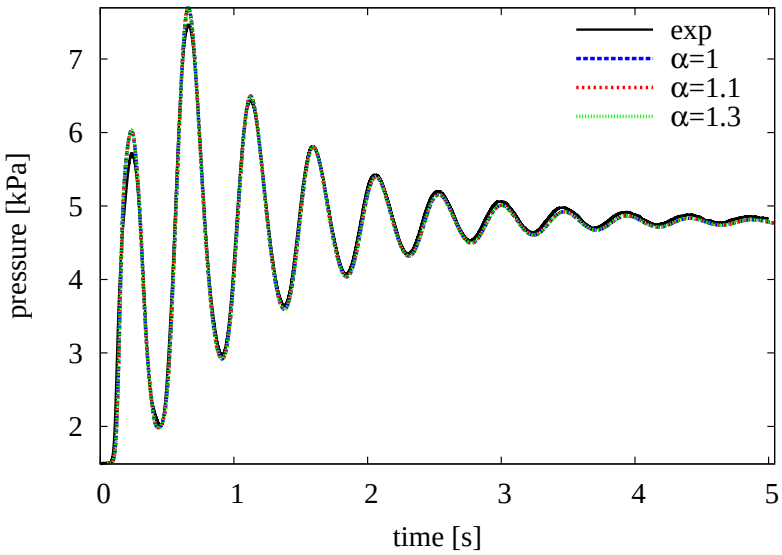

Figure 5.13.: Time series of pressure with various values of α.

Previous studies show that wall viscosity damps the waveform considerably (see e.g. [2, 32, 60, 70]). However, its influence on the pulse wave is very difficult to be evaluated in isolation, since the fluid friction is also a considerable damping factor, which is not easy to be determined precisely. Previous studies usually make *a priori* estimations on the fluid friction or even totally neglect this term. The fluid friction is strongly dependent on the Womersley number and thus various approximation methods have been proposed [10, 35, 38, 56]. Fitted with an elastic model for coronary blood flow, Smith et al. [76] determined the friction coefficient as $22\pi\nu$. This value is widely seen in recent literature (e.g. [2, 48, 95]) along with the value $8\pi\nu$, which is derived from a parabolic (poiseuille) velocity profile (e.g. [78, 102]).

Among several models proposed for the viscoelasticity of the wall, we chose the Kelvin-Voigt model, which can be readily integrated into the 1D governing equations. Armentano et al. [4] measured the pressure and diameter simultaneously of *in-vivo* arteries and fitted the Kelvin-Voigt model to estimate the viscosity coefficient in a range from 3.8 ± 1.3 kPa $\cdot$ s to 7.8 ± 1.1 kPa $\cdot$ s. Alastruey et al. [2] measured the viscosity of a polymer by tensile test and found a value of 3.0 ± 0.3 kPa $\cdot$ s.

In this study, we solved the nonlinear 1D viscoelastic model with MacCormack and MUSCL schemes. The elastic model predicts shocks, which are captured by the MUSCL method without non-physical oscillations. The fluid friction and wall viscosity were fitted in pairs with the 1D model. We obtained quite good agreement between the 1D model and experiments. If experimental uncertainties are considered, it can be estimated that $C_f = 22 \pm 4\pi\nu$ and $\phi = 1.0 \pm 0.3$ kPa $\cdot$ s (determined by wave3 and wave5 in Table 5.3). In our study, the frequency of the main harmonic is 2.4 Hz (see Fig. 5.9) and thus the Womersley number is about 15.5. The blood flow in the main aorta of an adult human is also featured with such a value. This confirms that in cases of blood flow with a similar characteristic Womersley number, the Poiseuille model underestimates the fluid friction (see e.g. [67]). The widely used value $C_f = 22\pi\nu$ in large arteries is acceptable. However, in smaller arteries, the Womersley number can be less than one, so parabolic velocity profile is more likely to appear, which implies that C_f decreases to $8\pi\nu$. Thus the friction term should vary through the whole cardiovascular system and a smaller value of C_f should be considered if the Womersley number is much smaller.

The viscoelasticity of the wall damps the high frequent components of the wave, thus the waveform is not very front-steepened, which has been pointed out by many previous studies (see e.g. [2, 32]). A perturbation of 20% on wall viscosity introduces moderate variances on pressure waveform, which is similar with the fluid friction (see Fig. 5.11 and 5.12). The output of the 1D model is not very sensitive to uncertainties of the two damping factors. Thus it is possible to use general values of those two parameters even in patient-specific simulations with the 1D model. But on *in vivo* conditions, the wall viscosity is much larger as measured by Armentano et al. [4] and the surrounding tissues of the vessel such as fat may also damp the waves like wall viscosity. Thus neither of the two viscous factors should be neglected if delicate details of the waves are required. Moreover, the test on α shows that its variance in the range from 1.0 to 1.3 almost does not influence the waveform (see Fig. 5.13).

5.5. Conclusion

We studied the parameters of the nonlinear 1D viscoelastic model with a well defined and measured experimental setup. The 1D model was solved by two schemes, one of which is shock-capturing. The fluid friction and wall viscosity were fitted in pairs with data measured at two locations. The estimated viscoelasticity parameters were in consistent with values obtained with other methods. The good agreement between the predictions and the experiments indicates that the nonlinear 1D viscoelastic model can simulate the pulsatile blood flow very well. We showed that the influence of wall viscosity on the waveform is in the same order of that of fluid friction. Both of them should not be neglected if delicate details of waveform are required.

6. Effect of viscoelasticity of arterial wall on waves of blood flow: a study on network of sheep

6.1. Introduction

The medical value of the pulsatile waveform of the blood flow has attracted human's attention for a long history. For instance, in the ancient civilization of China [29], there are many records of diagnosis methods based on the pulse waves. But those methods are described by qualitative words and there is a lack of experimental observations for the theories behind the methods. Thus it is hard to make those methods to be accepted by the major of modern medical community, even though some people believe the methods have some empirical values.

Starting from the original contribution of Euler in the 18^{th} century, many mathematicians and physicists have improved the math modeling of the pulse waves (for more details, see e.g. [54, 72]). Simulations of blood flow in networks with the one-dimensional model have been validated favorably with both *in vitro* experimental [2, 67, 92] and *in vivo* clinical data [20, 56, 63, 64, 78, 81]. Because the 1D model is well balanced between modeling complexity and computational cost, it has a lot of potential applications, ranging from non-invasive diagnosis, to optimization of surgery planning, to performing as an important part in multi-scale modeling.

However, challenges still exit for patient-specific simulations. One of them is due to the complex mechanical properties of the arterial wall. In the 1D model, a constitutive equation of the tube is necessary to close the system of conservation laws of mass and momentum. Although the viscoelastic behaviour of the wall has been recognized as a fundamental factor for a long time, most 1D simulations existing in literature adopted elastic models for simplicity.

Nevertheless, there are several studies of blood flow in network with viscoelastic 1D model. The viscoelastic models of arterial wall fall into roughly two classes: Fung's quasilinear viscoelastic models [28] and spring-dashpot models. The first kind of models are more generalized. But they are more difficult to handle when incorporated with the 1D model of blood flow, because they involve a creep function and convolutions have to be computed [77]. Holenstein et al. [32] proposed a model of the first kind and fitted the parameters from published data. The viscoelastic model makes considerable different predictions than the elastic one. Reymond et al. [63, 64] adopted Holenstain's

The animal experiments were done in Favaloro University (Buenos Aires, Argentine) by Prof. Armentano's group.

model and parameter values in their patient-specific simulations. The comparison between numerical results and *in vivo* measurements reveals a considerable impact of the viscoelasticity on the pulse waves. A comparison between the predictions of the 1D model with different viscoelastic models of the first kind shows that the difference is minor [61]. Segers et al. [70] incorporated a frequency dependent viscoelastic model with the linearized 1D model of blood flow. They found that the influence of viscoelasticity is comparable with that of the elastic nonlinearity [61]. We note that the parameter values of the viscoelastic model in those studies are fitted from limited available data in literature.

The second class of viscoelastic models are in analogy to combinations of springs and dashpots. One of them is the Kelvin-Voigt model which consists of one spring and one dashpot connected in parallel. The Kelvin-Voigt model is suitable to describe viscoelastic solids and it is straightforward to be incorporated with the 1D model of blood flow. Armentano et al. [4] fitted the Kelvin-Voigt model with the time series of diameter and pressure which were measured simultaneously. Good agreements between the Kelvin-Voigt model and measurements were obtained at various locations of the arterial network. Alastruey et al. [2] also adopted the Kelvin-Voigt model and estimated the parameters by tensile test. They simulated the pulsatile flow in an *in vitro* experimental setup and compared this model with an elastic one. The viscoelastic model agrees much better with measurements than the elastic one. We note that the vessels in the study were made of polymers which are actually much less viscous than the real arterial wall.

In this paper, the effect of viscoelasticity on the pulse waves was investigated on the arterial network of sheep. The simultaneous time series of diameter and pressure at several arteries were collected from a group of sheep. The viscoelasticity coefficients were estimated by fitting the measurements against the Kelvin-Voigt model. The pulsatile blood flow in the network was then computed with a nonlinear 1D viscoelastic model. We observed the smoothing effect of the wall viscosity on the pulse waveforms.

6.2. Methodology

6.2.1. Data acquisition

The experimental data were obtained from a group of eleven sheep (male Merino, between 25 and 35 kg). Before surgeries, the animals were anesthetized with sodium pentobarbital (35 mg/kg). The arterial segments of interest (6 cm long) were separated from the surrounding tissues. To measure the diameter, two miniature piezoelectric crystal transducers (5 MHz, 2 mm in diameter) were sutured on opposite sides into the arterial adventitia. The animals were then sacrificed and the arterial segments of interest were excised for *in vitro* test.

The arterial segments were mounted on a test bench where a periodical flow was generated by an artificial heart (Jarvik Model 5, Kolff Medical Inc., Salt Lake City, USA). The circulating liquid was an aqueous solution of Tyrode. At each arterial segment the internal pressure was measured using a solid-state pressure micro-transducer (Model P2.5, Konigsberg Instruments, Inc., Pasadena, USA), previously calibrated us-

ing a mercury manometer at 37 degrees. The arterial diameter signal was calibrated in millimeters using the 1 mm step calibration option of the sono-micrometer (Model 120, Triton Technology, San Diego, USA). The transit time of the ultrasonic signal with a velocity of 1,580 m/s was converted to the vessel diameter. The experimental protocol was conformed to the *European Convention for the protection of Vertebrate Animals used for Experimental and Scientific Purposes*. For more details on the animal experiments, please refer to [85].

The synchronized recording of transmural pressures and diameters was applied on the following seven anatomical locations as shown in Figure 6.1: Ascending Aorta (AA), Proximal Descending aorta (PD), Medial Descending aorta (MD), Distal Descending aorta(DD), Brachiocephalic Trunk (BT), Carotid Artery (CA) and Femoral Artery (FA). The time series of radius and pressure recorded at AA of one sheep are shown in Figure 6.2 as an example.

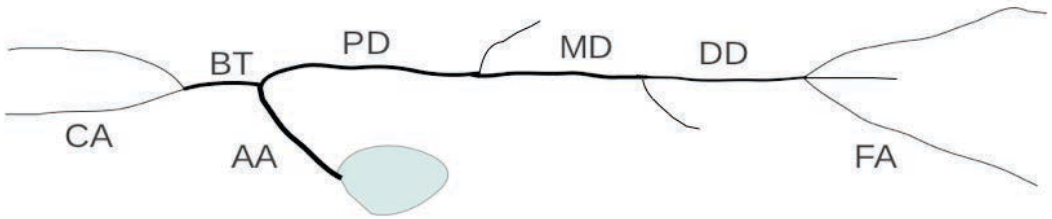

Figure 6.1.: Arterial tree of sheep. Experimental data are collected from eleven sheep at the following seven locations: Ascending Aorta (AA), Proximal Descending aorta (PD), Medial Descending aorta (MD), Distal Descending aorta (DD), Brachiocephalic Trunk (BT), Carotid Artery (CA) and Femoral Artery (FA). There are three virtual arteries (VA), which are indicated by dashed lines, to model the side branches when pulse waves are simulated. Parameters for all the arteries are shown in Table 6.1.

6.2.2. Evaluation of the parameters of the arterial wall

For the Kelvin-Voigt model, the tensile σ and the strain ϵ are related by the equation

$$\sigma = E\epsilon + \phi\frac{d\epsilon}{dt}, \tag{6.1}$$

where E is the Young's modulus and ϕ is the wall viscosity.

We assume that the arterial wall is thin, isotropic, incompressible and homogeneous with a thickness h. Each cross section is circular with an internal radius R. Driven by the transmural pressure $P - P_{ext}$ (P_{ext} is the external pressure), each cross section deforms axisymmetrically and independently of others. By Laplace's law, $P - P_{ext}$ is related with the stress σ by the equation

$$\sigma = \frac{R(P - P_{ext})}{h}. \tag{6.2}$$

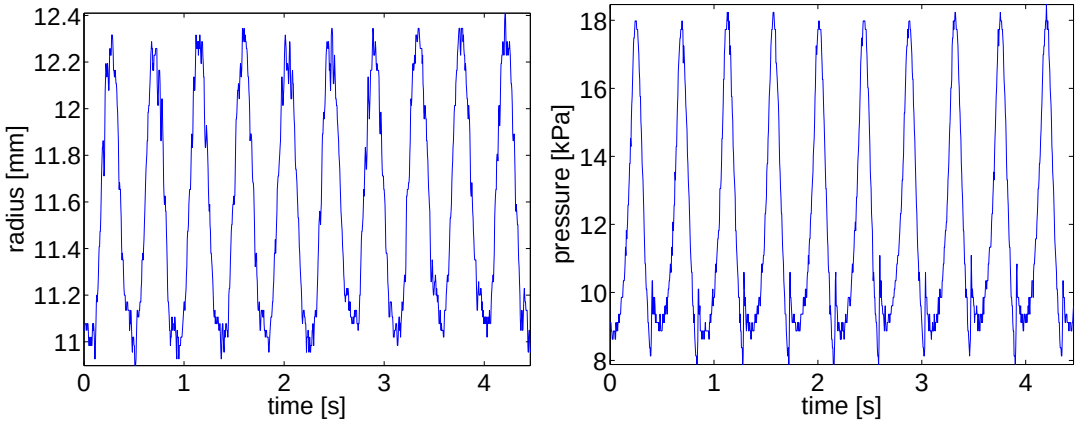

Figure 6.2.: Time series of radius (left) and transmural pressure (right) recorded at the ascending aorta for one of the eleven sheep.

Denoting the reference radius by R_0, the strain ϵ can be expressed as

$$\epsilon = \frac{1}{1-\eta^2}\frac{R-R_0}{R_0}, \tag{6.3}$$

where η is the Poisson ratio and it is 0.5 for incompressible materials. By substituting equations (6.2) and (6.3) into equation (6.1) and rearranging, we get

$$P - P_{ext} = \frac{Eh}{(1-\eta^2)R_0} - \frac{Eh}{(1-\eta^2)}\frac{1}{R} + \frac{\phi h}{(1-\eta^2)R_0}\frac{dR}{Rdt}. \tag{6.4}$$

The transmural pressure has a linear relationship with the quantities $1/R$ and $(dR)/(Rdt)$. The coefficients can be estimated by linear regression from experimental data. In particular, the numerical derivative of R with respect to t is evaluated with a spectral method. The thickness h is measured in the animal experiments and thus the values of reference radius R_0, Young's modulus E and viscosity coefficient ϕ can be calculated from the fitted coefficients.

6.2.3. Simulation of pulse waves with the 1D model

For blood flow in arteries, if we denote the circular cross-sectional area by A, the flow rate by Q and the internal pressure by P, the conservation of mass and balance of momentum are expressed in two partial differential equations (PDEs):

$$\frac{\partial A}{\partial t} + \frac{\partial Q}{\partial x} = 0, \tag{6.5}$$

$$\frac{\partial Q}{\partial t} + \frac{\partial}{\partial x}\left(\frac{Q^2}{A}\right) + \frac{A}{\rho}\frac{\partial P}{\partial x} = -C_f\frac{Q}{A}, \tag{6.6}$$

where x is the axial distance and t is the time. The blood density ρ is assumed a constant, and C_f is the skin friction coefficient which depends on the shape of the velocity

profile. In general, the profile depends on the Womersley number which is defined as $R\sqrt{\omega/\nu}$, with ω the angular frequency of the pulse wave and ν the kinematic viscosity of the fluid. In practice, C_f usually takes an empirical value fitted from experimental observations. In this study, we assume $C_f = 22\pi\nu$ as fitted for the blood flow in large vessels with a Womersley number of about 10 [76]. Those two PDEs are accompanied by the constitutive equation (6.4), which can be transformed to

$$P = P_{ext} + \beta(\sqrt{A} - \sqrt{A_0}) + \nu_s \frac{\partial A}{\partial t}, \tag{6.7}$$

with

$$\beta = \frac{\sqrt{\pi}Eh}{(1-\eta^2)A_0}, \quad \nu_s = \frac{A\sqrt{\pi}\phi h}{2(1-\eta^2)\sqrt{A_0}}.$$

Those are the governing equations for the blood flow in one segment.

At the conjunction points between segments, the conservation of mass and momentum is preserved. The energy loss due to the variation of geometry is neglected. At the inlet of the network (AA), the flow rate is a cyclic half sinusoidal function in time with a period of 0.5 s. At the outlets, proper reflection coefficients are imposed. The governing equations are solved numerically by Monotonic Upstream Scheme for Conservation Laws (MUSCL) and MacCormack methods, which give essentially the same results. The code has been favorably validated by analytical results and experimental data, see [92, 93].

6.3. Results

6.3.1. Parameters of the arterial wall

Figures 6.3 and 6.4 show the hysteresis loops and time series at the seven arteries. The comparison between the measurements and the model shows that the Kelvin-Voigt model captures quite well the wall viscosity. The modeling error mainly comes from the nonlinearity of elasticity, which is considerable especially at the central part of the arterial network. Among the seven arteries, the brachiocephalic trunk has the largest nonlinearity (Figure 6.4, top row). At the aorta, the nonlinearity decreases from the proximal part to the distal end (Figure 6.3, top row to bottom row). At the peripheral arteries, represented by carotid artery and femoral artery, the nonlinearity is negligible (Figure 6.4, second and bottom rows).

Figure 6.5 presents the statistics of the arterial properties of the group of sheep: the mean values of reference radius R_0, Young's modulus E, viscosity coefficient ϕ, and the ratio ϕ/E with their corresponding standard deviations. We observe that the variations of R_0, E and ϕ between different sheep are much smaller than between different arteries. The carotid artery has considerable bigger values of viscoelasticity than other arteries. Another noticeable pattern is that the ratio ϕ/E varies slightly among the different arteries (Figure 6.6(f)).

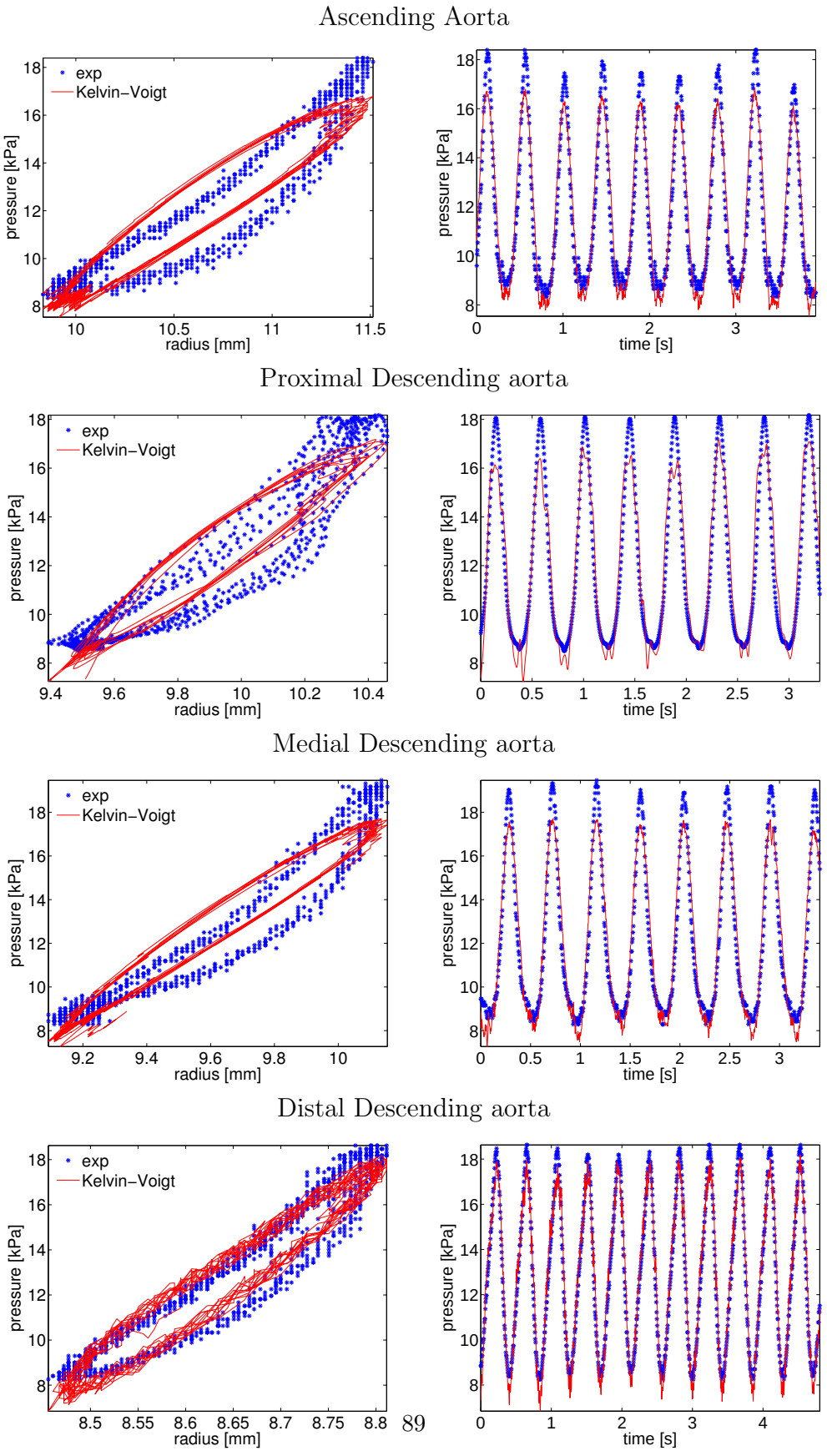

Figure 6.3.: Experimental data and the fitted Kelvin-Voigt model. Left column: hysteresis loop. Right column: time series.

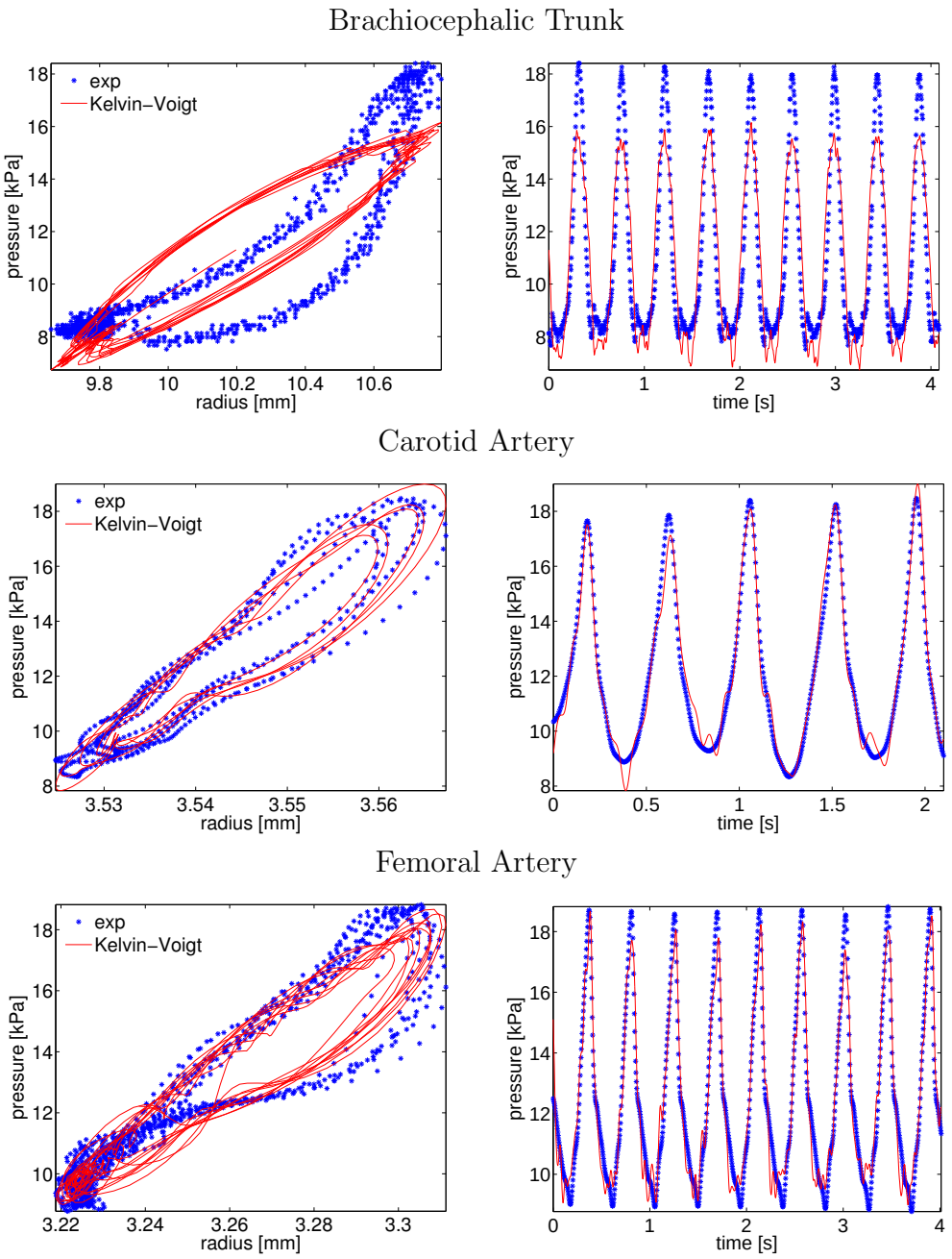

Figure 6.4.: Experimental data and the fitted Kelvin-Voigt model (continued). Left column: hysteresis loop. Right column: time series.

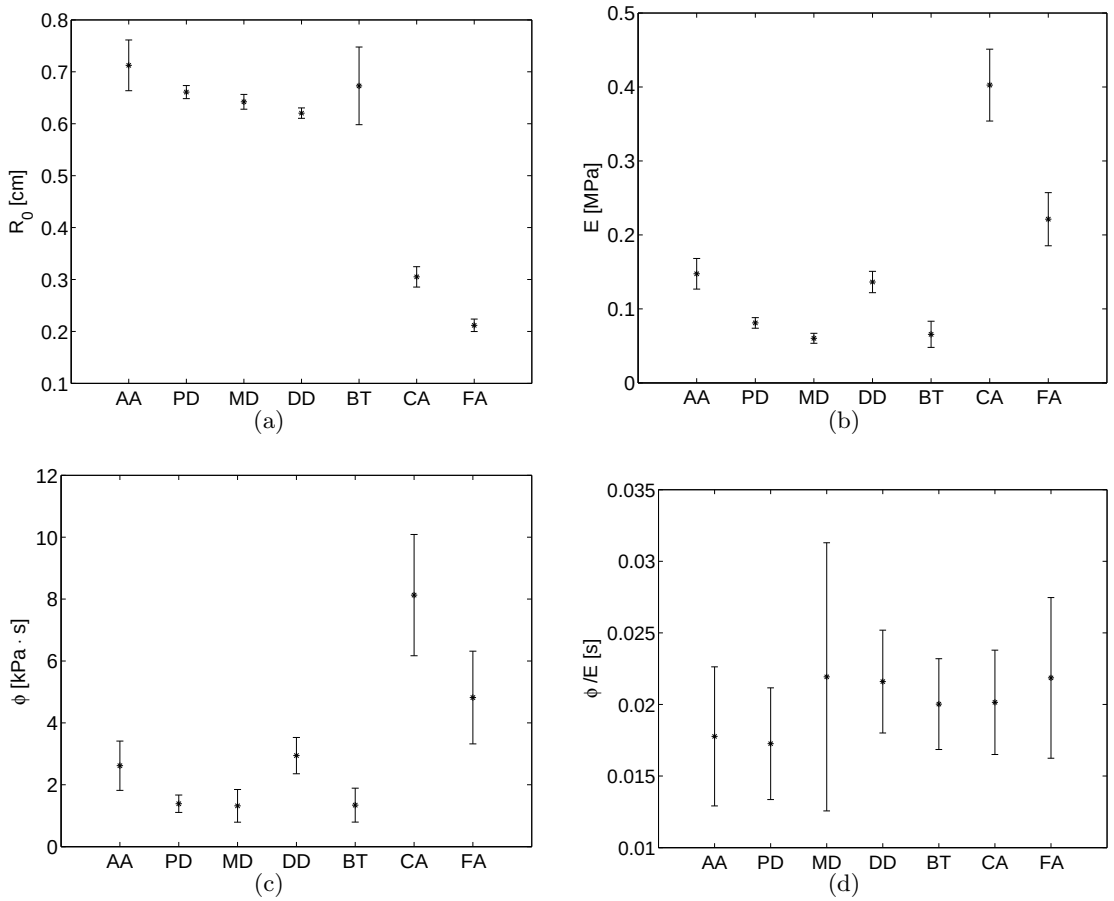

Figure 6.5.: Mean values of the reference radius R_0 (top left), Young's modulus E (top right), viscosity coefficient ϕ (bottom left) and relaxation time ϕ/E (bottom right) with standard deviations among the group of sheep at the seven locations of the arterial network.

6.3.2. Pulse waves

Table 6.1 shows the parameters of the simulated arterial tree where the length L of each artery is estimated from data in literature [29]. All other parameters are the mean values measured in the experiments. To model the side branches of the aorta, we added three virtual arteries at the ends of PD, MD and DD respectively (see Figure 6.1). The radius of the virtual arteries were determined by Murray's law and their elasticity were calculated with a well-matched condition (essentially no reflections at the bifurcations).

Figure 6.6 presents the simulated results at three locations: (i) MD as a representative for central arteries, and (ii) CA and FA for peripheral arteries. It is obvious that the viscoelastic model predicts smoother waveforms. The high frequency components of the

Artery	L (cm)	R_0 (cm)	h (cm)	E (MPa)	ϕ (kPa·s)
AA	4	0.7125	0.38	0.1475	2.6156
PD	10	0.8841	0.91	0.0811	1.3866
MD	10	0.6422	1.26	0.0603	1.3187
DD	15	0.6204	1.10	0.1363	2.9425
BT	4	0.6729	1.06	0.0656	1.3427
CA	15	0.3051	0.78	0.4025	8.1286
FA	10	0.2118	0.31	0.2213	4.8186
VA1	20	0.2601	1.00	0.2213	1.0000
VA2	20	0.2762	1.00	0.4025	1.0000
VA3	20	1.1441	1.00	0.2213	1.0000

Table 6.1.: Parameters of the simulated arterial tree.

waveform are damped by the wall viscosity, which is most noticeable in CA.

6.4. Discussion

Several previous studies [32, 61, 64, 70, 77] have shown the significant damping effect of wall viscosity on the pulse waves. However, the simulations are limited by the lack of exact values of the model parameters, especially for the viscoelasticity of the arterial network. We estimate the viscoelasticity by evaluating the pressure-diameter relationship from a dataset of direct measurements on several locations of arterial network of sheep. With the obtained parameter values, we simulate the pulse waves in the sheep network with the nonlinear 1D model.

There are several models for the viscoelasticity (see e.g. [9, 32, 70, 84]). Fung's quasi-linear model is more generalized than the spring-dashpot models, but it is more difficult to be incorporated with the 1D fluid model, thus it is only applicable to limited formulations of the 1D model (e.g. linearized 1D model [32, 70]). We adopt the Kelvin-Voigt model to fit the pressure-diameter relationship. The results show that this model captures the viscosity quite well. Valdez-Jasso et al. [85] tested the Kelvin model, which adopt a stress relaxation constant as an extra parameter. However, their sensitivity analysis shows that the model prediction depends least on this constant among all the parameters. Thus, even though the Kelvin-Voigt doesn't include this constant, the validity is hardly influenced. Moreover, in contrast to nonlinear optimization methods to estimate the model parameters in [85], we use the linear regression method which is very fast and the global optimization is readily guaranteed. We also note that the model needs further improvements to account for the nonlinearity of elasticity, especially for the central arteries.

By examining the parameter values among the different arteries, we can clearly see that smaller arteries tend to be stiffer, which has been pointed out by previous studies [84, 85]. However, we want to stress the ratio between ϕ and E in this study. By substituting a

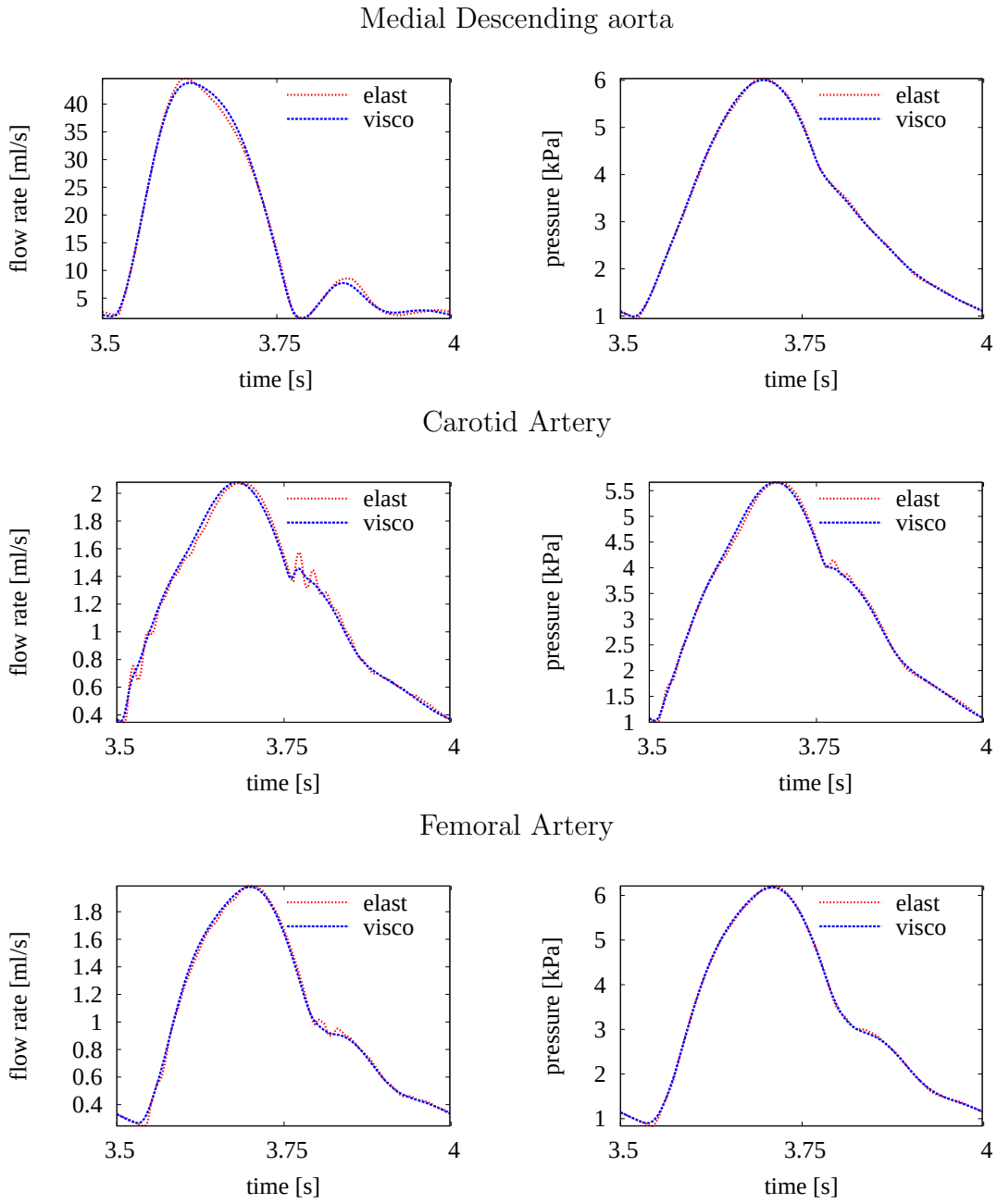

Figure 6.6.: Time series of pressure and flow rate at MD , CA and FA. The viscoelastic model predicts a smoother waveform than the elastic model.

harmonic perturbation $(\sigma, \epsilon) = (\sigma_0, \epsilon_0)e^{i\omega t}$ into the Kelvin-Voigt equation (6.1), we have

$$\sigma_0 = (E + i\phi\omega)\epsilon_0,$$

where $G(i\omega) = E + i\phi\omega$ is the complex modulus. The amplitude of G and the phase shift δ are

$$|G| = E\sqrt{1 + \left(\frac{t_r}{t_f}\right)^2}, \quad \delta = \arctan\left(\frac{t_r}{t_f}\right),$$

where $t_r = \phi/E$ is the viscoelastic relaxation time and $t_f = 1/\omega$ is the typical forcing time. If a transit perturbation is imposed on the arterial wall, it will restore to equilibrium but with a phase lag, which is characterized by the viscoelastic relaxation time. Figure 6.6(f) shows that the viscoelastic relaxation time seems a biological constant. Re-writing the phase shift as

$$\delta = \arctan\left(t_r\omega\right),$$

we can see that when ω increases, δ approaches $\pi/2$. It is obvious that for bigger values of ω, the amplitude of G is bigger. This indicates that the higher the frequency of the waves, the stronger the damping effect of the viscosity. Since the wavefronts are more steepened toward the peripheral part of the arterial tree due to the advection effect of blood flow, the damping effect is more significant in this part. This may be a key protective factor of the micro-circulations.

In a stiffer vascular network, more pulsation energy of high frequency tend to be damped in micro-circulations, especially in the brain and kidney [52]. This is considered to be related with the diseases of these organs, which usually coincide with atherosclerosis. The arterial wall is mainly composed of elastin and muscular fibers, and this composition varies throughout the whole network, from the aorta to the peripheral arteries. The elastin is more related with the elasticity modulus and the muscular fibers with the viscoelasticity. The smaller arteries usually have more muscular fibers than large arteries, and this may also be explained by the need of a stronger damping factor of pulsations right before the micro-circulations.

6.5. Conclusion

We estimated the viscoelasticity of arterial network of sheep by evaluating the pressure-diameter relationship with a dataset of direct measurements on several locations of the network. Quite good agreements between Kelvin-Voigt model and measurements were achieved through a linear regression method. The obtained parameter values were used in a nonlinear 1D model to simulate the pulse waves in the arterial network. We have shown the damping effect of the wall viscosity on the high frequency waves, especially at the peripheral arteries. This was explained by the nearly constant value of the viscoelastic relaxation time, which is defined by the ratio between the viscosity coefficient and the Young's modulus.

7. Blood flow induced by axillofemoral and femoral-femoral anastomoses with a severe iliac stenosis: a numerical study

7.1. Introduction

There are some medical situations when the blood flow to the infra aortic arteries needs to be restored. These situations are caused by severe stenoses or total occlusion of the aorta or iliac arteries. This causes gluteal, pelvic or leg ischemia, leading to symptoms from effort pain to tissue loss which may lead to amputation if blood flow is not restored in time. There are different ways to treat such vascular problems. In case of a simple artery stenosis or a short artery occlusion, endovascular surgery may be a good option to improve the blood flow. In other cases, conventional surgery has to be practiced. The best conventional solution is aorto-femoral or aortobifemoral bypass, well known for their long term patency, and for restoring complete flow to lower legs. When aorta can not be the bypass origin, because of major calcifications or because of a fragile patient condition, another way to restore flow is an axillo-femoral bypass between one axillary artery and one or two femoral arteries. Surgeons have to realize a proximal anastomosis between axillary artery and the beginning of prosthetic bypass and a distal anastomosis between the end of the bypass and the femoral artery. The bypass can be a polyesther or a polytetrafluoroetylen graft. Clinical data show that bypass patency is correlated with mechanical properties of the bypass. The mechanisms of this correlation may be alterations of local or global blood flow. Some studies show that peak flow velocity is a predictive marker of long term bypass patency. Compliance mismatch contribute to neointima hyperplasia through wall shear stress modifications at both anastomosis sites. Another point is that the femoral outflow is correlated to the axillary inflow and to the hemodynamic bypass conditions. Thus, there are a lot of factors influencing both bypass patency and femoral outflow.

Aorto-iliac occlusive disease blocks blood supply to the influenced leg. Aorto-femoral bypass grafting is usually first considered when there is no endovascular option. But when patients have prohibitive risks to undertake aorto-femoral bypass, Axillo-femoral bypass grafting (AxFBG) and femoral-femoral bypass grafting (FFBG) become alternative options to relieve the ischemia legs [49, 58]. AxFBG is a surgery of tunneling the axillary artery to the femoral artery by a subcutaneous vascular. Similarly, FFBG is a bypassing between the healthy femoral artery and the diseased one. In practice, polyethylene terephthalate (Darcon) and expanded polytetrafluoroethylene (ePTFE) are used as prosthetic vessels.

To simulate the blood flow in a large arterial network, a practical and effective model is the one-dimensional model. In this model, the hemodynamic quantities are described as mean values on the cross section of arteries. By solving this model, we can get the flow rate, the cross-sectional area, the pressure and some other quantities which can be derived further. In this chapter we apply a vascular 1D simulation to investigate the hemodynamic changes created by such a bypass, and the clinical relevance of the hemodynamics.

7.2. Methodology

7.2.1. The 1D model of blood flow

For pulsatile flow in a distensible vessel, the 1D model describes the distributions of the cross sectional area A, the flow rate Q and the internal pressure P. If we denote the axial distance of the vessel by x and the time by t, the governing equations for conservation of mass and balance of momentum write

$$\frac{\partial A}{\partial t} + \frac{\partial Q}{\partial x} = 0, \tag{7.1}$$

$$\frac{\partial Q}{\partial t} + \frac{\partial}{\partial x}\left(\frac{Q^2}{A}\right) + \frac{A}{\rho}\frac{\partial P}{\partial x} = -C_f \frac{Q}{A}, \tag{7.2}$$

where ρ is the blood density and C_f is a coefficient of fluid friction drag. The value of C_f is proportional to the kinematic viscosity of the blood ν and the shear strain at the interface between the blood and the wall. The latter is strongly related with the Womersley number. For the blood flow in large arteries, which is featured by a Womersley number of about 10, C_f has an empirical value of $22\pi\nu$.

Those equations are complemented by a constitutive equation of the arterial wall, which relates A and P

$$P = P(A).$$

If the arterial wall is simplified as a thin shell with homogenous elastic material, the transmural pressure $P - P_{ext}$ has a linear relation with the elongation of the internal radius,

$$P - P_{ext} = \beta(\sqrt{A} - \sqrt{A_0}), \tag{7.3}$$

where

$$\beta = \frac{\sqrt{\pi}Eh}{(1-\eta^2)A_0},$$

with A_0 the reference cross-sectional area, E the Young's modulus, h the thickness of the wall and η the Poisson's ration. For incompressible materials like the arterial wall, $\eta = 1/2$. At the conjunction points, the mass and momentum are conserved and the energy dissipations due to discontinuities are neglected as shown to be reasonable in literature [50].

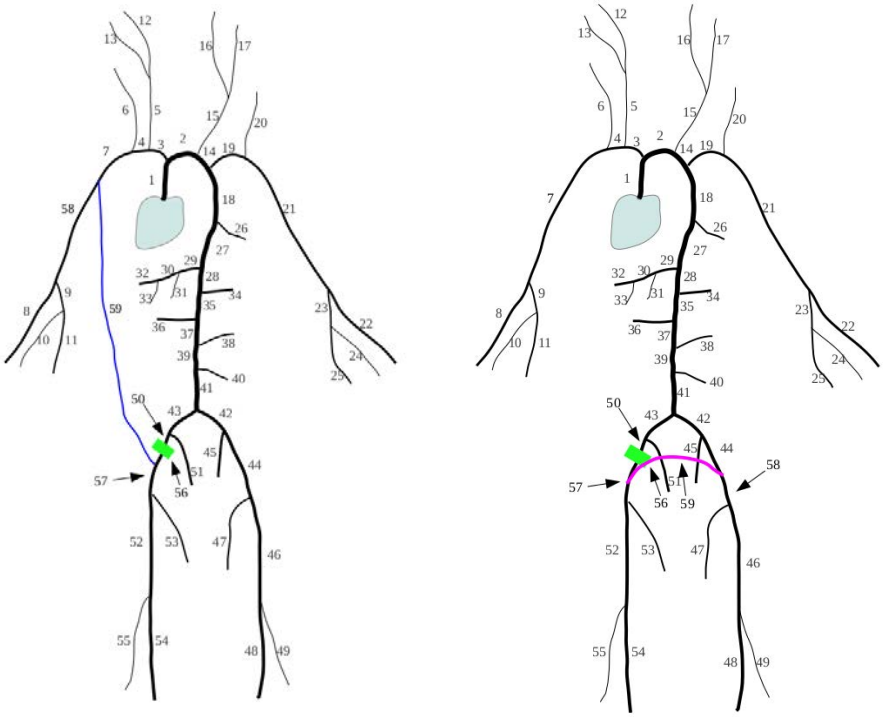

Figure 7.1.: Illustration of AxFBG (left) and FFBG (right) anastomoses to treat a severe stenosis at the right iliac artery.

7.2.2. Simulations

We adopted the data in literature [71] for the whole systemic network with 55 main arteries of a general adult human (see Fig. 7.1). To model a severe stenosis in the right external iliac artery, we chose a 5-cm segment and set the diameter to be 5% of the original one, which means that the lumen loss is 97.5%. For the AxFBG, the anastomosis at the proximal end is made at the right subclavian II. The distance from the root of the right vertebral to the anastomosis point is 12.2 cm. The distal anastomosis is made right downstream of the stenosis at the right external iliac artery. The length of the AxFBG bypass graft is set to 40 cm. For the FFBG approach, the proximal anastomosis is located at the left external iliac with a distance of 4.4 cm from the root of left internal iliac. For this surgery, the bypass graft is 20 cm in length. The clinically used prothesis vessels are 0.4 in radius R and about 0.05 cm in thickness of the wall h. If we adopt these two values and set the Young's modus E to 9 MPa, the compliance is 1.78 $\times 10^{-4}$/mmHg, which is defined as the change ratio of diameter per unit of pressure. The compliance can be calculated with the formula $\Delta R/(PR) = R/(Eh)$. The value of compliance is 1.6 for Darcon and 1.9 for ePTFE [69]. Since the elasticity of the grafts in the simulation is between the two values, we can consider it as an approximation of the real conditions. All of the parameters of the two bypass grafts are summarized in Table 7.1.

grafts	L (cm)	R_0 (cm)	E (MPa)	h (cm)	Compliance ($\times 10^{-4}$/mmHg)
A-F	40	0.4	9	0.05	1.79
F-F	20	0.4	9	0.05	1.79

Table 7.1.: Parameters of bypass grafts. Compliance is defined by $\Delta R/(PR) = R/(Eh)$.

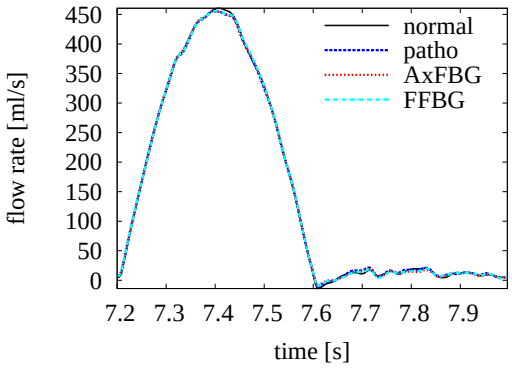

Figure 7.2.: The flow rate at the middle of the ascending aorta.

The governing equations were discretized by the MUSCL (Monotonic Upwind Scheme for Conservation Law) scheme. The code has been validated by analytical solutions and experiments [92, 93]. Each cell of the mesh was about 0.15 cm in length. The time step size was set to 0.04 ms. If we double the number of cells, the change ratio of numerical results were less than 1.3% in both pressure and flow rate. Thus the numerical convergence was checked. The cardiac output was modeled by a cyclic half sinusoidal function with a period of 0.8 s. The total volume of one stroke was 120 ml and accordingly the peak value of flow rate was 471 ml/s. We plotted in Fig. 7.2 the flow rate at the middle of the ascending aorta, which is very close to the cardiac output function we imposed at the inlet of the network. Ten heart beats were run to secure that a stable state was achieved and only the tenth heart beat was plotted.

7.3. Results

Fig. 7.3 shows the flow rate and pressure at the two bypass grafts. The pressure does not have big difference at the two grafts (Fig. 7.3(b)). In contrast, the flow rate has a significant bigger pulse amplitude at the AxFBG graft than at the FFBG graft (Fig. 7.3(a)).

To investigate the blood flow at the host and diseased arteries, as shown in Fig. 7.4 we plotted at the right subclavian, left iliac and right femoral arteries. The flow rate and pressure are plotted in the four conditions: normal, pathological, and after the two anastomoses. With the severe stenosis, both the flow rate and pressure drop essentially to zero at the influenced part of the leg (Fig. 7.4(e) and 7.4(f)). While the stenosis

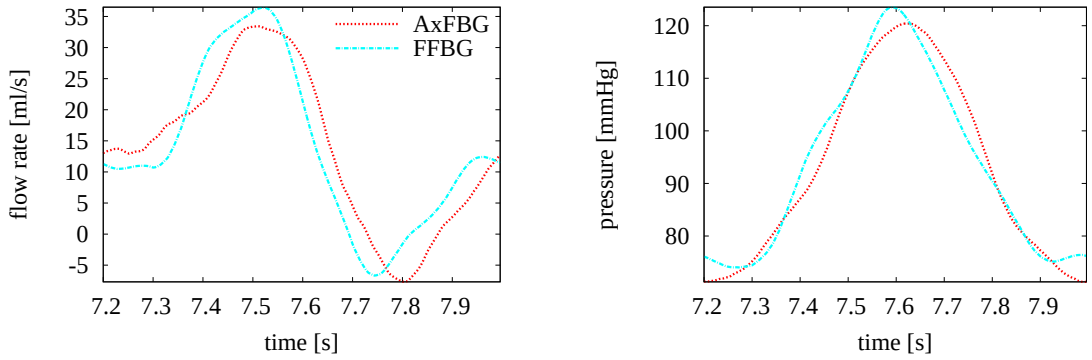

Figure 7.3.: Flow rate and pressure at the bypass grafts.

has negligible effect on the flow rate at the subclavian and left iliac arteries (Fig. 7.4(a) and 7.4(c)), the pressure increases at those sites (Fig. 7.4(b) and 7.4(d)).

After the AxFBG surgery, the flow rate at the upstream of the anastomosis site increases about 50 ml/s at the peak than the normal condition (red line, Fig. 7.4(a)). The reduction of blood flow at the downstream of anastomosis sees quite small at the host arm. The pressure drops significantly, even lower than the normal one (red line, Fig. 7.4(b)). The influence of the FFBG surgery on the left iliac artery is shown in Fig. 7.4(c) and 7.4(d). Both the flow rate and pressure at the down stream of the anastomosis site are very close to the normal level. At the upstream, the pressure is also close to the normal level, but the flow rate increases a lot.

At the diseased leg, after the bypass surgery, both the flow rate and pressure restore to almost the normal level, see Fig 7.4(e) and 7.4(f). But the waveforms for the two surgeries are lagged in phase than the normal one, especially the one for the AxFBG. Taken as a whole, the blood flow restored by the FFBG is better than by the AxFBG. This can be explained by the quasi-symmetry between the two iliac arteries in the network and the shorter length of the FFBG graft.

7.4. Discussions

Severe stenosis in iliac arteries blocks blood supply to the whole influenced leg. In medical practice, there are some conditions when endovascular and aorto-femoral bypass surgeries cannot be practiced due to many risk factors. Those conditions often happen to old patients who usually have some other complications. AxFBG and FFBG are the last options for a vascular surgeon if the arteries in one side of armies or legs of the patient are healthy. Clinical observations show that the success rate of the anastomosis surgeries are correlated with the hemodynamics.

We simulated the blood flow of the whole arterial network with a severe stenosis in the right external iliac artery. Both AxFBG and FFBG can restore blood flow to the

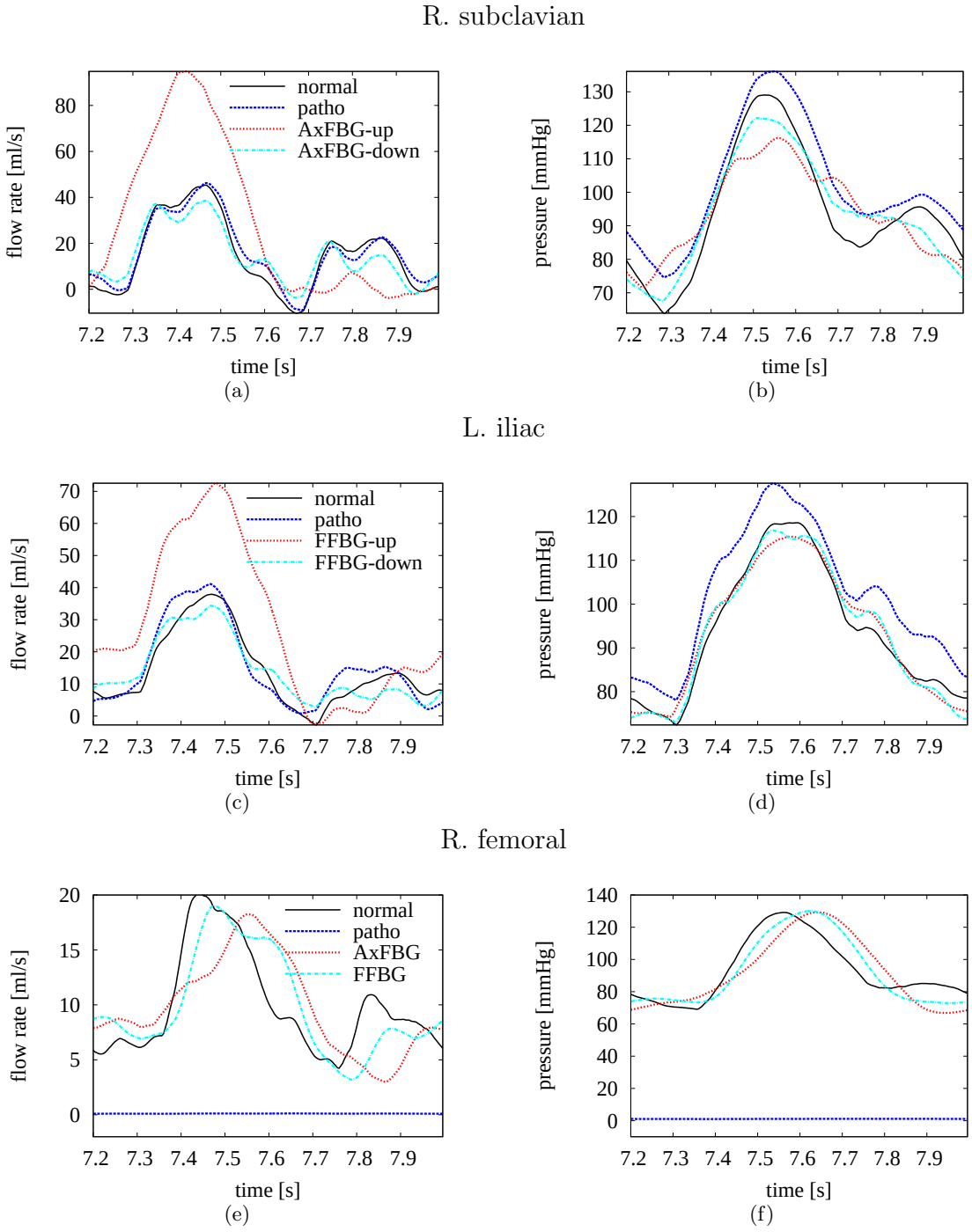

Figure 7.4.: Flow rate and pressure at the host and diseased arteries before and after the anastomoses.

diseased leg. However, the FFBG has a better result because the phase lag of the restored flow is smaller compared with the AxFBG. The proximity of the two iliac arteries gives a significant advantage to FFBG over AxFBG. A shorter prothesis graft introduces less resistance and that also seems an important factor to take into account when the bypassing path is designed.

However, for a patient with severe stenosis in one leg, there is a big possibility that the other leg also suffers from vascular diseases. This factor has to be considered in the future research. Moreover the flow velocity and wall shear stress (WSS) are seen as indicators of long term patency of the prosthesis. But the flow velocity predicted by the 1D model is the average velocity over the cross section and the velocity measured in clinics is the centerline velocity. To make them comparable, an exact velocity profile has to be determined. The estimation of WSS is also related with the velocity profile. The predictions of those two quantities by the 1D model have to validated by experiments.

7.5. Conclusion

Blood flow in the whole arterial network with a severe iliac stenosis is simulated by the 1D model and two anastomosis surgeries are evaluated. In the ideal case when the other leg does not suffer vascular diseases, the FFBG surgery is more advantageous over the AxFBG surgery due to the proximity between the host artery and the receptor artery. Again, we stress that the 1D model can be a useful tool in evaluations and optimizations of vascular surgeries.

8. Summary and Perspectives

While the study on blood flow has a very long history, it is still a very active research topic with urgent needs on clinics and a lot of challenging problems. Modeling the blood flow and properly interpreting the results need knowledge of multidisciplinary fields including physics, applied mathematics, computer science and medicine. 1D model of blood flow is well balanced between complexity and accuracy. It can predict the time-dependent distributions of pressure and flow rate at vascular networks. In this thesis, we first studied the numerical methods for the 1D model and developed a fast parallel code which can compute large networks. Moreover, with data collected from *in vitro* experimental setup and *in vivo* arterial networks, we studied the coefficient of fluid friction and wall viscoelasticity. A preliminary study of the hemodynamics induced by two anastomoses has been done with the 1D model.

8.1. Summary

This section summarizes the main achievements and conclusions of the thesis. Because the heart output is cyclic, the blood flow in the vascular system is pulsatile. Due to the distensibility of the blood vessels, the pulsation propagates in the network with a characteristic speed of 10 m/s. During the propagation, the waves are reflected and re-reflected at many points of discontinuities of the network, which makes the waveforms very complicated. One challenge of computer simulation of the blood flow is due to the large number of vessel segments. While usually the vascular beds are modeled with 0D models, this approach can not provide distributive information of the blood flow. Thus one objective of this thesis is to develop a tool, which can compute very large networks as fast as possible.

First we recalled the derivation of the 1D model, taking the approach of integrating along the radius of an axisymmetric flow. The axial velocity profile and tube law have been given special attention, because they are related with two important damping parameters of the 1D model. If the viscoelasticity of the vessel wall is described by a Kelvin-Voigt model, a hyperbolic-parabolic system of governing equations for the pulsatile blood flow can be derived. Many numerical schemes have been proposed to discretize the governing equations. We implemented in MATLAB four schemes, namely MacCormack, Taylor-Galerkin, MUSCL (Monotonic Upstream Scheme for Conservation Laws) and local discontinuous Galerkin. Those schemes belong to various numerical frameworks and they were cross compared with tests on several cases. The verifications of the implementations were done by the linearized model and asymptotic solutions were computed if there are various source terms. The tests show that the schemes have different features. The MacCormack is very simple to implement and quite accurate (of

second order in both time and space) when the nonlinearity of the system is not very large. The Taylor-Galerkin is well balanced between accuracy and speed in the case of a moderate nonlinearity. The MUSCL can capture shocks without non-physical oscillations, which is a unique feature among the four schemes. The local discontinuous Galerkin has very small numerical dissipation and dispersion. But if the wall viscosity is large, a very small time step size is necessitated, which makes the scheme very slow.

To improve the computation speed, a parallel C++ code has been developed. The topology of the network is described by a directed acyclic graph (DAG). To simulate a specific network, all the configurations are set by comma-separated-value files (CSV). If the network is complicated, the parameter files can be prepared by scripts of Python (other higher level languages are also possible). We computed three cases: a circle of arteries, a systemic arterial tree with 55 vessels, and an anatomically accurate network of a mouse kidney with over one thousand segments of vessels. The numerical results were visualized and the propagation pattern of the pulse waves can be seen clearly. Tests on multi-core workstations show that good speedup is achieved by parallelizations of the code for big networks.

The fluid friction and wall viscosity are two damping parameters of the 1D viscoelastic model of blood flow, but their values are difficult to evaluate separately. For the fluid friction, previous studies either assume a rough estimation or adopt a value in literature, which is actually fitted with an elastic model (wall viscosity is neglected). We fitted the two factors in pairs against pressure waves in a well-defined experimental setup. The study helps determine the coefficient of fluid friction and the influence of wall viscosity on the pulse waves.

To evaluate the viscoelasticity of *in vivo* arteries, we fitted the Kelvin-Voigt model against the time series of pressure and internal radius measured at several locations of sheep arterial network. With the estimated parameter values, a network was simulated with elastic and viscoelastic 1D models. The comparison between the numerical results shows the damping effect of the viscoelasticity on the high frequency components of the waveform. A simple theory was proposed to explain the damping mechanism with a characteristic relaxation time, which seems from the experimental data to be almost constant throughout the network.

Finally, we applied the developed code to simulate a vascular disease and evaluated the surgery options from the point of view of hemodynamics. For a patient with severe iliac stenosis, if there are risk factors preventing intravascular angioplasty and aortofemoral anastomosis, axillo-femoral and femoral-femoral anastomoses become the only options of surgeons. The simulation produced results compatible with data in literature. We evaluated the axillo-femoral and femoral-femoral anastomoses on several aspects: the rebuilding of blood supply to the diseased leg, the influence on the host arteries, and the blood flow in the bypass prothesis etc.

8.2. Perspectives

The long term objective is to develop a tool with the 1D model which can be used in clinics for diagnosis and surgery evaluation of vascular diseases. From the work of this thesis, we can progress in the following directions in the near future.

- *Simulation of some special circulations as detailed as possible.* We have shown the simulation of the renal circulation with a detailed network of over one thousand segments. It is well known that the kidney controls the blood flow actively in response to the internal environment of the body. By setting the elasticity of the vessels as a variable quantity changing in time, we can investigate the controlling mechanism on the distribution of the blood supply. Moreover, the coronary, hepatic, and cerebral circulations are also considered to be simulated with more detailed networks.

- *Coupling the venous system.* Compared with the modeling of arterial blood flow, the venous blood flow attracts less attention. Even though the veins have some distinct features such as collapsibility, unidirectional valves and considerable external pressures at some locations, the venous flow still can be described by the 1D model with some modifications. In the pulmonary circulation, the pulsations propagate to the venous system. In the systemic circulation, there are also considerable pressure variations in the venous system due to activities or posture changes. Coupling the two systems both described by the 1D model can help investigate the interaction dynamics and further may achieve a closed loop of model for the whole cardiovascular system.

- *Estimation of the parameters of the model.* One challenge for patient-specific simulations is to properly set the parameters of the model. Uncertainty qualification methods such as Monte-Carlo analysis can help determine the parameters whose uncertainties influence significantly the output of the model. Thus special attention is needed to improve the measurement techniques of those sensitive parameters. The data assimilation techniques estimate the model parameters from the model outputs which are usually easier to measure with various non-invasive techniques such as MIR, ultrasound imaging etc. Those techniques help make the non-invasive diagnosis closer to real clinical applications. The fast code developed in this thesis can be a convenient tool for numerical experiments of the researches in those directions.

Appendix A.

Simulation and data analysis

A.1. Parameter files and running simulations.

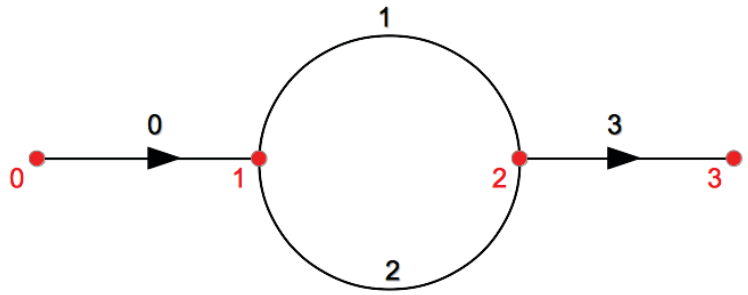

Figure A.1.: A circle of arteries.

We take a circle of arteries (shown in Fig. A.1) as an example to show how to set the parameter files. In this network, there are four nodes, labeled from 0 to 3 in red, and four directed edges, also labeled from 0 to 3. The DAG.csv file looks like the list A.1 Each row is a record of an artery, where the first number stands for the starting node

Listing A.1: DAG.csv

```
0 ,1
1 ,2
1 ,2
2 ,3
```

and the second number the end node. The number of row should be the same as that of the corresponding artery. By default, the node 0 is the inlet of the network. The inlet could be specified in flow rate, pressure or cross-sectional area. For instance, to specify the the flow rate, we shall use the key words <time > and <Q_Input> to indicate the columns of time and flux. Cross-sectional area and pressure are indicated by <A_Input> and <P_Input>. The outlets are specified by the number of leaf nodes and the reflection coefficient. In this example, the outlet is node 3 and the reflection coefficient is 0.0 as shown in A.3.

Listing A.2: Inlet.csv

```
<time>              <Q_Input>(cm^3/s)
0.000000000000000e+00          0.000000000000000e+00
4.000066667777797e-05          3.141644962660321e-04
8.000133335555594e-05          6.283289615242379e-04
1.200020000333339e-04          9.424933647667942e-04
1.600026667111119e-04          1.256657674985884e-03
2.000033333888898e-04          1.570821861173699e-03
...
```

Listing A.3: Outlet.csv

```
3,0
```

Similarly, the file for the vessel properties looks like Fig. A.2. The key works are self-explanatory.

C	D	E	F	G	H	I	J	K	L
<A0> (cm^2)	<Thickness> (cm)	<Length>(cm)	<N>(mesh points)	<E>(10^6 Pa)	<beta>(10^6 Pa/cm)	<Cv>(10^4 cm^2/s)	<fric>	<solver>	<order>
4	0.1	400	1600	0.4	0.023632718	0	0	FV	2
2	0.1	200	800	0.4	0.047265436	0	0	FV	2
2	0.1	200	800	0.4	0.047265436	0	0	FV	2
4	0.1	400	1600	0.4	0.023632718	0	0	FV	2

Figure A.2.: vessel file.

The simulation and recording time are set in the list A.4

In list A.5, we specify the recording location: the first column is the artery and the second column is the mesh point.

Now all the parameter files are ready and we are going to run the simulations in a unix-like environment. Before running the simulation, we can set the number of threads explicitly in the terminal by the command:

```
export OMP_NUM_THREADS=4
```

If we put all those files in a subfolder named *Param*, and create a subdirectory to put the result, for instance *data*, we can initiate the computing by the command:

```
bloodflow -i param -o data -v
```

The option -v (verbose) is for debugging of the parameters file. With this option, the configurations of the simulation will be shown like Fig. A.3.

A.2. Pre- and post- processing.

Directly writing parameter files is tedious and error-prone, especially when the network is quite large. We can set the parameter with pythons scripts, and through previously

Listing A.4: time_setup.csv

```
<t_final>(s),<t_step>(s),<record_start>,<record_end>
2.4,4e-05,0,2.4
```

Listing A.5: output.csv

```
<numArtery>,<numMeshPoint>
0,0
0,7
...
```

defined methods, all the parameters can be written in a compatible form with the C++ code. List A.6 illustrates the main steps to do this. The file fig_data.csv stores processes data with Python scripts. The first two columns are the coordinates of the 2D network, and the following columns are the pressure at corresponding points. We give in List A.7 a bash script which makes an animation with Gnuplot as the plotting engine.

```
Xiaofei-MacBook-Pro:branchConvergence xfwang$ bloodflow -i param/ -o data/ -v
input folder: param/
output folder: data/
suffix string: (null)
verbosel: Yes
sequential computing: No
 number of arteries = 4          number of conjuncs = 4
 Final time = 2.400000           time step = 0.000040    Number of time steps = 60000
 The DAG is:
    0    1
    1    2
    1    2
    2    3
arts:
   L(cm)          dx(cm)        N         A0(cm^2)  beta(10^6Pa/cm)   Cv(10^4cm^2/s)       Kr(cm^2/s)   Solver    order  c_ref(cm/s)          dt
0:
  400.00         0.250000     1600         4.000000         0.023633         0.000000         0.000000       FV        2   474.419124     0.000040
1:
  200.00         0.250000      800         2.000000         0.047265         0.000000         0.000000       FV        2   564.182597     0.000040
2:
  200.00         0.250000      800         2.000000         0.047265         0.000000         0.000000       FV        2   564.182597     0.000040
3:
  400.00         0.250000     1600         4.000000         0.023633         0.000000         0.000000       FV        2   474.419124     0.000040

nodes:       Parent    daughter1     dauther2      Re_Coef
0                              0
1                 0            1            2
2                 1            3
3                 3                                0.00
   record_artery     record_nodes
               0                0
```

Figure A.3.: Checking the configurations of the simulation.

Listing A.6: writParameters.py

```
#! /usr/bin/python3
import sys
sys.path.append("install_dirctory_bloodflow/py_lib")
# network_def is a file containing definitions of
# various functions and classes which can
# write paramter files compatibable with the c++ code.
from network_def import *

arts=[ ] # a list of arteries
... #generate each artery, set the paramters,
... # and append it to the list arts.
conjs=[ ] # a list of conjunctions
... #generate each conjunction, set the paramters
... # and then append it to the list conjs.
conjstS=timeSetup()
... #set time control parameters, inflow B.C., etc.
# generate a network
network=network(ARTS=arts,CONS=conjs)
network.tS=tS

#write all the paramter files to the destination directory.
network.writeParam("destination_directory")
```

Listing A.7: make_animation.sh

```
#!/bin/bash
function plot_1snapshot(){
Num_snap=$1
printf -v name "%02i" $1
gnuplot <<_EOF
set terminal gif
dataFile="fig_data.csv"
set style data lines
unset xtics
unset ytics
unset ztics
unset border
set o "destination_dir/anim_${name}.gif"
unset key
splot [][][-6:16] dataFile u 1:2:3 w l ls 1, \
"" u 1:2:$((${Num_snap}+2))
_EOF
}

for i in {1..40}
do
plot_1snapshot $i
done
convert -delay 15 -loop 0 "destination_dir/*.gif" animation.gif
```

A.3. Method of fitting the Kelvin-Voigt model with the data measured on sheep.

Given the Kelvin-Voigt model for the arterial wall,

$$P = \frac{Eh}{(1-\eta^2)R_0} - \frac{Eh}{(1-\eta^2)}\frac{1}{R} + \frac{\phi h}{(1-\eta^2)R_0}\frac{dR}{Rdt}, \tag{A.1}$$

with P the transmural pressure, R the internal radius, E the Young modulus, h the thickness of the arterial wall and η the Poisson constant. The time series of P and R are measured in experiments, and the parameters of the model are wanted. Written in matrix form, the problem can be expressed as

$$P(t) = AC,$$

where A is a $N \times 3$ matrix $[(1, ..., 1)^T, 1/R, dR/(Rdt)]$, with N the number of data points, C the 3×1 coefficient vector $[Eh/((1-\eta^2)R_0), Eh/(1-\eta^2), \phi h/((1-\eta^2)R_0)]^T$. And the objective cost function is

$$J(C) = \frac{1}{N}\sqrt{\sum_i^N ((P_{model})_i - P_i)^2)},$$

with P_{model} the pressure predicted by the model. We assume that the columns of the data matrix are independent in the linear space, the errors of the measurement data are independent and identically distributed. According to the theory of least square method, C is given by,

$$C = (A^T A)^{-1} A^T P.$$

In the data matrix, the derivative of R is evaluated by a spectral numerical method. Given a times series $R(t)$ with period T, it can be expanded in Fourier series

$$R = \sum_{k=-\infty}^{\infty} \hat{R}(k) e^{\frac{2\pi i}{T}kt},$$

where $\hat{R}$ is given by

$$\hat{R}(k) = \frac{1}{T}\int_{t=0}^{T} R(t) e^{-\frac{2\pi i}{T}kt} dt.$$

For the derivative, one has

$$\frac{dR}{dt} = \sum_{k=-\infty}^{\infty} \hat{R}\frac{2\pi i}{T} k e^{\frac{2\pi i}{T}kt}.$$

In the computation,we take advantage of the Discrete Fourier Transform (DFT). The measurement noises are filtered out through a loop in the calculation. The pseudocode is listed below:

- Step 1: Evaluate the DFT of R (assume N as an even number without loss of generality)

$$\hat{R} = \frac{1}{N} \sum_{n=-\frac{N}{2}+1}^{\frac{N}{2}} Re^{-\frac{2\pi i}{N}nk}.$$

- Step 2: If $||\hat{R}_n|| < \gamma$, set $\hat{R}_n = 0$, where γ is a given criterion whose value should be optimized through the loop.

- Step 3: Multiply $\hat{R}_n$ by a factor $\frac{2\pi ni}{T}$ to get $\widehat{DR}$

- Step 4: Evaluate the inverse DFT of $\widehat{DR}$

$$\frac{dR}{dt} = \sum_{n=-\frac{N}{2}+1}^{\frac{N}{2}} \widehat{DR} e^{\frac{2\pi i}{N}nk}$$

- Step 5: Solve the least square problem and evaluate the objective function.

- Step 6: Change γ and return back to Step 2 until the value of objective function is not decreasing.

Bibliography

[1] Global status report on noncommunicable diseases 2010. Technical report, World Health Organization, 2011.

[2] J. Alastruey, A.W. Khir, K.S. Matthys, P. Segers, S.J. Sherwin, P.R. Verdonck, K.H. Parker, and J. Peiró. Pulse wave propagation in a model human arterial network: Assessment of 1-d visco-elastic simulations against *in vitro* measurements. *Journal of biomechanics*, 44(12):2250–2258, 2011.

[3] J. Alastruey, K.H. Parker, J. Peiró, S.M. Byrd, and S.J. Sherwin. Modelling the circle of willis to assess the effects of anatomical variations and occlusions on cerebral flows. *Journal of Biomechanics*, 40(8):1794–1805, 2007.

[4] R.L. Armentano, J.G. Barra, J. Levenson, A. Simon, and R.H. Pichel. Arterial wall mechanics in conscious dogs assessment of viscous, inertial, and elastic moduli to characterize aortic wall behavior. *Circulation Research*, 76(3):468–478, 1995.

[5] K. Azer and C.S. Peskin. A one-dimensional model of blood flow in arteries with friction and convection based on the womersley velocity profile. *Cardiovascular Engineering*, 7(2):51–73, 2007.

[6] R.E. Ballard, D.E. Watenpaugh, G.A. Breit, G. Murthy, D.C. Holley, and A.R. Hargens. Leg intramuscular pressures during locomotion in humans. *Journal of Applied Physiology*, 84(6):1976–1981, 1998.

[7] A.C.L. Barnard, W.A. Hunt, W.P. Timlake, and E. Varley. A theory of fluid flow in compliant tubes. *Biophysical Journal*, 6(6):717–724, 1966.

[8] C. Bertoglio, P. Moireau, and J.-F. Gerbeau. Sequential parameter estimation for fluid–structure problems: Application to hemodynamics. *International Journal for Numerical Methods in Biomedical Engineering*, 28(4):434–455, 2012.

[9] D. Bessems, C.G. Giannopapa, M. Rutten, and F.N. van de Vosse. Experimental validation of a time-domain-based wave propagation model of blood flow in viscoelastic vessels. *Journal of biomechanics*, 41(2):284–291, 2008.

[10] D. Bessems, M. Rutten, and F. Van De Vosse. A wave propagation model of blood flow in large vessels using an approximate velocity profile function. *Journal of Fluid Mechanics*, 580:145–168, 2007.

[11] F. Bouchut. *Nonlinear Stability of Finite Volume Methods for Hyperbolic Conservation Laws: And Well-Balanced Schemes for Sources*. Springer, Basel switzerland, 2004.

[12] B.S. Brook, S.A.E.G. Falle, and T.J. Pedley. Numerical solutions for unsteady gravity-driven flows in collapsible tubes: evolution and roll-wave instability of a steady state. *Journal of Fluid Mechanics*, 396:223–256, 1999.

[13] B.S. Brook and T.J. Pedley. A model for time-dependent flow in (giraffe jugular) veins: uniform tube properties. *Journal of biomechanics*, 35(1):95–107, 2002.

[14] S. Čanić, C.J. Hartley, D. Rosenstrauch, J. Tambača, G. Guidoboni, and A. Mikelić. Blood flow in compliant arteries: an effective viscoelastic reduced model, numerics, and experimental validation. *Annals of Biomedical Engineering*, 34(4):575–592, 2006.

[15] N. Cavallini, V. Caleffi, and V. Coscia. Finite volume and weno scheme in one-dimensional vascular system modelling. *Computers and Mathematics with Applications*, 56(9):2382–2397, 2008.

[16] P. Chen, A. Quarteroni, and G. Rozza. Simulation-based uncertainty quantification of human arterial network hemodynamics. *International journal for numerical methods in biomedical engineering*, 29(6):698–721, 2013.

[17] Y. Chen, L. Zhang, D. Zhang, and D. Zhang. Wrist pulse signal diagnosis using modified gaussian models and fuzzy c-means classification. *Medical engineering & physics*, 31(10):1283–1289, 2009.

[18] H. Coullon, J.-M. Fullana, P.-Y. Lagrée, S. Limet, and X. Wang. Blood flow arterial network simulation with the implicit parallelism library skelgis. In *ICCS 2014*, 2014.

[19] O. Delestre and P.-Y. Lagrée. A well balanced finite volume scheme for blood flow simulations. *International Journal for Numerical Methods in Fluids*, page doi: 10.1002/fld.3736, 2012.

[20] K. DeVault, P.A Gremaud, V. Novak, M.S. Olufsen, G. Vernieres, and P. Zhao. Blood flow in the circle of willis: Modeling and calibration. *Multiscale Modeling & Simulation*, 7(2):888–909, 2008.

[21] S. Dharmananda. The significance of traditional pluse diagnosis in the modern parctice of chinese medicine.

[22] D. Elad, D. Katz, E. Kimmel, and S. Einav. Numerical schemes for unsteady fluid flow through collapsible tubes. *Journal of biomedical engineering*, 13(1):10–18, 1991.

[23] M. Fernández, V. Milisic, and A. Quarteroni. Analysis of a geometrical multiscale blood flow model based on the coupling of odes and hyperbolic pdes. *Multiscale Modeling & Simulation*, 4(1):215–236, 2005.

[24] P. Flaud, P. Guesdon, and J.-M. Fullana. Experiments of draining and filling processes in a collapsible tube at high external pressure. *The European Physical Journal Applied Physics*, 57(03):31101p1–31101p13, 2012.

[25] L. Formaggia, D. Lamponi, and A. Quarteroni. One-dimensional models for blood flow in arteries. *Journal of Engineering Mathematics*, 47:251–276, 2003.

[26] L. Formaggia, A. Quarteroni, and A. Veneziani, editors. *Cardiovascular Mathematics: Modeling and simulation of the circulatory system*, volume 1. Springer, Milano, Italy, 2009.

[27] J.-M. Fullana and S. Zaleski. A branched one-dimensional model of vessel networks. *Journal of Fluid Mechanics*, 621(1):183–204, 2009.

[28] Y.C. Fung. *Biomechanics:Mechanical Properties of Living Tissues*. Springer-Verlag, New York, US, 1993.

[29] Y.C. Fung. *Biomechanics: circulation*. Springer Verlag, New York, US, 1997.

[30] J.-F. Gerbeau, M. Vidrascu, and P. Frey. Fluid–structure interaction in blood flows on geometries based on medical imaging. *Computers and Structures*, 83(2):155–165, 2005.

[31] J.S. Hesthaven and T. Warburton. *Nodal discontinuous Galerkin methods: algorithms, analysis, and applications*, volume 54. Springer-Verlag New York Inc, New York, US, 2008.

[32] R. Holenstein, P. Niederer, and M. Anliker. A viscoelastic model for use in predicting arterial pulse waves. *Journal of biomechanical engineering*, 102(4):318–325, 1980.

[33] W. Huberts, A.S. Bode, W. Kroon, R.N. Planken, J.H.M. Tordoir, F.N. Van de Vosse, and E.M.H. Bosboom. A pulse wave propagation model to support decision-making in vascular access planning in the clinic. *Medical engineering & physics*, 34(2):233–248, 2012.

[34] W. Huberts, K. Van Canneyt, P. Segers, S. Eloot, J.H.M. Tordoir, P. Verdonck, F.N. van de Vosse, and E.M.H. Bosboom. Experimental validation of a pulse wave propagation model for predicting hemodynamics after vascular access surgery. *Journal of biomechanics*, 2012.

[35] T.J.R. Hughes and J. Lubliner. On the one-dimensional theory of blood flow in the larger vessels. *Mathematical Biosciences*, 18(1):161–170, 1973.

[36] Y. Kivity and R. Collins. Nonlinear wave propagation in viscoelastic tubes: application to aortic rupture. *Journal of Biomechanics*, 7(1):67–76, 1974.

[37] D. Kuzmin. Slope limiting for discontinuous galerkin approximations with a possibly non-orthogonal taylor basis. *International Journal for Numerical Methods in Fluids*, 71(9):1178–1190, 2013.

[38] P.-Y. Lagrée. An inverse technique to deduce the elasticity of a large artery. *EPJ Applied Physics*, 9(2):153–164, 2000.

[39] C.A.D. Leguy, E.M.H. Bosboom, A.S.Z. Belloum, A.P.G. Hoeks, and F.N. van de Vosse. Global sensitivity analysis of a wave propagation model for arm arteries. *Medical engineering & physics*, 33(8):1008–1016, 2011.

[40] C.A.D. Leguy, E.M.H. Bosboom, H. Gelderblom, A.P.G. Hoeks, and F.N. van de Vosse. Estimation of distributed arterial mechanical properties using a wave propagation model in a reverse way. *Medical engineering & physics*, 32(9):957–967, 2010.

[41] R.J. LeVeque. *Finite volume methods for hyperbolic problems*, volume 31. Cambridge University Press, Cambridge UK, 2002.

[42] J. Lighthill. *Waves in fluids*. Cambridge University Press, 2001.

[43] S.C. Ling and H.B. Atabek. A nonlinear analysis of pulsatile flow in arteries. *Journal of Fluid Mechanics*, 55(03):493–511, 1972.

[44] D. Lombardi. Inverse problems in 1d hemodynamics on systemic networks: A sequential approach. *International journal for numerical methods in biomedical engineering*, 30(2):160–179, 2014.

[45] R. MacCormack. The effect of viscosity in hypervelocity impact cratering. *Journal of spacecraft and rockets*, 40(5):757–763, 2003.

[46] A.C.I. Malossi, P.J. Blanco, and S. Deparis. A two-level time step technique for the partitioned solution of one-dimensional arterial networks. *Computer Methods in Applied Mechanics and Engineering*, 237:212–226, 2012.

[47] E. Marchandise and P. Flaud. Accurate modelling of unsteady flows in collapsible tubes. *Computer Methods in Biomechanics and Biomedical Engineering*, 13(2):279–290, 2010.

[48] E. Marchandise, M. Willemet, and V. Lacroix. A numerical hemodynamic tool for predictive vascular surgery. *Medical Engineering and Physics*, 31(1):131–144, 2009.

[49] D. Martin and S.G. Katz. Axillofemoral bypass for aortoiliac occlusive disease. *The American journal of surgery*, 180(2):100–103, 2000.

[50] K.S. Matthys, J. Alastruey, J. Peiró, A.W. Khir, P. Segers, P.R. Verdonck, K.H. Parker, and S.J. Sherwin. Pulse wave propagation in a model human arterial network: Assessment of 1-d numerical simulations against *in vitro* measurements. *Journal of Biomechanics*, 40(15):3476–3486, 2007.

[51] J.P. Mynard and P. Nithiarasu. A 1d arterial blood flow model incorporating ventricular pressure, aortic valve and regional coronary flow using the locally conservative galerkin (lcg) method. *Communications in Numerical Methods in Engineering*, 24(5):367–417, 2008.

[52] W. Nichols, M. O'Rourke, and C. Vlachopoulos. *McDonald's blood flow in arteries: theoretical, experimental and clinical principles*. CRC Press, 2011.

[53] F. Nicoud, H. Vernhet, and M. Dauzat. A numerical assessment of wall shear stress changes after endovascular stenting. *Journal of Biomechanics*, 38(10):2019–2027, 2005.

[54] M.S. Olufsen. *Modeling the arterial system with reference to an anestesia simulator*. PhD thesis, Roskilde Universitetscenter,, 1998.

[55] M.S. Olufsen, N.A. Hill, G.D.A. Vaughan, C. Sainsbury, and M. Johnson. Rarefaction and blood pressure in systemic and pulmonary arteries. *Journal of fluid mechanics*, 705:280–305, 2012.

[56] M.S. Olufsen, C.S. Peskin, W.Y. Kim, E.M. Pedersen, A. Nadim, and J. Larsen. Numerical simulation and experimental validation of blood flow in arteries with structured-tree outflow conditions. *Annals of Biomedical Engineering*, 28(11):1281–1299, 2000.

[57] G.L. Papageorgiou, B.N. Jones, V.J. Redding, and N. Hudson. The area ratio of normal arterial junctions and its implications in pulse wave reflections. *Cardiovascular research*, 24(6):478–484, 1990.

[58] M.A. Passman, L.M. Taylor Jr, G.L. Moneta, J.M. Edwards, R.A. Yeager, D.B. McConnell, and J.M. Porter. Comparison of axillofemoral and aortofemoral bypass for aortoiliac occlusive disease. *Journal of vascular surgery*, 23(2):263–271, 1996.

[59] T.J. Pedley. *The Fluid Mechanics of Large Blood Vessels*. Cambridge University Press, Cambridge UK, 1980.

[60] R. Raghu and C.A. Taylor. Verification of a one-dimensional finite element method for modeling blood flow in the cardiovascular system incorporating a viscoelastic wall model. *Finite Elements in Analysis and Design*, 47(6):586–592, 2011.

[61] R. Raghu, I.E. Vignon-Clementel, C.A. Figueroa, and C.A. Taylor. Comparative study of viscoelastic arterial wall models in nonlinear one-dimensional finite element simulations of blood flow. *Journal of biomechanical engineering*, 133(8):081003, 2011.

[62] P.J. Reuderink, H.W. Hoogstraten, P. Sipkema, B. Hillen, and N. Westerhof. Linear and nonlinear one-dimensional models of pulse wave transmission at high womersley numbers. *Journal of biomechanics*, 22(8):819–827, 1989.

[63] P. Reymond, Y. Bohraus, F. Perren, F. Lazeyras, and N. Stergiopulos. Validation of a patient-specific one-dimensional model of the systemic arterial tree. *American Journal of Physiology-Heart and Circulatory Physiology*, 301(3):H1173–H1182, 2011.

[64] P. Reymond, F. Merenda, F. Perren, D. Rüfenacht, and N. Stergiopulos. Validation of a one-dimensional model of the systemic arterial tree. *American Journal of Physiology-Heart and Circulatory Physiology*, 297(1):H208–H222, 2009.

[65] M. Saito. One-dimensional modeling of pulse wave for a human artery model. Technical report, Université Pierre et Marie-Curie, 2010.

[66] M. Saito. *Non-invasive Assessment of Arterial Stiffness by Pulse Wave Analysis: In Vivo Measurements and One-dimensional Theoretical Model*. PhD thesis, Doshisha University, 2011.

[67] M. Saito, Y. Ikenaga, M. Matsukawa, Y. Watanabe, T. Asada, and P.-Y. Lagrée. One-dimensional model for propagation of a pressure wave in a model of the human arterial network: Comparison of theoretical and experimental results. *Journal of Biomechanical Engineering*, 133:121005, 2011.

[68] S. Sankaran, M.E. Moghadam, A.M. Kahn, E.E. Tseng, J.M. Guccione, and A.L. Marsden. Patient-specific multiscale modeling of blood flow for coronary artery bypass graft surgery. *Annals of biomedical engineering*, 40(10):2228–2242, 2012.

[69] S. Sarkar, H.J. Salacinski, G. Hamilton, and A.M. Seifalian. The mechanical properties of infrainguinal vascular bypass grafts: their role in influencing patency. *European journal of vascular and endovascular surgery*, 31(6):627–636, 2006.

[70] P. Segers, N. Stergiopulos, P. Verdonck, and R. Verhoeven. Assessment of distributed arterial network models. *Medical and Biological Engineering and Computing*, 35(6):729–736, 1997.

[71] S.J. Sherwin, L. Formaggia, J. Peiro, and V. Franke. Computational modelling of 1d blood flow with variable mechanical properties and its application to the simulation of wave propagation in the human arterial system. *International Journal for Numerical Methods in Fluids*, 43(6-7):673–700, 2003.

[72] S.J. Sherwin, V. Franke, J. Peiró, and K. Parker. One-dimensional modelling of a vascular network in space-time variables. *Journal of Engineering Mathematics*, 47(3):217–250, 2003.

[73] Y. Shi, P. Lawford, and R. Hose. Review of zero-d and 1-d models of blood flow in the cardiovascular system. *Biomed. Eng. Online*, 10(1):33, 2011.

[74] C.W. Shu. Different formulations of the discontinuous galerkin method for the viscous terms. *Advances in Scientific Computing*, pages 144–155, 2001.

[75] C.W. Shu and S. Osher. Efficient implementation of essentially non-oscillatory shock-capturing schemes. *Journal of Computational Physics*, 77(2):439–471, 1988.

[76] N.P. Smith, A.J. Pullan, and P.J. Hunter. An anatomically based model of transient coronary blood flow in the heart. *SIAM Journal on Applied mathematics*, 62(3):990–1018, 2002.

[77] B.N. Steele, D. Valdez-Jasso, M.A. Haider, and M.S. Olufsen. Predicting arterial flow and pressure dynamics using a 1d fluid dynamics model with a viscoelastic wall. *SIAM Journal on Applied Mathematics*, 71(4):1123–1143, 2011.

[78] B.N. Steele, J. Wan, J.P. Ku, T.J.R. Hughes, and C.A. Taylor. In vivo validation of a one-dimensional finite-element method for predicting blood flow in cardiovascular bypass grafts. *IEEE Transactions on Biomedical Engineering*, 50(6):649–656, 2003.

[79] P.D. Stein and H.N. Sabbah. Turbulent blood flow in the ascending aorta of humans with normal and diseased aortic valves. *Circulation research*, 39(1):58–65, 1976.

[80] N. Stergiopulos, D.F. Young, and T.R. Rogge. Computer simulation of arterial flow with applications to arterial and aortic stenoses. *Journal of Biomechanics*, 25(12):1477–1488, 1992.

[81] J.C. Stettler, P. Niederer, and M. Anliker. Theoretical analysis of arterial hemodynamics including the influence of bifurcations. *Annals of biomedical engineering*, 9(2):145–164, 1981.

[82] A.C.Y. Tang, J.W.Y. Chung, and T.K.S. Wong. Validation of a novel traditional chinese medicine pulse diagnostic model using an artificial neural network. *Evidence-Based Complementary and Alternative Medicine*, 2012, 2011.

[83] E.F. Toro. *Riemann solvers and numerical methods for fluid dynamics*, volume 16. Springer, 1999.

[84] D. Valdez-Jasso, D. Bia, Y. Zócalo, R.L. Armentano, M.A. Haider, and M.S. Olufsen. Linear and nonlinear viscoelastic modeling of aorta and carotid pressure–area dynamics under in vivo and ex vivo conditions. *Annals of Biomedical Engineering*, 39(5):1438–1456, 2011.

[85] D. Valdez-Jasso, M.A. Haider, H.T. Banks, D.B. Santana, Y.Z. Germán, R.L. Armentano, and M.S. Olufsen. Analysis of viscoelastic wall properties in ovine arteries. *IEEE Transactions on Biomedical Engineering*, 56(2):210–219, 2009.

[86] F.N. van de Vosse and N. Stergiopulos. Pulse wave propagation in the arterial tree. *Annual Review of Fluid Mechanics*, 43(1), 2011.

[87] I.E. Vignon and C.A. Taylor. Outflow boundary conditions for one-dimensional finite element modeling of blood flow and pressure waves in arteries. *Wave Motion*, 39(4):361–374, 2004.

[88] I.E. Vignon-Clementel, C.A. Figueroa, K.E. Jansen, and C.A. Taylor. Outflow boundary conditions for 3d simulations of non-periodic blood flow and pressure fields in deformable arteries. *Computer methods in biomechanics and biomedical engineering*, 13(5):625–640, 2010.

[89] J. Wan, B. Steele, S.A. Spicer, S. Strohband, G.R. Feijo, T.J.R. Hughes, and C.A. Taylor. A one-dimensional finite element method for simulation-based medical planning for cardiovascular disease. *Computer Methods in Biomechanics and Biomedical Engineering*, 5(3):195–206, 2002.

[90] H. Wang and Y. Cheng. A quantitative system for pulse diagnosis in traditional chinese medicine. In *Engineering in Medicine and Biology Society, 2005. IEEE-EMBS 2005. 27th Annual International Conference of the*, pages 5676–5679. IEEE, 2006.

[91] J.J. Wang and K.H. Parker. Wave propagation in a model of the arterial circulation. *Journal of biomechanics*, 37(4):457–470, 2004.

[92] X. Wang, O. Delestre, J.-M. Fullana, M. Saito, Y. Ikenaga, M. Matsukawa, and P.-Y. Lagrée. Comparing different numerical methods for solving arterial 1d flows in networks. *Computer Methods in Biomechanics and Biomedical Engineering*, 15(sup1):61–62, 2012.

[93] X. Wang, J.-M. Fullana, and P.-Y. Lagrée. Verification and comparison of four numerical schemes for a 1d viscoelastic blood flow model. *Computer Methods in Biomechanics and Biomedical Engineering*, In press, 2014.

[94] M. Wibmer. *One-dimensional simulation of arterial blood flow with applications.* PhD thesis, Vienna University of Technology, Vienna, Austria, 2004.

[95] M. Willemet, V. Lacroix, and E. Marchandise. Validation of a 1d patient-specific model of the arterial hemodynamics in bypassed lower-limbs: Simulations against in vivo measurements. *Medical engineering & physics*, 2013.

[96] N. Xiao, J. Alastruey, and C. Alberto Figueroa. A systematic comparison between 1-d and 3-d hemodynamics in compliant arterial models. *International journal for numerical methods in biomedical engineering*, 30(2):204–231, 2014.

[97] N. Xiao, J.D. Humphrey, and C.A. Figueroa. Multi-scale computational model of three-dimensional hemodynamics within a deformable full-body arterial network. *Journal of computational physics*, 244:22–40, 2013.

[98] D. Xiu and S.J. Sherwin. Parametric uncertainty analysis of pulse wave propagation in a model of a human arterial network. *Journal of Computational Physics*, 226(2):1385–1407, 2007.

[99] Y. Yamamoto, M. Saito, Y. Ikenaga, M. Matsukawa, Y. Watanabe, M. Furuya, and T. Asada. Experimental study on the pulse wave propagation in a human artery model. *Japanese Journal of Applied Physics*, 50(7), 2011.

[100] S. Yomosa. Solitary waves in large blood vessels. *Journal of the Physical Society of Japan*, 56:506–520, 1987.

[101] M. Zagzoule, J. Khalid-Naciri, and J. Mauss. Unsteady wall shear stress in a distensible tube. *Journal of biomechanics*, 24(6):435–439, 1991.

[102] M. Zagzoule and J.-P. Marc-Vergnes. A global mathematical model of the cerebral circulation in man. *Journal of Biomechanics*, 19(12):1015–1022, 1986.